TRAPPING AND TRANSPORT OF INDIRECT EXCITONS IN COUPLED QUANTUM WELLS

by

Jeffrey K. Wuenschell

BPhil in Engineering Physics, University of Pittsburgh, 2005

M.S. in Electrical Engineering, University of Pittsburgh, 2007

Submitted to the Graduate Faculty of

the Kenneth P. Dietrich School of Arts and Sciences in partial fulfillment

of the requirements for the degree of

Doctor of Philosophy

University of Pittsburgh

2014

UNIVERSITY OF PITTSBURGH

DIETRICH GRADUATE SCHOOL OF ARTS AND SCIENCES

This dissertation was presented

by

Jeffrey K. Wuenschell

It was defended on

December 2, 2014

and approved by

David Snoke, Department of Physics and Astronomy

Kevin Chen, Department of Electrical Engineering

Rob Coalson, Department of Chemistry

Brian D'Urso, Department of Physics and Astronomy

Arthur Kosowsky, Department of Physics and Astronomy

Dissertation Director: David Snoke, Department of Physics and Astronomy

TRAPPING AND TRANSPORT OF INDIRECT EXCITONS IN COUPLED QUANTUM WELLS

Jeffrey K. Wuenschell, PhD

University of Pittsburgh, 2014

Spatially indirect excitons are optically generated composite bosons with a radiative lifetime sufficient to reach thermal equilibrium. This work explores the physics of indirect excitons in coupled quantum wells in the GaAs/AlGaAs system, specifically in the low-temperature, high-density regime. Particular attention is paid to a technique whereby a spatially inhomogeneous strain field is used as a trapping potential. In the process of modeling the trapping profile in wide quantum wells, dramatic effects due to intersubband coupling were observed at high strain. Experimentally, this regime coincides with the abrupt appearance of a dark population of indirect excitons at trap center, an effect originally suspected to be related to Bose-Einstein condensation. Here, the role of band mixing due to the strain-induced distortion of the crystal symmetry will be explored in detail in the context of this effect.

Experimental studies presented here and in the literature suggest that Bose-Einstein condensation in indirect exciton systems may be difficult to detect with optical means (e.g., coherence measurements, momentum-space narrowing), possibly due to the strong dipole interaction between indirect excitons. Due to similarities between this system and liquid helium, it may be more fruitful to look for transport-related signatures of condensation, such as superfluidity. Here, a method for performing transport measurements on optically generated indirect excitons is also outlined and preliminary results are presented.

Keywords: semiconductor, quantum wells, excitons, BEC, stress, photoluminescence, transport.

TABLE OF CONTENTS

LIST OF TABLES

LIST OF FIGURES

PREFACE

I want to thank the members of my doctoral committee: Kevin Chen, Brian D'Urso, Rob Coalson, and Arthur Kosowsky. Your time and feedback are deeply appreciated.

I also want to acknowledge my advisor, David Snoke, for his mentorship during my time at the University of Pittsburgh, both as a graduate student and in the photonics program as an undergrad. None of this work would have been possible without his guidance.

Much of the experimental work discussed here evolved from experiments initially performed by Zoltán Vörös and was done in collaboration with Nick Sinclair. The theoretical work in this dissertation was also built from years of discussion with Nick.

The strain calculations introduced in Chapter 2 grew from work by Ryan Balili and Bryan Nelsen, from whom I learned a great deal. I also want to thank David Meyers for his assistance with some of the fabrication work and measurements discussed in Chapter 4. To my other coworkers - Mark Steger, Chitra Gautham, and Gangqiang Liu - I am grateful for countless hours of discussion and advice. I consider myself extremely lucky to have worked with such an intelligent group of people over the past seven years.

I also want to express my gratitude to the faculty and staff of the University of Pittsburgh Physics Department, as well as the staff of the PINSE Nanoscale Fabrication and Characterization Facility.

This work was funded in part by the US Department of Energy, Grant No. DE-FG02-99ER457080. I also received one year of funding from the Andrew Mellon Predoctoral Fellowship and one year of funding from the Faculty Predoctoral Fellowship.

The GaAs/AlGaAs samples discussed here were grown by our collaborators at Princeton, Loren Pfeiffer and Kenneth West, who are partially funded by the Gordon and Betty Moore Foundation as well as the National Science Foundation MRSEC Program through

the Princeton Center for Complex Materials (DMR-0819860).

This work is dedicated to my family, particularly my parents Joseph and Donna, for their constant love and support.

1.0 INTRODUCTION

This dissertation deals with the study of spatially indirect excitons in gallium arsenide coupled quantum wells. Excitons are a type of metastable quasi-particle that can be optically generated in semiconductor systems, typically at low temperature. The primary focus here will be the search for low temperature phase transitions in excitonic systems, particularly Bose Einstein condensation (BEC). The experiments discussed later in this work revolve around two main ideas - achieving a high density of cold, indirect excitons and finding methods of probing this population for signatures of BEC.

Before delving into the experimental details, this chapter will first provide some context by surveying the theoretical and experimental history of Bose-Einstein condensation over the past century. Following that, the reader will be introduced to the physics of excitons in quantum wells, providing the theoretical background and terminology necessary to understand subsequent chapters.

1.1 BOSE-EINSTEIN CONDENSATION

Indistinguishability is one of the most fundamental ideas of many-body quantum mechanics. Over the course of the last century, physicists have developed rules for calculating expectation values and assigning probabilities to physical measurements in systems containing a large number of particles. To use this machinery, particles are typically assigned labels of some sort. Of course, in the eyes of Nature, each electron is exactly the same as every other, and such labels exist solely in the imagiantion. If the end result of any calculation predicts a physical outcome that is dependent on the labeling scheme used, something must be wrong.

In short, indistinguishability requires that any measurable quantity be unchanged if the arbitrary particle labels are switched around.

Another key concept of quantum mechanics is that the overall phase of a wave function is not physically significant. If a system is split into two coherent sub-systems, the relative phase between them can be measured, but absolute phase should have no physical significance. Applying this concept to the principle of indistinguishability, the spin statistics theorem states that, in three dimensions, the many-particle wave function, Ψ, of N indistinguishable particles must either be symmetric or anti-symmetric under the exchange of any two particles, i.e.

$$\Psi\left(\vec{r}_1, \vec{r}_2, \ldots \vec{r}_i \ldots \vec{r}_j \ldots \vec{r}_{N-1}, \vec{r}_N\right) = \pm\Psi\left(\vec{r}_1, \vec{r}_2, \ldots \vec{r}_j \ldots \vec{r}_i \ldots \vec{r}_{N-1}, \vec{r}_N\right) \tag{1.1}$$

The positive eigenvalue of the particle exchange operation corresponds to particles with integer spin, or bosons. The negative eigenvalue corresponds to particles with half-integer spin, or fermions. [1]

The phenomenon of Bose-Einstein condensation was predicted by Einstein after he was approached by Satyendra Nath Bose, who wrote an analysis of the statistics of distinguishable particles in the context of the black-body problem [2]. The premise of Bose's work is relatively intuitive. If four distinguishable balls are to be distributed in two boxes, the state associated with all four balls in the left box is unique, whereas there are six distinct ways they can be split evenly between the two boxes. If, instead, four *indistinguishable* balls are distributed between two boxes, there is still only one way of putting all the balls in the left box, but there is also only one distinct way of splitting them evenly. Compared to the distinguishable case, the bunched case is statistically much more favorable for indistinguishable particles. [2]

Bose-Einstein statistics can be used to calculate a thermodynamic distribution function- which predicts the mean occupation number of a state with a particular energy, ϵ, at a given

[1] In two-dimensional systems, it is possible to have a more general case, where the eigenvalue of the exchange operation is an arbitrary complex phase - $e^{i\phi}$. This type of particle is called an anyon and corresponds to a rational, non-half-integer spin. Anyons play a role in the fractional quantum Hall effect, but will not be relevant to any of the physics discussed in this dissertation.

[2] This picture is relevant for bosons. For fermions, each box can have at most one ball.

chemical potential, μ and temperature, T,[3] -

$$f(\epsilon) = \frac{1}{\exp\left[\frac{(\epsilon-\mu)}{k_B T}\right] - 1}. \tag{1.2}$$

On a macroscopic scale, one would likely be more interested in the overall density as a function of temperature and chemical potential. In general, the total particle number can be calculated by simply multiplying the density of states, $g(\epsilon)$ (the number of states available in an infinitesmal energy range dϵ around energy ϵ is given by $g(\epsilon)$dϵ) by the Bose-Einstein distribution function, and integrating over all energy,

$$N = N(\epsilon = 0) + \int_0^\infty \frac{g(\epsilon)\mathrm{d}\epsilon}{\exp\left[\frac{(\epsilon-\mu)}{k_B T}\right] - 1} \tag{1.3}$$

where $\epsilon = 0$ corresponds to the ground state of the system and the expected occupation of a state at large energy ($\epsilon \to \infty$) is zero. The density of states is determined entirely by the Hamiltonian and dimensionality of the system. For a free-particle in n-dimensions with spin-degeneracy g_0, the density of states per volume is given by,

$$\frac{g(\epsilon)}{V} = \frac{g_0}{2^n \pi^{n/2} \Gamma\left(\frac{n}{2}+1\right)} \epsilon^{(n-2)/2} \left(\frac{2m}{\hbar^2}\right)^{n/2} \frac{n}{2}. \tag{1.4}$$

Evaluating the integral in 1.3 leads to an expression for the density,

$$\left(\frac{N}{V}\right) = \left(\frac{N}{V}\right)_{\epsilon=0} + g_0 \frac{\mathrm{Li}_{n/2}\left(\mathrm{e}^{\mu/k_B T}\right)}{\lambda_T^n}. \tag{1.5}$$

The function $\mathrm{Li}_{n/2}$ is the polylogarithm function of order n/2. The density of the ground state is simply,

$$\left(\frac{N}{V}\right)_{\epsilon=0} = \frac{g_0}{V}\left(\frac{\mathrm{e}^{\mu/k_B T}}{1 - \mathrm{e}^{\mu/k_B T}}\right). \tag{1.6}$$

and the usual definition of the thermal wavelength,

$$\lambda_T = \frac{h}{\sqrt{2\pi m k_B T}} \tag{1.7}$$

is used.

The chemical potential of a Bose system is required to be less than or equal to the

ground state energy. As the chemical potential approaches the ground state of the system, the population increases. As $\mu \to 0$, the density of the system increases as the argument of the polylogarithm function goes to unity:

$$\lim_{\mu \to 0} \left[\left(\frac{N}{V} \right) - \left(\frac{N}{V} \right)_{\epsilon=0} \right] = \begin{cases} g_0 \left(\frac{1}{\lambda_T} \right)^n \zeta(n/2), & n > 2 \\ \infty, & n \leq 2. \end{cases} \tag{1.8}$$

Physically, this means that for free particles of dimensionality two or less, the density of particles in excited states can increase without bound. For dimensionality greater than two, the density of particles in excited states is capped at a particular value, determined by the temperature. It is also easy to see that the expression for the density of the ground state in (1.6) - typically zero in the macroscopic limit ($V \to \infty$) - can approach a finite, non-zero value as the chemical potential approaches zero. But - as shown - this will only happen at finite total density if the density of states leads to a convergent expression in (1.8).

Alternatively, at fixed density, particles will begin to condense into the ground state below some critical temperature. This can easily be found from (1.8), by solving for the temperature. For example,

$$T_{crit} = \left(\frac{N/V}{g_0 \zeta(3/2)} \right)^{2/3} \frac{2\pi\hbar^2}{m k_B} \tag{1.9}$$

is the critical temperature for the three dimensional case.

In Fermi systems, Pauli exclusion limits the number of particles that can be packed in low lying energy states. With bosons, the opposite seems true. A limited number of particles can be packed into the excited states of the system. Above a critical density, any additional bosons will condense into the ground state. We see that for interacting particles, the interparticle separation associated with this critical density is on the order of the thermal wavelength. The typical intuitive picture is that the effects of Bose-Einstein statistics start becoming important when the particle wave functions begin to overlap.

It is worth mentioning that when particle number is not conserved, the chemical potential is fixed to the ground state energy. One canonical example of this is the black-body problem, where a photon gas is held in equilibrium with a perfect absorber at a fixed temperature. As the system approaches zero temperature, the population of photons simply goes to zero.

There are other interesting signatures of Bose statistics, even in systems without particle number conservation; the presence of stimulated emission of photons in an optically active system with significant population inversion is the working principle behind lasers.

The above argument for condensation into the ground state was roughly the conclusion Einstein came to after reading Bose's work; he published a paper predicting BEC in 1925 [4]. According to a review of the history of BEC by Griffin,

> (N)othing much happened concerning BEC until 1938. Apparently a major reason was because George Uhlenbeck criticized Einstein's prediction of a 'phase transition' by arguing it would not occur in a finite system...Second-order phase transitions were not understood yet and Uhlenbeck's criticism was generally accepted. [5].

This criticism mirrors similar discussions as to what constitutes a "true" BEC, particularly in two-dimensions - where long-range order is technically forbidden - and in non-equilibrium systems. Nonetheless, over the following decades there would be a number of experimental observations that can be attributed to the surprising properties of bose systems.

1.1.1 Superfluidity and Superconductivity

The discovery of the superfluid He-II phase of liquid ^{4}He is an early experimental appearance of Bose-Einstein condensation, though unambiguous evidence of this would not be found for many years. Observation of the sharp drop in viscocity and large thermal conductivity in the late 1930's[6, 7], led theorists Fritz London [8] and Laszlo Tisza [9] to predict that BEC was involved.

It was shown by Landau that superfluidity will break down above a critical velocity when the elementary excitations are phonon-like; i.e., when the energy dispersion relationship is linear at low energy [10]. Landau's argument was that excitations out of the system will be spontaneously generated if doing so lowers the energy of the system. Applying this condition to a liquid moving at some fixed velocity with respect to a stationary capillary tube, excitations will be created if the speed of flow is above a critical value, determined by the dispersion relationship. If the liquid cannot shed energy and momentum, it will have no viscosity. Phonon-like elementary excitations are characteristic of a Bose system near its ground state; thus, virtually all experimentally observed cases of superfluidity are

accompanied by condensation. For many years, superfluidity was the only concrete evidence of condensation in ^{4}He.

The most definitive evidence of Bose-Einstein condensation is a macroscopic occupation of particles in the ground state of the system. However, due to the strongly interacting nature of liquid helium, this measurement is not as straightforward as it would be for a weakly interacting gas. Deep inelastic neutron scattering has been used to measure the momentum-space distribution of liquid helium [11]; while a sharp peak at $k = 0$ was never observed, careful measurements of temperature dependence of the scattering at $k = 0$ - as recently as 2000 - were consistent with a projected condensate fraction of around 7% at absolute zero[12]. Another, relatively recent experiment (1998) showed that quantum evaporation of helium atoms induced by a collimated beam of photons produces a sharply peaked angular distribution, suggesting a large fraction of atoms intially at zero in-plane momentum (with respect to the surface) [13].

Superconductivity is essentially superfluidity in a charge-carrying system; but the connection between most superconductors and BEC is not as direct. In 1911, Heike Kamerlingh-Onnes observed a sharp drop in the resistance of extremely pure mercury below 4.2 K; the final value of the resistance was below the measureable range of his instruments [14]. Experiments in the 1930s revealed a discontinuity in the heat capacity of superconducting metals, of varying magnitude dependening on the relative contribution of electrons and phonons in a particular metal [15]. The ability of superconductors to expel an externally appliced magnetic field was observed in 1933 by Meissner and Oschenfeld, the first concrete result that suggested that a superconductor is not just a material with perfect conductivity [16].

The connection between superconductivity and BEC was not firmly established until the late-1950's. It was perhaps suspected by Fritz London, who published a phenomenological model of superconductor electrodynamics with his brother, Heinz, in 1935 [17]. BCS theory - the work of theorists Bardeen, Cooper and Schrieffer in 1957 - predicted that an electronic pairing mechanism strong enough to overcome the screened Coulomb repulsion would cause electrons to form correlated, integer-spin pairs. In metallic superconductors, this pairing mechanism was found to be mediated by the electron-phonon interaction [18]. This process is now typically referred to as "Cooper pairing".

The strong correlation between Cooper pairs in a BCS superconductor is sometimes referred to as a pseudo-BEC [19], primarily because it occurs in a Fermi system. Of course, virtually every experimental example of Bose-Einstein condensation occurs in systems of composite bosons (bosons that are built out of fermions that are tightly bound together). Cooper pairs are somewhat different, in the sense that the electrons do not form a tightly bound pair in real-space. Instead, two electrons of opposite momentum and spin form correlated pairs. In Fermi systems where both states are possible in different regimes, it is possible to observe the transition from the typical BCS state to a condensate of tightly bound composite bosons; this transition is called "BEC-BCS crossover" [20].

In the decades following BCS theory, the study of superconductivity moved forward with a focus on finding higher critical temperature superconducting materials. Alloys based on copper oxide have been particularly fruitful, instigated by studies of the Ba-La-Cu-O system in 1986 (which suggested a T_C of around 30 K) [21] and with the record set in 1993 by the Hg-Ba-Cu-O system at high pressure (with $T_C = 150$ K) [22]. The exact pairing mechanism for high temperature superconductors is still not certain, although there is a general understanding that the system can be modeled as a doped Mott insulator [23] Within this picture, one dominant theory for pairing involves anti-ferromagnetic exchange effects [24].

1.1.2 Cold Atom Experiments

A dilute, spin-polarized hydrogen gas was proposed as candidate for BEC, first in 1959 by C.E. Hecht [25] and again in 1976 by Stwalley and Nosanow [26], by virtue of the prediction that it would remain gaseous down to absolute zero. Spin-polarized hydrogen became the focus of BEC research throughout the 1980s. The pace of research was set by the invention of new techniques for achieving extremely low temperatures in this system - magnetic trapping and evaporative cooling made $100\mu K$ achievable by 1991 [27, 28]. Unlike ^{4}He, atomic gases provided an opportunity to study a weakly-interacting Bose gas. The weakly interacting case is significantly easier to deal with theoretically and - it turns out - lends to simpler experimental intepretation.

In the early-90s, groups at MIT, JILA and Rice University began applying these methods, in conjunction with new laser cooling techniques, to dilute alkali gases. Alkali systems lack some of the advantages of spin-polarized hydrogen; specifically, they are heavier - which corresponds to a lower BEC transition temperature - and were predicted to exhibit bound states at low temperature. However, alkali gases have the advantage of being more responsive to evaporative cooling. The scattering mechanisms responsible for the formation of bound states also turned out to be strongly suppressed at low temperature[27, 29]. The first atomic condensate is credited to the JILA group headed by Cornell and Wieman (working with Rb-87) [30] , followed shortly by the MIT group under Wolfgang Ketterle (working with Na-23) [31]. This work was recognized with the 2001 Nobel prize, which Wieman, Cornell and Ketterle shared equally. The onset of BEC was observed from a drastic peak in the momentum-distribution of the atoms, symptomatic of macroscopic occupation of the ground state.

1.1.3 Bose Einstein Condensation of Excitons

Solid state systems constitute another major experimental front in the study of BEC. Excitons - a type of quasiparticle typically occuring in solid state systems - will be the primary focus of this work.

Recall that semiconductors are characterized by a valence band and a conduction band, with an energy separation called the band gap. The Fermi energy is located mid-gap, meaning that at absolute zero, all valence band states are occupied and all conduction band states are empty. When a semiconductor absorbs a photon with energy greater than the band gap energy, an electron is promoted from the valence band to the conduction band. The vacant state can be treated as a positively charged particle, calle a hole. Thinking about the ground state of the semiconductor as the vacuum, this process can be pictured as a photon spontaneously generating an electron-hole pair. If the electron and hole have sufficiently low kinetic energy, they will bind together in a manner analogous to positronium. The close proximity of the two means that they will quickly recombine; but, while this quasiparticle exists, it is referred to as an exciton. Constructed out of two half-integer spin particles, an

exciton has net integer spin and will act like a boson. In principle this is no different than in atomic systems; atoms are also composite bosons composed of half-integer spin protons, neutrons and electrons. At very high density, when the wave functions of the underlying fermions start to overlap, the approximation of excitons as bosons begins to break down; however, it has been rigorously shown that excitons can be treated as a Bose gas, with some modifications due to fermionic effects [32].

Large, expensive and complicated experimental setups are a necessary requirement for the study of cold atomic gases. This is primarily a result of the heroic effort needed to achieve temperatures in the microkelvin and nanokelvin range. From the perspective of commercial application, this is a huge barrier. Excitonic systems circumvent these issues in several ways. Excitons are orders of magnitude less massive than atoms. This corresponds to a drastically higher critical temperature. Even a critical temperature of above 2 K drastically reduces the complexity of the experiment; but, practically speaking, any sort of large-scale device application would need to work near room temperature, eliminating the need for cryogenics altoghether. Semiconductor systems are also advantageous in the sense that relatively complex structures can be cheaply fabricated on a semiconductor chip. In other words, compared to similar experiments in cold atomic gases, semiconductor systems are compact, versatile, and cheap.

While the study of Bose-Einstein condensation in semiconductor systems is interesting in-and-of itself, it can also lead to a deeper understanding of the optical and electrical properties of semiconductors under exotic conditions. It opens the possibility of observing other novel, low temperature phase transitions. And, on a more basic level, it can teach us about the physics of semiconductors at low temperatures, which can then potentially be extended to build novel, room temperature devices.

1.1.4 Survey of Excitonic BEC Research

Bose-Einstein condensation of excitons was first suggested in 1962 in two short theory papers by Blatt, et. al. [33] and Moskalenko [34]. Several decades prior to the observation of atomic BEC, the outlook for excitons was extremely favorable. Excitons have a much lower mass -

on the order of the electron mass - compared to atoms, which implies a much higher critical temperature (note the dependence of the thermal wavelength on mass in (1.7)).

There are a few requirements for the observation of BEC in excitonic systems. First, the exciton lifetime need to be at least comparable to the thermalization time. In order for excitons to condense to the ground state before being re-emitted as a photons, they must undergo some process that allows them to give up energy and scatter down to the ground state.

Secondly, if the average thermal energy of the system - k_BT - is larger than the exciton binding energy, excitons may easily ionize. In this case, electrons and holes will form a plasma and will not act as paired bosons. This can also happen at high density, if the Coulomb interaction between electrons and holes becomes sufficiently screened. In principle, if the BEC critical temperature is higher than the exciton formation temperature, below that temperature excitons may immediately condense as soon as they begin pairing. In the search for room temperature BEC, a high binding energy would be necessary.

Thirdly, the crystal must be pure enough that the excitons are not trapped in localized defect states at the transition temperature. Localization can make it difficult to observe any effects related to condensation, which are typically characterized by long-range order.

The possibility of room temperature BEC is a huge selling point, so early studies focused on excitons or excitonic molecules with large binding energy (ideally, greater than k_BT $\approx$ 25 meV, associated with room temperature) [35]. In 1972, Kuroda et al. observed the appearance of sharp luminescence line under pulsed excitation in cadmium selenide at low temperature (1.8 K), and interpreted it as a BEC of biexcitons [36]. A critique of this work in 1974 argued that this was unlikely due to the role of crystal heating under pulsed excitation for the claimed experimental parameters; the authors instead identified the sharp luminescence line as an exciton complex bound to a neutral donor site [37].

Copper chloride (CuCl) likewise exhibits a strongly bound biexciton (BX) state; signatures of bose effects in CuCl were observed in the 1980's and 1990's, including a thermal distribution similar to a Bose-Einstein distribution near $\mu = 0$ (measured from the BX luminescence spectrum), stimulated scattering into the ground state [38], and stimulated enhancement of an optical phase conjugation signal in four-wave mixing experiments [39].

However, the biexciton state in CuCl is characterized by a short radiative lifetime (1-10 ns), and effects indicative of Bose statistics are only observed with resonant excitation; this suggests that it is only possible to observe a non-equillibrium condensate in this system [40]. In a non-equillibrium condensate, the coherence of the ground state is seeded by the coherence of the pump laser. In a system within the density and temperature regime necessary for BEC, it should condense even when excitons are injected into the system incoherently [3].

A third major candidate system for BEC, studied extensively in the 1980's and 1990's, is cuprous oxide (Cu_2O). The excitonic ground state in Cu_2O is bound at room temperature and is forbidden by symmetry to undergo direct recombination, giving it a long radiative lifetime - measured experimentally to be as large as 13 μs at low temperature (10 K) [41]. The primary obstacle to the observation of BEC in Cu_2O systems is the prevalence of Auger recombination at high density; Auger recombination drastically reduces the lifetime and results in a significant source of heating [35]. In the last few years, there have been claims of BEC in Cu_2O at low density and - necessarily - low temperature (less than 1 K) [42, 43].

There has been remarkable progress in the study of BEC in semiconductor microcavity systems in the last decade. A microcavity is an optical cavity formed between two Bragg reflectors, grown with alternating semiconductor layers (for example, GaAs and AlAs). The structure is designed so that quantum wells sit at the anti-nodes of the cavity mode; if the quantum well exciton energy is near the resonant energy of the cavity, it is possible to produce excitons strongly coupled to cavity photons. An exciton-polariton is a quasi-particle that is a quantum superposition of an exciton and a cavity photon. The most attractive attribute of this system is that the effective mass of the polariton is based on the exciton and photon mass. Due to the extremely low effective in-plane mass of a cavity photon, the effective mass may be on the order of 10^{-4} times the bare electron mass [44]. This implies a significantly higher critical temperature, compared to a system of bare excitons.

While the lifetime of microcavity polaritons is typically short, it is possible to reach some degree of thermalization by working with polaritons that have a stronger exciton fraction [4].

[3] Or, if they are injected with a coherent source, but undergo repeated scattering, which would result in a loss of driven coherence.

[4] Polariton-polariton scattering is primarily mediated by scattering between the exciton component; scattering between cavity photons is typically negligible.

In 2007, several groups published strong evidence of condensation in microcavities, including spatial coherence and momentum-space narrowing [44, 45, 46]. These results differ from the earlier observation of non-equilibrium condensation, in the sense that coherence was observed even with incoherent (non-resonant) pumping. In microcavity samples with long polariton lifetime, Nelsen et. al recently observed coherent, dissipationless flow of polaritons above a critical density; the coherent behavior was observed to persist up to 200 μm from the incoherent pump source [47].

Coupled quantum well and electron-hole bilayer systems have also been extensively studied in the past two decades. Microcavity polaritons can be thought of as a weakly-interacting Bose gas; as will be discussed later, spatially-indirect excitons exhibit a strong dipole-dipole repulsion and can not be thought of as weakly interacting. Much like the search for signatures of BEC in superfluid helium (another strongly interacting system), unambiguous observation of an indirect exciton BEC has proven to be challenging. But the search may also reveal interesting new physics that does not appear in weakly interacting systems. Indirect excitons are the major focus of the work presented here, so the current state of the field will be reviewed in a bit more detail in Chapter 3 - after the appropriate conceptual background has been established.

1.2 BAND STRUCTURE OF GAAS

Gallium arsenide (GaAs) is a III-V compound semiconductor with a direct bandgap, meaning that the lowest point of its conduction band and the highest point of its valence band are at the same point in momentum-space. At sufficiently low temperature, electrons and holes will inhabit states primarily near the bottom of the valence band and top of the conduction band, respectively.

The key feature of direct bandgap semiconductors is that an electron in the valence band can be optically excited to the conduction band without the assistance of phonons [5]. A plot

[5] Or, conversely, an electron in the conduction band can drop back to the valence band by emitting a photon.

of the band diagram of bulk GaAs is shown in Figure 1, along with a sketch of the photon dispersion relationship centered at the top of the valence band,

$$E(\vec{k}) = \frac{\hbar c|\vec{k}|}{n_{GaAs}} \tag{1.10}$$

where n_{GaAs} is the index of refraction of GaAs (approximately 3.7 in the near-infrared [48]). In order for a valence band electron to be promoted to the conduction band by a photon, energy and momentum must be conserved. This illustrates that absorption (and emission) will occur almost entirely near band-center.

The direct gap of GaAs is approximately 1.43 eV at room temperature and 1.52 eV at low temperature (below 10 K) [48], corresponding to photon wavelengths of 867 nm and 815 nm respectively. This puts the band edge absorption/emission in the near-infrared region. A more detailed discussion on luminescence in GaAs is covered in Chapter 2.

The band structure of a crystal is built from the hybridization of the atomic orbitals that make up the lattice. Energy bands are formed when a large number of discrete atomic levels are coupled together, forming a continuum of states.

The spin structure of the electrons and holes in a semiconductor are determined by the symmetry of the states that make up the valence and conduction bands. In GaAs, the valence band is composed of a hybridization of the $4s^2 4p^1$ valence states in gallium and the $4s^2 4p^3$ valence states of arsenic; this results in a p-like valence band and an s-like conduction band[1]. Electrons in the conduction band have total angular momentum $j = \frac{1}{2}$, corresponding to a state with spin-$\frac{1}{2}$ and zero orbital angular momentum. Meanwhile, the uppermost valence band electrons correspond to states with orbital angular momentum $\ell = 1$ and spin-1/2, meaning they have total angular momentum of $j = \frac{3}{2}$.

To calculate the band structure, one must solve for the electron eigenstates and eigenvalues for the periodic potential defined by the crystal lattice of GaAs. While in principle this is a difficult problem, it has also been one of the central tasks of solid state physics in the past century, so there is a well-established methodology to deal with it. Some of the main points will be outlined here, to give the reader some physical intuition of the system. For more detail, refer to discussions of $k \cdot p$ theory and the Luttinger-Kohn model in Chuang [1] or Winkler [49]. This overview closely follows the discussion and notation in Chuang's work.

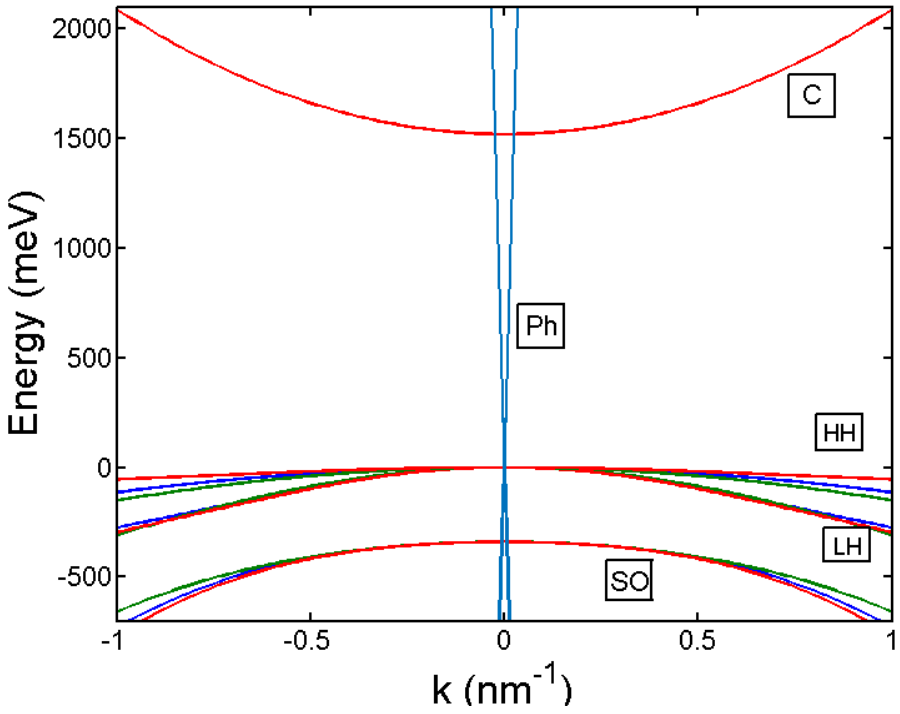

Figure 1: A plot of the six highest valence bands and two lowest conduction bands of bulk GaAs using the six-band Luttinger-Kohn model at low-temperature. Shown is a cross-section of the dispersion relationship, $E = E(k_x, k_y, k_z)$ along the (100) (blue), (110) (green), and (111) (red) directions. Note that the heavy hole (hh), light hole (hh), split-off (so) and conduction bands (c) are all doubly degenerate. At k = 0, the hh and lh band splitting goes to zero, leading to a four-fold degeneracy. The photon dispersion curve is shown to illustrate that absorption (and emission) only occurs with small momentum transfer (in effect, near k = 0)

.

We start with Schrodinger's equation for an electron in the crystal lattice, including spin-orbital coupling,

$$\hat{H}\Psi(\vec{r}) = \left[\frac{p^2}{2m_0} + V(\vec{r}) + \frac{\hbar}{4m_0^2c^2}\vec{\sigma}\cdot\vec{\nabla}V\left(\vec{r}\right)\times\vec{p}\right]\Psi(\vec{r}) = E\Psi(\vec{r}). \tag{1.11}$$

In general, the form of the potential due to the crystal lattice, $V(\vec{r})$, can be very complicated. This problem is made tractable by exploiting the periodicity of the lattice. Periodicity requires that any physically measureable quantity in the crystal must have the same periodicity. Therefore, the probability density of an electron must be the same in every unit cell. A family of wave functions that satisfy this condition is given by Bloch's theorem,

$$\Psi(\vec{r}) = e^{\mathrm{i}\vec{k}\cdot\vec{r}}u_{n\vec{k}}(\vec{r}) \tag{1.12}$$

where term $u_{n\vec{k}}(\vec{r})$ is a function that has the same periodicity as the crystal lattice. The plane-wave prefactor allows the wave function to have a phase shift between unit cells, which has no effect on the electron probability distribution $|\Psi|^2$, but which does contribute to the kinetic energy. By plugging this solution into Schrodinger's equation, one can generate an eigenvalue equation explicitly in terms of $u_{n\vec{k}}$:

$$\left[\frac{p^2}{2m_0} + \frac{\hbar\vec{k}\cdot\vec{p}}{m_0} + V(\vec{r}) + \frac{\hbar}{4m_0^2c^2}\sigma\cdot\nabla V\left(\vec{r}\right)\times\vec{p}\right]u_{n\vec{k}}(\vec{r}) = \left[\epsilon_{n\vec{k}} - \frac{\hbar^2k^2}{2m_0}\right]u_{n\vec{k}}(\vec{r}). \tag{1.13}$$

Perturbation theory can then be used to consider solutions near some point of high symmetry. For example, around $\vec{k} = 0$, the conduction-band is s-like and valence-band is p-like, so it is appropriate use the appropriate spherical harmonics as a basis ($|S\rangle$ and $|X\rangle$,$|Y\rangle$,$|Z\rangle$, respectively). In the Luttinger-Kohn model, the six highest valence bands are treated explicitly, while the effect of the conduction band and lower lying valence bands are taken into account through experimentally determined model parameters. The basis-states of the Luttinger-Kohn model are as follows:

$$\left|\frac{3}{2},\frac{3}{2}\right\rangle = \frac{1}{\sqrt{2}}\left|(X+\mathrm{i}Y)\right\rangle\left|\uparrow\right\rangle \tag{1.14}$$

$$\left|\frac{3}{2},\frac{1}{2}\right\rangle = -\frac{1}{\sqrt{6}}\left|(X+\mathrm{i}Y)\right\rangle\left|\downarrow\right\rangle + \sqrt{\frac{2}{3}}\left|Z\right\rangle\left|\uparrow\right\rangle \tag{1.15}$$

$$\left|\frac{3}{2},-\frac{1}{2}\right\rangle = \frac{1}{\sqrt{6}}\left|(X-\mathrm{i}Y)\right\rangle\left|\uparrow\right\rangle + \sqrt{\frac{2}{3}}\left|Z\right\rangle\left|\downarrow\right\rangle \tag{1.16}$$

$$\left|\frac{3}{2},-\frac{3}{2}\right\rangle = \frac{1}{\sqrt{2}}\left|(X-\mathrm{i}Y)\right\rangle\left|\downarrow\right\rangle \tag{1.17}$$

$$\left|\frac{1}{2},\frac{1}{2}\right\rangle = \frac{1}{\sqrt{3}}\left|(X+\mathrm{i}Y)\downarrow\right\rangle + \frac{1}{\sqrt{3}}\left|Z\uparrow\right\rangle \tag{1.18}$$

$$\left|\frac{1}{2},-\frac{1}{2}\right\rangle = \frac{1}{\sqrt{3}}\left|(X-\mathrm{i}Y)\downarrow\right\rangle - \frac{1}{\sqrt{3}}\left|Z\uparrow\right\rangle. \tag{1.19}$$

Evaluating the matrix elements for the Hamiltonian (1.13) perturbatively in this basis up to order k^2 results in the Luttinger-Kohn Hamiltonian. For simplicity, the terms corresponding to the the states in the splitoff band, (1.18) and (1.19), will be neglected. This leaves a 4×4 matrix,

$$H_v = -\begin{bmatrix} P+Q & -S & R & 0 \\ -S^* & P-Q & 0 & R \\ R^* & 0 & P-Q & S \\ 0 & R^* & S^* & P+Q \end{bmatrix}. \tag{1.20}$$

where each term depends on $\vec{k}$, as follows:

$$P = \frac{\hbar^2\gamma_1}{2m_0}\left(k_x^2 + k_y^2 + k_z^2\right), \tag{1.21}$$

$$Q = \frac{\hbar^2\gamma_1}{2m_0}\left(k_x^2 + k_y^2 - 2k_z^2\right), \tag{1.22}$$

$$R = \frac{\hbar^2}{2m_0}\left[-\sqrt{3}\gamma_2\left(k_x^2 - k_y^2\right) + \mathrm{i}2\sqrt{3}\gamma_3 k_x k_y\right], \tag{1.23}$$

$$S = \frac{\hbar^2}{2m_0}2\sqrt{3}\gamma_3\left(k_x - \mathrm{i}k_y\right)k_z. \tag{1.24}$$

Using a 4×4 matrix that excludes the coupling to the split-off band is a typical approximation at low k-values. The split-off band is associated with total angular momentum $j = \frac{1}{2}$, resulting from anti-aligned orbital angular momentum $\ell = 1$ and spin angular momentum $s = \frac{1}{2}$. The spin-orbit coupling associated with the anti-alignment of the spin and orbital angular momentum results in it having less energy than the aligned case, putting it 340 meV below the band-edge in bulk [1]; at k-values accessible to holes at low temperature, it is expected that coupling to the split-off band will be negligible.

The minus sign in front of the Luttinger-Kohn Hamiltonian indicates a decrease in energy as k increases, as would be expected for the valence band. In the exciton picture, this text will often treat holes as real particles with positive mass and positive charge, rather than as explicitly treating them as unoccupied valence band states. Keep in mind that energy changes that increase the energy of a hole actually decrease the valence band energy.

The four basis states treated here are associated with total angular momentum $j = \frac{3}{2}$; resulting from aligned orbital angular momentum $\ell = 1$ and spin angular momentum $s = \frac{1}{2}$. The $\left|\frac{3}{2}, \pm\frac{3}{2}\right\rangle$-states are called heavy-hole states, associated with the angular momentum entirely aligned or anti-aligned with +z-direction ($m_j = \pm\frac{3}{2}$). The $\left|\frac{3}{2}, \pm\frac{1}{2}\right\rangle$-states are called light-hole states, associated with an angular momentum projection along the z-axis of $\pm\frac{1}{2}$ ($m_j = \pm\frac{1}{2}$).

Applying the usual definition of the effective mass

$$m_{\text{eff}} = \frac{\hbar^2}{\left(\partial^2 E/\partial k^2\right)_{k=0}} \tag{1.25}$$

to the Luttinger-Kohn Hamiltonian, shows that the valence band states have different masses

Parameter	Value
γ_1	6.8
γ_2	1.9
γ_3	2.73
$m_{hh,z}/m_0$	0.333
$m_{lh,z}/m_0$	0.094
$m_{hh,\|\|}/m_0$	0.115
$m_{lh,\|\|}/m_0$	0.204
m_e/m_0	0.067

Table 1: Parameters of Luttinger-Kohn Model for GaAs [1]

in the z-direction than in the x- and y-directions (determined by the parameters γ_1, γ_2 and γ_3; see Table 1). The heavy-hole band is associated with a heavier mass in the z-direction and a lighter-mass in the plane perpendicular to z; the case for the light-hole band is reversed. These parameters are summarized in Table 1. Note that the bands are not entirely parabolic, due to the coupling terms R and S. This will be discussed in greater detail in Section 1.3. The conduction band is parabolic and exhibits the same effective mass in all propagation directions (this can be seen in Figure 1, where the energy cross-section for the conduction band is the same along the (100),(110) and (111) directions).

A few things are worth mentioning about the symmetry of gallium arsenide. In our discussion of quantum wells, the z-direction will be defined as the growth direction. But it is important to realize that this is completely arbitrary. At first glance, that seems incorrect; the heavy- and light-hole states exhibit different effective masses in the in-plane direction than in the z-direction. This seems to indicate there is something special about the z-direction. In fact, only reason for this apparent asymmetry is because the basis states used in this Hamiltonian are angular momentum eigenstates defined with respect to the z-direction. If one were to define the x-direction as the growth direction and re-define the

basis states consistently, the results should be identical. This is evident given that GaAs has a zinc blende structure (which is structurally identical to diamond cubic, except for the presence of two different types of atoms, and has cubic symmetry).

In the literature, the [100] and [001] crystallographic directions are used interchangeably to define the growth direction of quantum wells in GaAs - it is worth keeping in mind that these are, in fact, physically identical. Occasionally, wells are grown in the [111]-direction or [110]-direction; these types of structures will have different physical properties.

Likewise, the in-plane - [110] and $[1\bar{1}0]$ directions are typically interchangeable. In Chapter 2, it will be shown that under applied stress this symmetry is broken in our system by a small piezoelectric effect.

1.3 QUANTUM WELLS

A quantum well is a two-dimensional potential well[6] in the conduction band and/or the valence band, created by growing alternating layers of different semiconductors on top of one another. A Type-I quantum well is a structure where electrons and holes are trapped in the same layer, a type-II quantum well is a structure where they are trapped in different layers. A cartoon sketch of these geometries is shown in Figure 2. The structures studied in later chapters will all be type-I quantum wells.

A common quantum well system is where a compound semiconductor is alloyed with some other material to either raise or lower the bandgap. For example, aluminum arsenide (AlAs) is an indirect bandgap material with a larger gap at the Γ-point than GaAs, 3.03 eV at room temperature and 3.13 eV near absolute zero [1]. GaAs can be continuously alloyed with aluminum to increase its bandgap energy. This system is typically referred to as $Al_xGa_{1-x}As$, where x is a number between 0 and 1 that refers to the alloy fraction of aluminum in the material. As one might expect, at some alloy fraction the system transitions from direct-gap to indirect-gap. The maximum conduction band discontinuity - and quantum well barrier

[6]Two-dimensional in the sense that motion of carriers is confined in one dimension; they are free to move about in the plane of the quantum well.

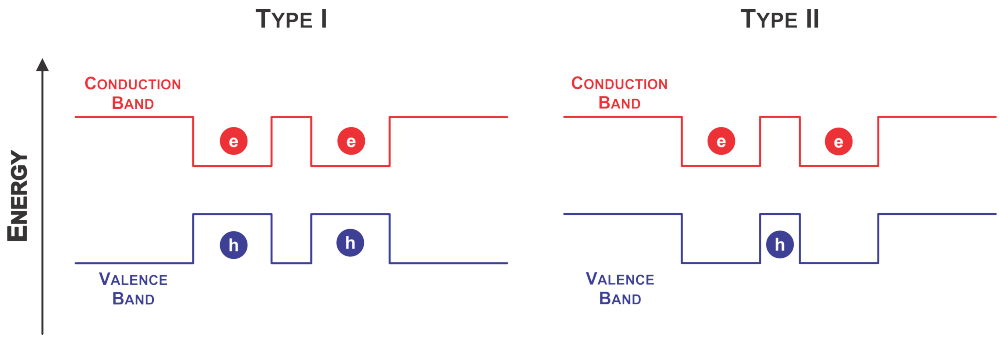

Figure 2: A sketch of the Type 1 and Type 2 quantum well energy band diagrams.

height - was measured by Maezawa, et. al., to occur around $x = 0.45$ [50].

The band structure of a quantum well system is determined by the band gap of the two materials, but also the band offset - the amount of the band gap discontinuity seen at the conduction band compared to the valence band. While band theory predicts that this should be determined entirely by the band gap and electron affinity of the two materials, the actual offset was somewhat contentious throughout the 1970's and 1980's; numerous electrical and optical measurements in the late-80's suggested a ratio ΔE_c:ΔE_v of between 60:40 and 70:30 [48]. In the calculations presented in later Chapters, a ratio of 67:33 is used [1].

The GaAs/AlAs system is an attractive choice for heterostructures composed of thin layers, because AlAs and GaAs have very similar lattice constants - 5.653 Å and 5.660 Å respectively, at room temperature [1]. This means that a layer of AlAs grown on top of a layer of GaAs will suffer very little lattice mismatch. When lattice mismatch between two materials is significant, it will either cause built-in strain near the interface between the two materials (if the mismatch is small) or will cause a large amount of disorder. Disorder in quantum wells can cause a number of issues, from trapping of carriers at defect sites at low temperature to poor carrier mobility due to carrier-defect scattering.

In terms of solving for the wave function, a quantum well can be treated as a finite 1D barrier in the growth direction[7]. It is also a typical approximation to de-couple the in-plane

[7]There is some additional complication due to the difference of the effective mass in the well and the barriers. This issue is addressed in detail in Appendix A

motion from the wave function in the confinement direction. A simple model wave function for a carrier in a quantum well is

$$\psi_{j,m_j,\vec{k}_{||},n}\left(\vec{r}_{||},z\right) = g_n(z)\mathrm{e}^{\mathrm{i}\vec{k}_{||}\cdot\vec{r}}\left|j,m_j\right\rangle \tag{1.26}$$

where the j and m_j quantum numbers describe the basis state for the Luttinger-Kohn Hamiltonian, the vector $\vec{k}_{||}$ defines the motion in plane, and the new quantum number - n - corresponds to the eigenstate of the 1D well in the confinement direction. This eigenstate, $g_n(z)$ is called an envelope function. The energy is often approximated as,

$$E = \frac{\hbar^2}{2m_{\mathrm{eff},z}}\left(\frac{\pi}{a}n\right)^2 + \frac{\hbar^2}{2m_{\mathrm{eff},||}}k_{||}^2 \tag{1.27}$$

where the first term is the confinement energy due to an infinite 1D well of width a. For the infinite-barrier case, the quantum number n can be any integer greater than one, and this set of basis functions defines a complete set.

For the finite-barrier case, there will be a few differences. First, there will be some amount of penetration of the wave function into the barrier. In (1.27), the confinement energy is based on the assumption that the wave function must go to zero at the well edges, fixing k_z at some multiple of $\frac{\pi}{a}$. For a better approximation of the finite well problem, it is necessary to define an effective well width, which is necessarily slightly larger than the physical well width [8].

Secondly, confined states will exist only as long as the confinement energy is less than the depth of the well. This means that for a finite-well, only a few confined states will exist, followed by a continuum of unbound states at higher energy. For the experiments discussed here, the average thermal energy will be significantly less than the gap between the lowest and second-lowest ($n = 1$ and $n = 2$) confined states. Using the infinite-barrier approximation, the gaps between the $n = 1$ and $n = 2$ electron, heavy-hole, and light-hole subbands are 85 meV, 17 meV, and 61 meV, respectively. The actual values will be slightly lower, but even 17 meV corresponds to a thermal activation energy of around 200 K; far greater than would be observed in our working range, typically 20 K or less.

[8] Penetration into the barrier increases as the confinement energy increases, so the effective well width will be larger for larger n.

Note that due to the effective mass difference between the heavy-hole and light-hole states in the z-direction, the confinement energy splits the two bands at $\vec{k}_{||} = 0$. This will leave the heavy-hole (with its larger mass in the confinement direction) as the lowest energy hole state; corresponding to the highest valence band. This also splits the degeneracy at valence band center; making it two-fold, rather than four-fold degenerate. In Figure 3, the band diagram of the lowest electron band and the lowest few hole bands are shown. They are not calculated in the infinite-well approximation discussed above, but using the full Luttinger-Kohn model; there are some subtleties to this calculation that will be discussed in Chapter 2, that lead to a momentum-space indirect bandgap in the light-hole band.

1.4 EXCITONS

An exciton is a bound-state formed by an electron and a hole due to the Coulomb interaction. The Hamiltonian that describes this system can be written as,

$$H = -\frac{\hbar^2}{2m_e}\nabla_e^2 - \frac{\hbar^2}{2m_h}\nabla_h^2 + V_e(\vec{r}_e) + V_h(\vec{r}_h) - \frac{e^2}{4\pi\epsilon}\frac{1}{|\vec{r}_e - \vec{r}_h|^2}. \tag{1.28}$$

In bulk, this expression looks very similar to the hydrogen atom - with the exception that the mass of the hole is comparable to that of the electron and cannot be neglected. Instead, one can write the solution in terms of the reduced mass,

$$\frac{1}{\mu} = \frac{1}{m_e} + \frac{1}{m_h}, \tag{1.29}$$

which will depend on the effective masses of the electron and hole in GaAs (see Table 1. Note that ϵ in (1.28) refers to the static dielectric constant in the medium. For GaAs, it is approximately $13\epsilon_0$ at room temperature (300 K) and $12.7\epsilon_0$ near absolute zero [48]. The eigenstates of this Hamiltonian will be the hydrogenic wave functions with a Bohr radius given by [51],

$$a_{ex} = \frac{4\pi\hbar^2\epsilon}{e^2\mu} \tag{1.30}$$

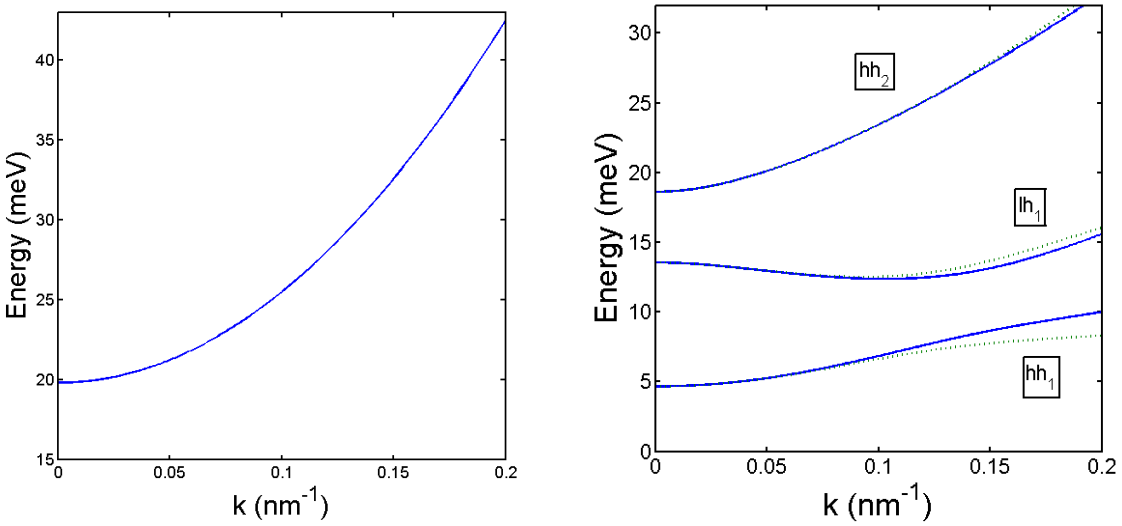

(a) (b)

Figure 3: Plot of the (a) electron and (b) hole energy bands of a 14 nm GaAs quantum well with $Al_{0.45}Ga_{0.55}As$ barriers, as a function of in-plane k. For the hole states, the lowest three subbands are shown with a cross-section along the (100) (blue, solid line) and (110) (green, dotted line) directions. Each subband is two-fold degenerate.

and a ground state energy of,

$$E_{bind} = -\frac{e^2}{8\hbar^2\epsilon^2}. \tag{1.31}$$

The binding energy of ground state excitons in bulk GaAs has been measured to be around 4 meV at low temperature (between 1 and 2 K) [52], which would correspond to a Bohr radius of around 14 nm. Recall that the lowest hydrogenic wave function is of the form,

$$\psi(\vec{r}) \propto \mathrm{e}^{-r/a_{ex}}. \tag{1.32}$$

In quantum wells, one effect of confinement is the enhancement of the exciton binding energy. An interpolation on measurements by Tarucha, et. al. show a binding energy of approximately 10 meV for 14 nm quantum wells in an GaAs/AlAs structure [53]. Measurements of the splitting between the 1s and 2s exciton energy levels by Miller, et. al. lead to a predicted binding energy of approximately 8 meV for the heavy-hole exciton and 9.5 meV for the light-hole exciton for 14 nm quantum wells in a GaAs/$Al_{0.37}Ga_{0.63}As$ structure [54]. In short, the general trend is that stronger confinement (either through higher barriers or narrower wells), leads to a higher exciton binding energy.

The role of confinement, which forces the electron and hole into greater proximity and lowers the binding energy, also shortens the lifetime. Measurements by Köhler, et. al., [55] show a 700 ps exciton lifetime for 21 nm wells, a 300 ps lifetime for 10.7 nm wells, and a 200 ps lifetime for 5 nm wells (all in GaAs/$Al_{0.3}Ga_{0.7}As$).

In single quantum wells, an applied electric field in the growth direction will cause excitons to polarize slightly within the well, lowering the overall energy slightly. Called the quantum-confined Stark effect, it will be more pronounced in wider or shallower wells - because the carriers are able to polarize more effectively in the z-direction - and is roughly quadratic with applied field. For 10 nm quantum wells with $Al_{0.32}Ga_{0.68}As$ barriers, Miller et. al. observed a roughly 20 meV shift of the hh- and lh-lines with an applied field of 100 kV/cm [56]. The separation of the electron and hole also results in a longer lifetime - an early experiment by Polland et. al. reported a huge enhancement in 20 nm quantum wells in an 100 kV/cm field - from just under 1 ns at zero field to approximately 100 ns - and a much smaller enhancement in 10 nm quantum wells - from around 0.5 ns at zero field to 1

ns at almost 180 kV/cm [57].

This lifetime enhancement can be drastically improved by using a system of two, closely coupled quantum wells (CQW). At zero-field, the two lowest states of two, identical coupled wells are roughly symmetric and anti-symmetric combinations of the single quantum well ground state (shown in Figure 4); the symmetric state will be the ground state, the anti-symmetric state will be higher by a value that depends on the energy height and spatial width of the barrier (stronger coupling leads to a greater splitting). Under an applied electric field, one well becomes energetically preferable for the electron and the other becomes preferable for the hole. In Figure 4, it is shown that the electron and hole very quickly become localized in their respective wells.

It was discussed in the previous section that the primary purpose of the coupled quantum well structure is to enhance the lifetime. A detailed description radiative recombination will be covered in Chapter 2, but the main ideas will be shown here. One might guess that, due to the spatial separation of the electron and hole in the CQW structure, the excitonic wave function will look much different.

There are several ways to solve for the excitonic wave function in quantum wells or coupled quantum wells. A typical variational solution that can be applied to both cases is [58, 59],

$$\Psi(x, y, z_e - z_h) = N g_e(z_e) g_h(z_h) \exp\left[\frac{-\sqrt{x^2 + y^2 + \alpha\,(z_e - z_h)^2}}{\lambda}\right] \tag{1.33}$$

where g_e and g_h are the single particle electron and hole ground state wave functions due to the quantum well confinement potential, x and y indicate the separation between the electron and hole in-plane, and α and λ are variational parameters. Physically, λ represents an effective Bohr radius and α is a unitless deformation parameter that takes into account distortion of the wave function due to confinement in the z-direction.

The numerical calculations of Takahashi et. al [58]., using this variational approach, do not specifically treat the geometry used in the experiments discussed in subsequent Chapters (14 nm quantum wells with a 4 nm barrier). For 14 nm quantum wells with 5 nm barrier in a $GaAs/Al_{0.3}Ga_{0.7}As$ system, a binding energy of around 5.5 meV is predicted at zero electric

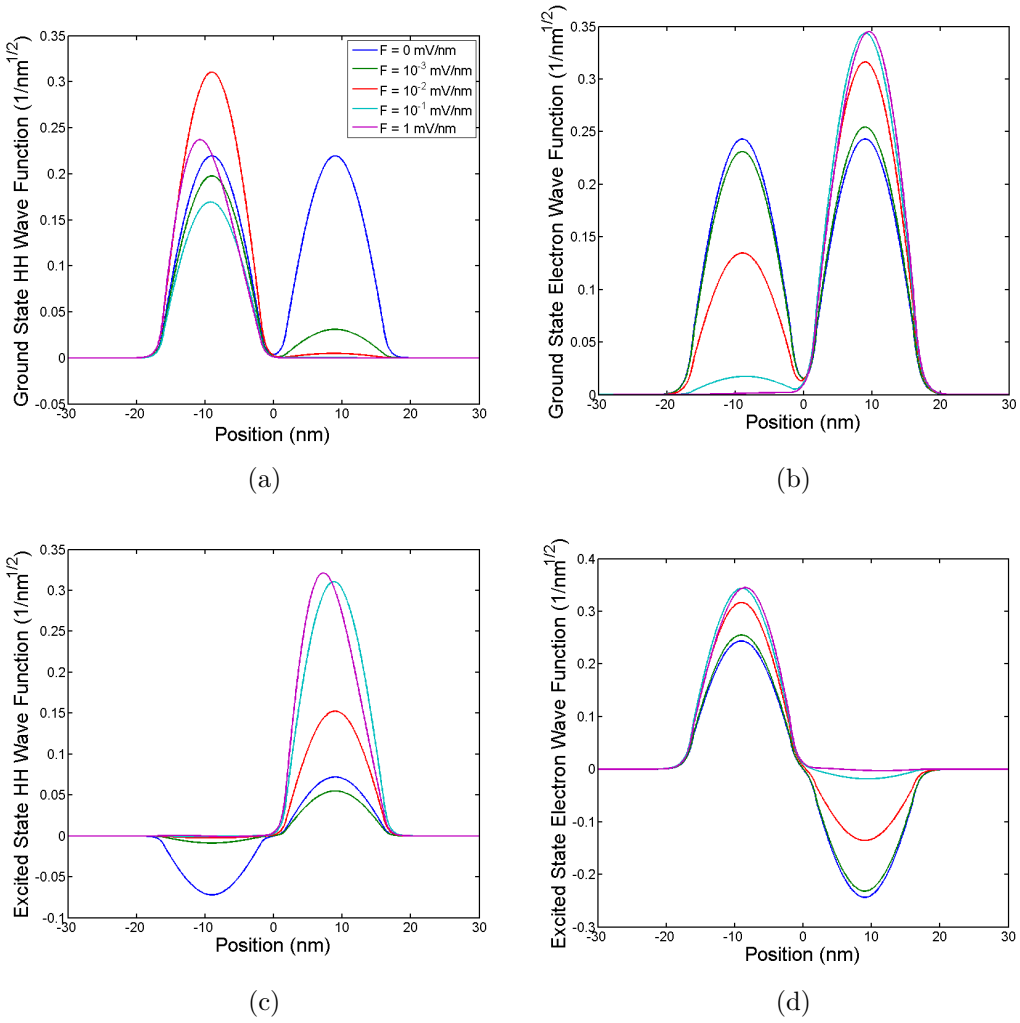

Figure 4: The calculated envelope wave functions for electrons and holes in a 14 nm-4 nm-14 nm CQWs with $Al_{0.45}Ga_{0.55}As$ barrier as a function of electric field in the growth direction. Shown are the wave functions for (a) the heavy-hole and (b) electron eigenstates localized to lower energy well, and the (c) heavy-hole and (d) electron eigenstates localized to the upper energy well.

field. At 1 mV/nm electric field, a similar structure with 10 nm quantum wells and a 4 nm barrier is predicted to have a binding energy of around 3.3 meV. With a similar calculation, Takahashi et al., predict the spatial extent of a heavy-hole exciton in this system to have an in-plane spatial extent of around 30 nm and an expected electron-hole separation in the growth direction of around 14 nm (close to the well-center to well-center distance).

Another approach is to choose a basis set of single-particle wave functions for the electron and hole and use the product of these states to model the two-particle wave function. After finding the matrix elements of the Hamiltonian (1.28) in the chosen basis, one can diagonalize the Hamiltonian to find the lowest eigenvalue. This method will only be accurate if the projection of the true ground-state wave function onto the chosen basis is almost unity (in other words, if the ground state wave function can be accurately expanded into the chosen finite basis).

A calculation pertaining to indirect excitons in 14 nm coupled quantum wells with a 4 nm barrier in a GaAs/$Al_{0.45}Ga_{0.55}As$ structure, was performed by Marzena Szymanska using this method with a large number of basis functions (for a similar calculation in a t-shaped quantum wire, 8000 basis functions were used) [60, 61]. A plot of the results of this calculation are shown in Figure 5 and Figure 6.

The relative oscillator strength cited in Figure 6 is proportional to the overlap integral between the electron and hole wave function and inversely proportional to the lifetime of the exciton. The exciton decay rate will be discussed in more detail in Chapter 2, but for now, it is enough to note that the exciton lifetime increases exponentially with applied field - at least in the range of interest. In this structure, radiative lifetimes greater than 10 μs has been observed; this is orders of magnitude greater than the single quantum well lifetime, which is typically less than 1 ns.

1.5 OUTLINE

Hopefully, this introduction has provided the reader with the basic tools necessary to understand the material discussed in the following chapters. In Chapter 2, the modeling of the

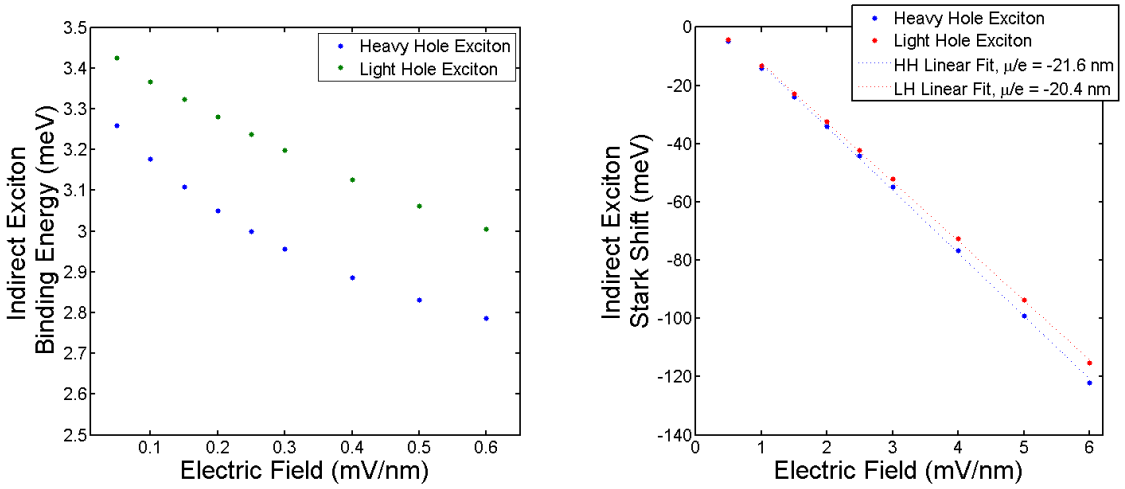

Figure 5: A plot of the binding energy and the Stark shift associated with the heavy-hole and light-hole excitons in a 14 nm coupled quantum well structure in GaAs/$Al_{0.45}Ga_{0.55}As$ with a 4 nm barrier. Calculation performed by M. Szymanska, as described in the text, to model the structure in Sinclair, et. al. [62].

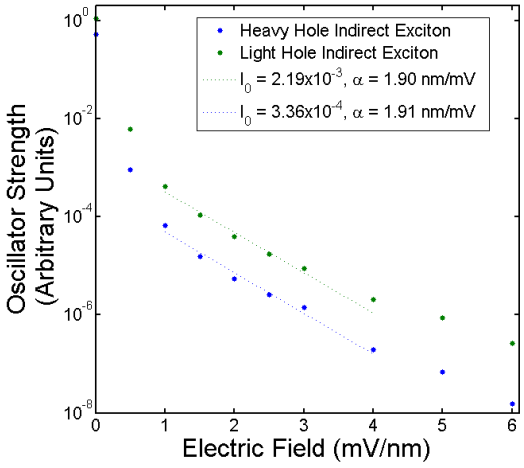

Figure 6: A plot of the oscillator strength associated with the heavy-hole and light-hole excitons in the structure described in Figure 5. Calculation also performed by M. Szymanska [62].

indirect exciton under an applied, uniaxial stress will be discussed in detail. The Pikus-Bir Hamiltonian will be applied to help model the energetic and luminescence properties of a coupled quantum well structure under strain and some features of the trapping potential in the low-stress regime. In Chapter 3, the machinery developed in Chapter 2, in conjunction with a density-dependent blue shift due to IX-IX interactions, will be used to treat the high stress, high density regime of our experiments. In particular, an effect where the luminescence at trap center darkens sharply will be discussed and an explanation will be proposed.

Chapter 4 departs from the photo-luminscence studies of the previous chapters, and focuses instead on a method for studying the transport of carriers in coupled quantum wells. The field of strongly correlated electron-hole and electron-electron bilayers will be reviewed. Then, the design and fabrication of a structure designed to measure the transport properties of optically injected indirect excitons will be discussed in detail, along with preliminary results.

2.0 MODELING EXCITON LUMINESENCE IN STRAIN TRAPS

This chapter covers the single-particle potential for a strain-based trapping setup for excitons in coupled quantum wells. While the primary interest of this work is the search for phase transitions in such systems - which are, of course, many-particle effects - it will be apparent in Chapter 3 that a strong understanding of the low-density physics is extremely important in separating phase transitions from phenomena that come about due to the symmetry breaking from the strain.

A cartoon depiction of a typical coupled quantum well structure designed for photoluminescence studies is shown in Figure 7a. The active part of the structure contains two GaAs quantum wells that are either 12 nm or 14 nm thick, separated by a 4 nm barrier of $Al_{0.45}Ga_{0.55}As$, and embedded betweeen thick layers of $Al_{0.45}Ga_{0.55}As$ on either side. It can be seen from Figure 4 in Chapter 1 that there is typically some penetration of the carrier wave functions into the central barrier, but the outer barriers are designed to be thick enough relative to the penetration depth that they can be approximated as infinitely thick.

The quantum well structure is capped on top and bottom by a superlattice - an alternating structure of GaAs and $Al_{0.45}Ga_{0.55}As$ layers, typically 6 nm and 8 nm thick respectively. The superlattice traps hot carriers injected into the system via the applied voltage bias and reduces the number of free carriers that reach the quantum wells. A high current passing through the wells tends to introduce a source of heating and can result in current filaments through the barrier, which can cause permanent damage to the structure. The superlattice is also designed to be transparent to light near the direct- and indirect-exciton luminescence wavelength.

The entire structure is grown on a heavily n-doped GaAs wafer and capped with a thin layer of heavily p-doped GaAs. Due to band-bending, this induces a built-in voltage across

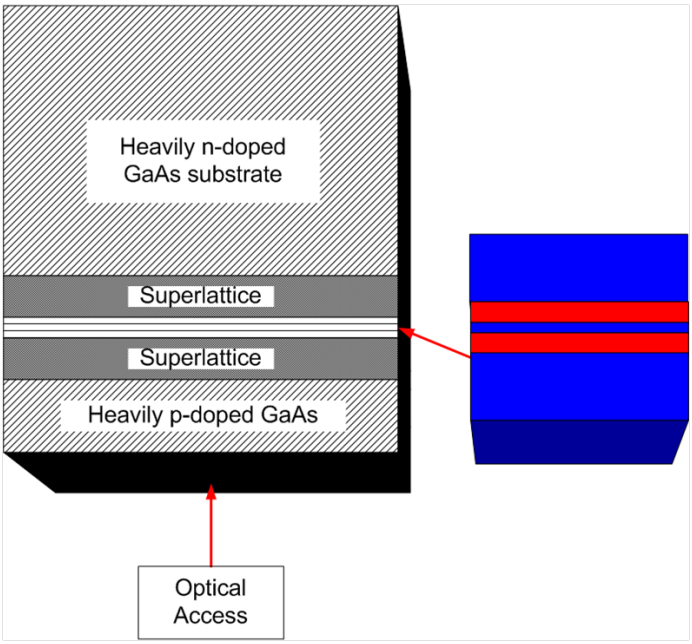

(a) Sample diagram

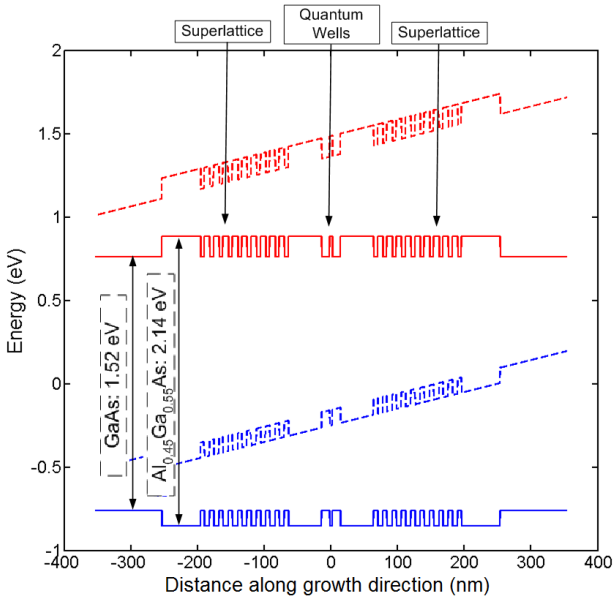

(b) Sample band structure

Figure 7: The (a) physical structure and (b) energy band diagram of a typical coupled quantum-well sample. In (a) the GaAs quantum wells - in red - are between $Al_{0.45}Ga_{0.55}As$ barriers - in blue. In (b), the spatial energy band diagram is shown for the flatband case (solid lines) and biased case (dotted lines).

the active region of the sample approximately equal to the band gap [1]. Due to the higher conductivity of the doped layers, doping also maked it easier to electrically bias the sample. In practice, to achieve good electrical contact to the doped substrate and capping layer, it is necessary to use indium foil - either pressed into mechanical contact with the sample or by thermally annealing it to the top and bottom. The insulating region of the sample is typically around 700 nm thick; meaning that the electric field induced by the built-in voltage is expected to be around 2 mV/nm, in the absence of any screening charge.

Pholuminescence spectroscopy is one technique commonly used to study the energy spectrum of the spatially direct and indirect excitons. A rough outline of the setup for this type of measurement is shown in Figure 8a. A laser diode designed to operate near the direct exciton resonant wavelength is used to optically pump the sample, which is mounted in either an immersion or continuous flow cryostat with optical access. Direct excitations - where electron-hole pairs are generated in the same well - are typically far more optically active than indirect excitions. These electron-hole pairs, once generated, cool down quickly to either form direct excitons or tunnel through the barrier to form the lower energy indirect excitons. Measurements of the electron and hole tunneling times suggested that both are less than a nanosecond (Oberli et. al reports a tunneling time of 10-75 ns for electrons in a similar structure [63], depending on bias voltage, and Leo et. al reports hole tunneling times around 800 ps at low electric field [64]). A typical direct exciton lifetime is expected to be on the order of ns, while the indirect exciton lifetime is observed to be on the order tens of μs at high bias [65].

The luminescence from the sample is imaged onto a spectrometer slit roughly 1 m away. When the spectrometer slit is open, the zero-order diffraction from the sample image can be directly projected onto an intensified charge-coupled device (ICCD) camera; providing a 2D, spatially resolved image of the luminescence. When the spectrometer slit is closed, a 1D spatial cross-section of the luminescence can be projected onto the spectrometer grating, which can then be used to create a spectrally resolved image of the luminscence. The

[1] The built-in voltage is close to the band gap because a high concentration of p-type dopants moves the Fermi level from mid-gap to near the valence band; a high concentration of n-type dopants moves the Fermi level near the conduction band. Therefore, from the top of the structure to the bottom of the structure, the change in the Fermi level is approximately equal to the band gap.

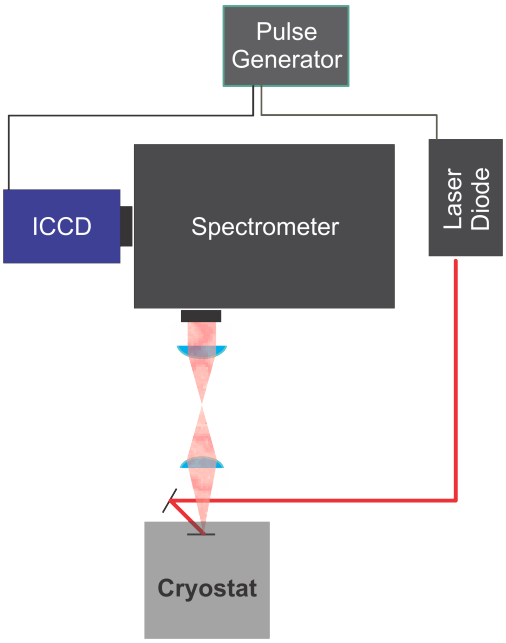

(a) Photoluminescence Measurement Setup

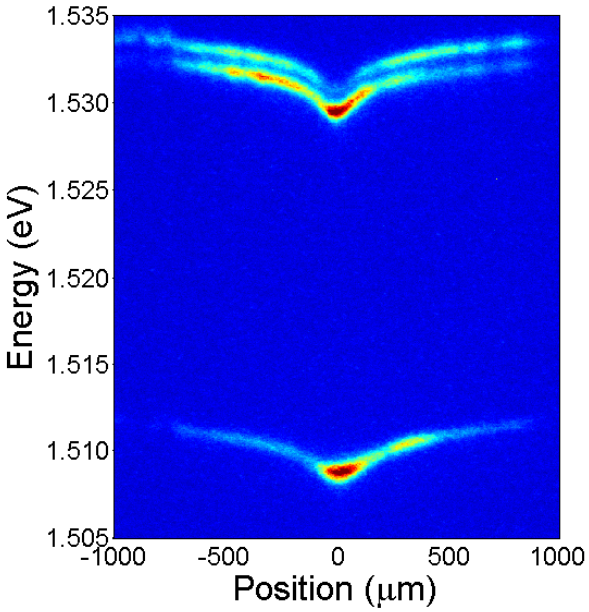

(b) Typical PL Spectrum when stress is applied at position 0 μm

Figure 8: A diagram of a typical time-gated photoluminescence measurement experimental setup and a spectrally resolved image of the stress trap. In CW experiments, laser diode can be ungated, or can be replaced with a He-Ne laser.

photoluminescence spectrum of a typical stressed coupled quantum well structure (p-i-n doping, 14 nm quantum wells separated by a 4 nm barrier) excited by a defocused He-Ne laser is shown in Figure 8b. The highest visible spectral line is associated with the direct exciton. Directly below that is a biexciton line. A biexciton is a molecule formed by two spatially-direct excitons; in regimes where the biexciton is stable, it will appear slightly under the direct exciton line, separated by a small biexciton binding energy. The lowest energy state in this spectrum is that associated with spatially-indirect excitons. Note that there is no stable indirect-biexciton; indirect excitons act as aligned dipoles and will typically have a repulsive interaction, thus one would not expect them to form bound pairs.

To summarize, there are a few things one can verify just from looking at the luminescence. First, both the direct and indirect luminescence is typically visible; this confirms that the indirect exciton formation rate is not drastically more or less than the direct exciton lifetime. If the direct exciton lifetime were much shorter than the indirect exciton formation rate, all photoexcited carriers would decay as direct excitons and no indirect states would form. If the direct exciton lifetime were much longer, all carriers would decay as indirect excitons and the DX line would be invisible. However, the fact that the DX and IX lines are typically on the same order of magnitude of intensity suggests that the population of indirect excitons is much greater than direct excitons; otherwise the IX line would be much dimmer, due to the much lower IX radiative rate. In steady state, this may be somewhat of a self-limiting process; the presence of indirect excitons tends to cancel out the local applied electric field, blue shifting the energy, and potentially slowing the tunneling rate.

The light-hole indirect exciton, which should lie between the heavy-hole direct exciton and the heavy-hole indirect exciton luminescence, is typically invisible at low stress. It will be shown later in this Chapter that the hh-lh splitting decreases with applied stress; when the two lines are near-resonance, the light-hole line is typically visible. At low stress, one explanation is that there is not a metastable population of light-hole indirect excitons; otherwise some luminescence from them would be visible. Another explanation, suggested by Figure 3, is that the light-hole valence band is slightly momentum-space indirect at low stress, which would suppress the recombination rate.

2.1 TRAPPING

It was shown in Section 1.1 using a non-interacting model that condensation will not occur for free particles in two dimensions. For the case of particles in a harmonic trap, the result will be different. In two dimensions, the density of states of a harmonic trap with spring constants ω_x and ω_y is

$$g(\epsilon) = g_0 \frac{\epsilon}{\hbar^2 \omega_x \omega_y}. \tag{2.1}$$

Doing a similar calculation as was done for the untrapped case, one can show that the critical temperature for condensation in a trap is not zero; instead it is given by [2],

$$T_{\text{crit}} = \sqrt{\frac{(\hbar\omega_x)\,(\hbar\omega_y)}{k_B^2} \frac{N}{\zeta(2) g_0}}, \tag{2.2}$$

which depends on the total number of particles in the trap, N, rather than the density. This arises from the fact that this system is finite; it is not necessary to take the limit where the number of particles goes to infinity, which is clearly unphysical for a finite system.

The non-existance of BEC in the untrapped case is related to a more general result, called the Hohenberg-Mermin-Wagner theorem (HMW), which shows that true long-range order cannot exist in infinite two-dimensional systems. In this case, the order parameter of the condensation phase transition is the ground state wave function, normalized to be proportional to the square-root of the population of the ground state. Fortunately, there are a number of caveats to this proof that are very significant for the search of BEC-like effects in 2D.

First, the absence of a true BEC does not necessarily forbid the presence of superfluidity. The general idea behind the HMW theorem is that thermal fluctuations exist at temperatures above absolute zero which kill the long-range order parameter; in a BEC system, these fluctuations take the form of vortices in the superfluid component, which are spontaneously generated, and which quench the superflow. However, in the early 1970's, theorists V.L.

[2] A more rigorous discussion of trapped condensates, including interactions, was performed by Baym and Pethick for cold atoms [66] and for exciton-polaritons (discussed in Section 1.1.4) by Berman, Lozovik, and Snoke [67].

Berezinskii [68], J.M. Kosterlitz, and D.J. Thouless [69] showed that something similar to long-range order can exist in many two-dimensional systems (of which, a neutral superfluid is one)[3]. Below some critical temperature, free vortices are energetically unfavorable; instead, vortices appear only in vortex-anti-vortex pairs. It was shown in both papers that this phase results in a non-zero superfluid density. The BKT transition has been experimentally observed in atomic systems - in these studies, some degree of coherence is observed above and below the critical temperature, while superfluidity seems to occur only below the critical temperature [70], and free vortices are thermally activated only above the critical temperature [71], as expected. There has been some evidence of power-law decay of coherence in polariton systems; although the exponent found in those measurements does not match what is predicted by the BKT model [72].

Secondly, in a finite system "macroscopic occupation of the ground state" can be a somewhat fuzzy concept. In a truly infinite system, which is assumed in the simple model above, the system possesses an infinite number of particles distributed amongst a true continuum of states. In this case, macroscopic occupation is a straightforward concept - normally each state would possess an infinitesmally small density of particles; any single state with a finite density associated with it can be described as macroscopically occupied. In a real, finite system - where the ground state will always have some finite population - one is typically looking for a sharp increase in the ground state population associated with a critical density or temperature.

In finite systems it is more pragmatic to think about long-range order in terms of coherence length. The HMW theorem proves only that infinite coherence length is impossible in a two-dimensional system. In practice, a finite but macroscopically large population can still exhibit a coherence length that is larger than the size of the system. By most definitions this scenario would be interpreted as the apperance of a condensate.

To summarize, there is some reason to believe that BEC is easier to observe in a trapped system, but it may be possible to observe some degree of spatial coherence or superfluidity without it. The more important role of a trapping potential is that it is necessary for

[3]In this type of system, the coherence does not fall off expontentially, as in the disordered case. Instead, it falls off more slowly, as a power law.

achieving a large, steady-state density of indirect excitons. It will be shown in Chapter 3 that indirect excitons in this system are strongly repulsive, so an untrapped population will tend to diffuse very quickly.

There are a number of trapping methods available in systems of spatially indirect excitons. Recall that the energy of an indirect exciton scales linearly with applied electric field in the growth direction,

$$\Delta E_{\text{exciton}} = -edF_z \tag{2.3}$$

where the dipole length, d, is 20 nm for the representative structure modeled in Figure 5[4]. In a spatially inhomogeneous electric field, indirect excitons will tend to be drawn to high electric field areas. This method of electrostatic trapping is one of the more common techniques used in the study of indirect excitons [73, 74, 75]. The IX radiative lifetime is exponentially dependent on the electric field, which can complicate the system. In principle, having the longest lifetime at trap center seems beneficial, as it may provide some evaporative cooling. On the other hand, a typical implementation of this type of trap involves sharp traps defined by pattern contacts on the sample surface. A sharp gradient in the transverse field, by Gauss's law, typically also induces a large in-plane field, which can result in ionization. In a study by Rapaport et. al, it was shown that the predicted effective lifetime drops rapidly with trap depth - going from a 3 meV deep trap lowers the lifetime around two orders of magnitude [75]. This drastically reduces the maximum possible density in the trap, due to a strong density dependent blue shift.

The method studied in this chapter and the next involves using a spatially inhomogeneous strain field to shift the band gap. This approach was used in studies of excitons and electron-hole liquids in bulk semiconductors [76, 77] and was first used in the coupled quantum well system by Negoita et. al [78]. This approach allows the applied electric field to be an entirely independent parameter, which can be used to tune the lifteime and the steady-state density of the indirect population.

There are a few complications implicit in strain-based trapping techniques, which will be

[4]For a typical coupled quantum well structure, this will be about equal to the well center-to-center distance.

discussed in more detail later in this chapter. Shear strain locally changes the symmetry of the crystal in the trap, leading to mixing between different spin states, which significantly complicates the single-particle picture. It will be shown that strain traps with depths of 10 to 20 meV are possible. The limiting factor for trap depth will typically be when the crystal is pushed outside of the elastic limit; i.e., when defects begin to form or the sample fractures. While strain-based techniques are more difficult to implement as compact devices, it provides some flexibility in tuning the subband structure of the system, allowing one to explore different aspects of the system.

2.2 ELASTIC THEORY - STRESS AND STRAIN

The goal of this section will be to set up the machinery necessary to calculate the energy of a given stressor geometry in a GaAs sample. A stress applied to the sample will result in some deformation, or strain, of the local crystal structure, which must first be calculated. The effect of this strain on the band structure will then be calculated using the Pikus-Bir model.

The equilibrium strain for a given geomtry is obtained by solving Newton's second law, written for an infinitesmal volume element in a continuous medium [79],

$$F_i + \frac{\partial \sigma_{xi}}{\partial x} + \frac{\partial \sigma_{yi}}{\partial y} + \frac{\partial \sigma_{zi}}{\partial z} = \rho \frac{\partial^2 u_i}{\partial t^2}, \quad i = x, y, z. \tag{2.4}$$

The vector $\vec{F}$ indicates the bulk force on a particular volume element, which will be zero in our system. The variable σ_{ij} is the stress tensor, indicating the stress components on a particular volume element (a sketch of the action of the stress tensor on an infinitesmal cube volume element is shown in Figure 9). The partial derviatives of the local stress are significant, because the deformation of a particular infinitesmal volume element will be determined by the gradient of the force across its faces. The displacement of the volume element from the equilibrium position is given by $\vec{u}$; for the static solution, the partial derivative of the displacement with respect to time will be equal to zero.

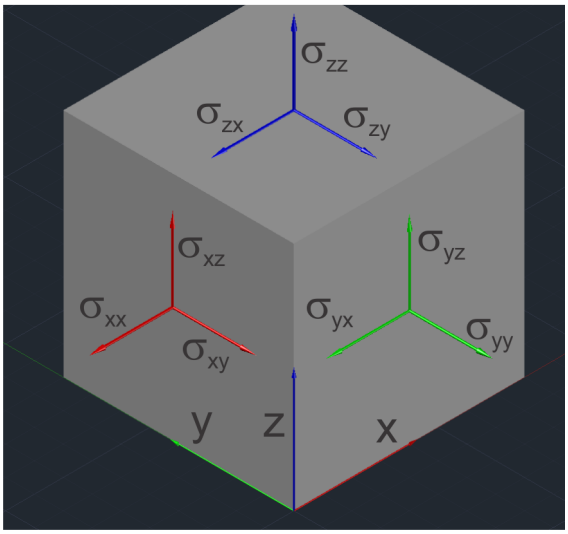

Figure 9: A sketch of the stress tensor components acting on an infinitesimal volume element.

Strain, ϵ_{ij}, is expressed in terms of the symmetrized derivatives of the displacement

$$\epsilon_{ij} = \frac{1}{2}\left(\frac{\partial u_i}{\partial x_j} + \frac{\partial u_j}{\partial x_i}\right) \tag{2.5}$$

and relationship between the strain and stress is given by the generalized Hooke's Law,

$$\sigma_{ij} = C_{ijkl}\epsilon_{kl} \tag{2.6}$$

where the stiffness tensor, C_{ijkl}, is a 3×3×3×3, fourth-order tensor. Due to symmetry, only six combinations from each coordinate pair (ij or kl) are distinct - *xx*, *yy*, *zz*, *yz*, *xz*, *xy* - so it is typically represented as a 6×6 matrix (where the aforementioned coordinate pairs are labeled as 1,2,3,...etc.). In particular, for GaAs the stiffness tensor is given by [48],

$$C = \begin{pmatrix} C_{11} & C_{12} & C_{12} & 0 & 0 & 0 \\ C_{12} & C_{11} & C_{12} & 0 & 0 & 0 \\ C_{12} & C_{12} & C_{11} & 0 & 0 & 0 \\ 0 & 0 & 0 & C_{44} & 0 & 0 \\ 0 & 0 & 0 & 0 & C_{44} & 0 \\ 0 & 0 & 0 & 0 & 0 & C_{44} \end{pmatrix}. \tag{2.7}$$

The values used for our simulations are based on the room temperature values and temperature derivatives given in Adachi's text [48]; therein, it is shown that the slope of the stiffness with respect to temperature is approximately constant down to T = 0. Specifically, the values used here are $C_{11} = 12.11 \times 10^4$ N/mm^2, $C_{12} = 5.48 \times 10^4$ N/mm^2, and $C_{44} = 6.04 \times 10^4$ N/mm^2. The difference between the stiffness of AlAs and GaAs is small; for $Al_{0.45}Ga_{0.55}As$, the difference from GaAs for each component is less than 3% [48]. Therefore, it is reasonable to approximate the entire structure as bulk GaAs for the purposes of the strain calculation. The boundary conditions will be determined by the stressor structure geometry, a rough diagram of which is shown in Figure 10.

There are a number of approaches to finding the static solution to (2.4). One method is to start with an intial guess at the strain field based on the trap shape and evolve it in time with an additional, small damping term, until the system reaches equilbrium. Another method is to use a variational approach to solve for the configuration that minimizes the potential energy of the system, subject to the given boundary conditions.

Ultimately, ANSYS, a commercial finite-element software, was used. The details of the ANSYS calculation are described in detail in Appendix C. Similar calculations were initially performed by Balili and Reid to model the same stressor geometry in the microcavity polariton system [80].

There are four boundary conditions that need to be taken into consideration in this solution: the edges, the top plate, the bottom plate, and the pin. It was found through trial-and-error that the boundary conditions at the edges of the sample are not critical in determining the shape of the trap, given that they are far enough away from trap center that the profile created by the pin has more or less relaxed to its equilibrium value. Likewise, the top plate boundary conditions are not very significant, as it does not put significant pressure on the sample (compared to that produced by the pin or the edges of the hole). Typically, the role of the top plate is simply to hold the sample in place.

There are a few ways that the bottom plate can be modeled. The most realistic approach is to fix the position of the bottom face of the sample in the z-direction; in other words, requiring that the displacement of volume elements in contact with the plate be equal to zero. This would allow for sliding in the x- and y-directions. Numerically, it is simpler to

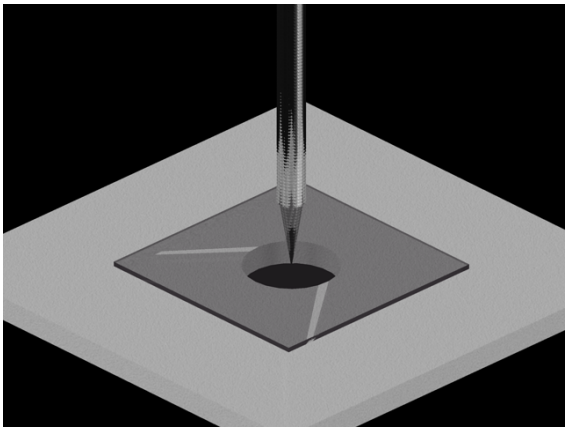

Figure 10: Rough schematic of the stressor geometry. The sample (shown as transparent here) is situated over a circular hole in a flat aluminum plate, typically of radius around 1 mm. A stainless steel pin is pushed by micrometer-driven springs (not shown) into the sample, ideally near the center of the hole. A top plate is typically used to hold the sample in place.

fix the bottom surface entirely (requiring that the pin is effectively stuck to the bottom of the plate). Experimenting with these two conditions revealed that there was no signficant difference in the trap shape between them, thus the entirely fixed bottom surface condition was used.

The pin contact surface is strongly dependent on its shape and surface roughness, so accurately modeling the pin geometry is not straightforward. The radius of the pin tip is roughly in the range of 25 μm to 50 μm. An analytic approach is to model the pin tip as a half-sphere in contact with a semi-infinite half-plane, which is a simple problem in Hertzian contact theory. In that approach, the contact radius of a stainless steel pin on the surface is given by [81],

$$a = \left[\frac{3}{4}F\left(\frac{1-\nu_{\text{GaAs}}^2}{E_{\text{GaAs}}} + \frac{1-\nu_{\text{Steel}}^2}{E_{\text{Steel}}}\right)R\right]^{1/3} \tag{2.8}$$

where $\vec{F}$ is the applied force, R is the radius of the pin tip, and E and ν are the elastic modulus and Poisson ratio, respectively, of the two materials. Using the material parameters

for GaAs [82] and stainless steel [83], a 25 μm, spherical pin tip would have a 7 μm contact radius at 1 N of applied force.

A number of approaches were made to modeling the contact surface of the pin. It is expected that the strain will be sharply discontinuous on the top surface of the sample directly underneath the pin. However, we are primarily interested in the strain in the plane of the quantum wells, which are typically a few hundred nanometers from the bottom of the sample. Far from the contact point the sharp spatial features associated with the pin are mostly washed out of the strain profile. It was observed that all pin models produce small discontinuities in the strain profile underneath the edges of the pin and are noticeable even near the bottom surface, something that is not observed in the experimental data. This can be eliminated either by locally smoothing the simulation results or taking a linear cross-section which avoids this region; in any case, the trap profile otherwise fits the experimental trap shape very well, as will be discussed in Section 2.3.1. One possible explanation for this is that the stress gradients at the edges of the pin on the top surface are extremely sharp; meaning that the sample is outside the elastic regime very close to the pin tip and that non-linear effects would need to be considered to model it correctly.

Ultimately, the most critical factors in determining the trap profile are the sample thickness, the hole radius, and the applied force. Using a typical geometry, the resulting strain profiles produced by ANSYS for a nominal 1 N force are shown in Figure 11. Excluding effects due to deformation of the pin and the plate, the strain profile will be linear with applied force. Therefore, any stress within the elastic limit can be modeled by simply scaling these results.

2.3 PIKUS-BIR HAMILTONIAN

Next, the dependence of the conduction and valence band energy on strain needs to be considered. This can be derived in a manner similar to the discussion of $k \cdot p$ theory in Chapter 1; the similarity comes from the idea that an applied strain changes the symmetry of the problem in a fashion analogous to non-zero k. The effect of strain on the conduction

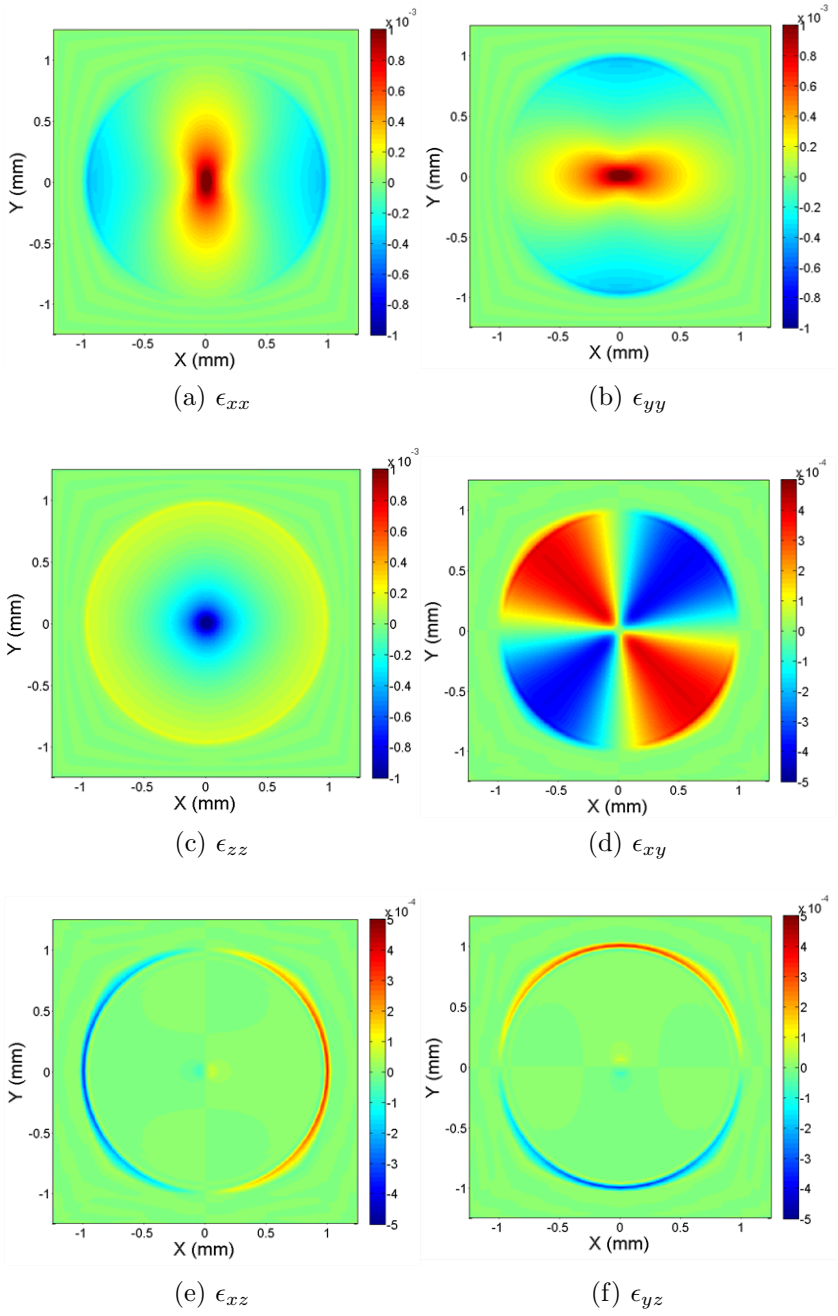

(a) ϵ_{xx} (b) ϵ_{yy}

(c) ϵ_{zz} (d) ϵ_{xy}

(e) ϵ_{xz} (f) ϵ_{yz}

Figure 11: The spatial strain profiles near the bottom surface of the sample, output by ANSYS for the stressor geometry shown in Figure 10, with a 25 μm radius pin, sitting on a 1 mm radius hole in an incompressible metal plate. Each profile is a 2D cross-section taken 500 nm from the bottom of a 100 μm thick sample. A nominal force of 1 N was applied uniformly to the area under the pin.

band to lowest order is simple, given that the s-like states of the electron are not split or mixed:

$$\Delta E_{\text{cond}} = -a_c \left(\epsilon_{xx} + \epsilon_{yy} + \epsilon_{zz}\right). \tag{2.9}$$

In GaAs, the conduction band deformation potential, a_c, is shown in Table 2. The effect of strain on the valence band is more complicated and is modeled by the Pikus-Bir Hamiltonian. The Pikus-Bir Hamiltonian can be written simply in the same basis as the Luttinger-Kohn Hamiltonian (see Equation (1.24)), with modified parameters [1]:

$$P_s = -a_v \left(\epsilon_{xx} + \epsilon_{yy} + \epsilon_{zz}\right), \tag{2.10}$$

$$Q_s = -\frac{b}{2}\left(\epsilon_{xx} + \epsilon_{yy} - 2\epsilon_{zz}\right), \tag{2.11}$$

$$R_s = \frac{\sqrt{3}b}{2}\left(\epsilon_{xx} - \epsilon_{yy}\right) - \mathrm{i}d\epsilon_{xy}, \tag{2.12}$$

$$S_s = -d\left(\epsilon_{xz} - \mathrm{i}\epsilon_{yz}\right). \tag{2.13}$$

The overall Hamiltonian can be found by summing the Pikus-Bir Hamiltonian and the Luttinger-Kohn Hamiltonian. Several approximations can be made to simplify the overall Hamiltonian. First, in the LK term, one can assume that k_z is a fixed value due to quantum well confinement and that $k_x = k_y = 0$. For the sake of calculating the ground state energy as a function of position, only the band-center energy is necessary. This is a reasonable approximation at low temperature, because the average kinetic energy due to in-place motion will be small compared to the confinement energy. The in-plane k-dependence of the energy will be explored in Chapter 3.

Due to the close proximity of our quantum wells to the bottom of the structure, one can also assume that the ϵ_{xz} and ϵ_{yz} components of the strain are approximately zero. This is verified by the numerical simulation; as shown in Figure 11, these components are non-zero near the edge of the hole, but are negligible near trap center, where the population of excitons largely resides.

The standard Hamiltonian can be transformed into a block-diagonal form, as demonstrated in Chuang [1], and can then be separated into two, de-coupled 2×2 matrices. Taking

Parameter	Value in GaAs (eV)	Value in AlAs (eV)
a_c	-7.17	-5.64
a_v	1.16	2.47
b	-1.7	-1.5
d	-4.55	-3.4

Table 2: Deformation Potentials [1] in GaAs and AlAs

the previous two assumptions into account, this reduced Hamiltonian is

$$H = \begin{bmatrix} P_s + Q_s - \frac{\Delta}{2} & |R_s| \\ |R_s| & P_s - Q_s + \frac{\Delta}{2} \end{bmatrix} \tag{2.14}$$

where P_s, Q_s and R_s are the strain terms given in (2.13). The Δ term is the hh-lh confinement splitting, at zero in-plane momentum,

$$\Delta = 4\frac{\hbar^2 k_z^2}{2m_0}\gamma_2 \tag{2.15}$$

where γ_2 is as given in Table 1. This Hamiltonian acts on the following basis functions:

$$|\text{hh}\rangle = \frac{1}{\sqrt{2}}e^{\text{i}\left(\frac{\theta_R}{2}+\frac{\pi}{4}\right)}\left|\frac{3}{2},\frac{3}{2}\right\rangle - \frac{1}{\sqrt{2}}e^{-\text{i}\left(\frac{\theta_R}{2}+\frac{\pi}{4}\right)}\left|\frac{3}{2},-\frac{3}{2}\right\rangle \tag{2.16}$$

$$|\text{lh}\rangle = -\frac{1}{\sqrt{2}}e^{\text{i}\left(\frac{\theta_R}{2}-\frac{\pi}{4}\right)}\left|\frac{3}{2},\frac{1}{2}\right\rangle + \frac{1}{\sqrt{2}}e^{-\text{i}\left(\frac{\theta_R}{2}-\frac{\pi}{4}\right)}\left|\frac{3}{2},-\frac{1}{2}\right\rangle. \tag{2.17}$$

Recall that the R_s term is complex and depends on the component of the shear strain that breaks the x-y symmetry of the crystal:

$$R_s = |R_s|e^{\text{i}\theta_R} = \frac{3}{2}b(\epsilon_{xx} - \epsilon_{yy}) - \text{i}d\epsilon_{xy} \tag{2.18}$$

The eigenvalues of this matrix can be found analytically, as follows:

$$\epsilon_{\pm} = P_s \pm \sqrt{\left(Q_s - \frac{\Delta}{2}\right)^2 + |R_s|^2} \tag{2.19}$$

In the next section, this model will be applied to an experimentally determined trapping profile.

2.3.1 Trap Potential Fit

To calibrate the trapping potential, it makes more sense to look at the DX luminescence than the IX. Direct excitons will typically be less sensitive to electric field and do not experience a significant density-dependent blue shift. But they should exhibit roughly the same strain dependence as indirect excitons.

The energy of a typical strain trap can be found by pumping the system with a broadly defocused, CW laser at a significantly higher energy than the direct line. This generates hot carriers, which cool down and either recombine as direct excitons or turn into indirect excitons via tunneling, then recombine. By observing the spectrally-resolved photoluminescence along a spatial cross-section, the energy of the direct line as a function of position can be found - this was done for a 14 nm sample at low stress, as shown in Figure 12.

In the same figure, the position-dependent peak energy values were extracted and fit to the model described above using an overall energy shift, an overall position shift, the applied force, and the effective k_z as fitting parameters. While, in principle, the energy shift is not explicitly a free parameter within the model (it should be accounted for by the band gap energy, confinement energy, and strain) - the precision of the model parameters are such that a small error in the overall energy, which is around 1.5 eV, will be very large with respect to the energy variation of the trap - which is on the order of 10 meV. Likewise, the position shift is simply for convenience, to take into account the fact that the trap is not exactly centered. The center of the position axis could be defined such that the center of the trap is at zero, but there would still be some uncertainty due to the slight asymmetry of the trap profile.

The ANSYS-generated strain profile is calculated at nominally 1 N of applied force. It is

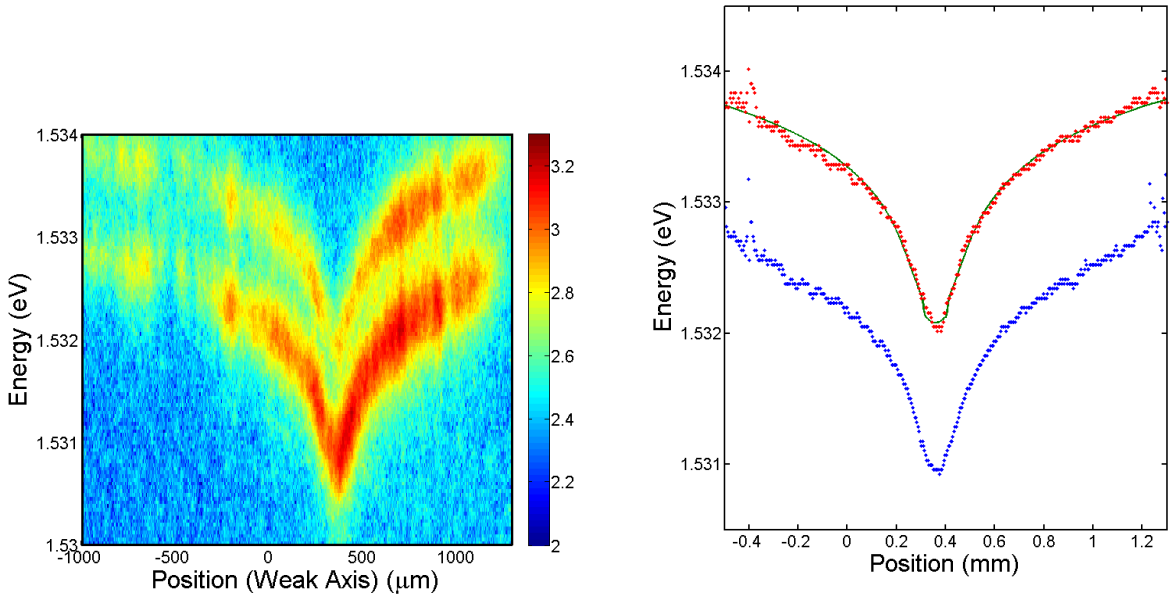

Figure 12: A plot of the photoluminescence from the direct and biexciton line for a pair of 14 nm coupled quantum wells at low stress. On the left, the spectrally resolved log-intensity (color scale), on the right, the extracted peak centers as a function of position.

somewhat difficult to calibrate this to the actual force applied in the experimental setup; the force on the pin is determined by a micrometer driven stressor at the top of the sample rod compressing a spring. In principle, the force is simply defined by the spring constant and the amount of compression. In practice, the variation of the spring constant and effective spring constant of the rod with temperature makes it difficult to calibrate it directly. Instead, it makes more sense to use the overall trap depth - which is easily observed in the luminescence - as a measurement of the applied force, which determines all other stress effects within the model.

To improve ease of calculation, the confinement energy is approximated using the infinite-barrier model; the effective value of k_z is not fixed at π/a, but is instead allowed to vary as a fitting parameter. Of course, using this approach, one should pay attention to the value predicted by the fit - it should be slightly smaller than the infinite-barrier case, but not drastically different (the fit shown corresponds to an effective well width of 14.14 nm, only slightly larger than the infinite barrier approximation).

It can be seen from Figure 12 that this model provides a reasonable fit to the potential associated with the direct exciton luminescence. There are two primary differences between the indirect exciton and the direct exciton energy profile. First, the indirect exciton will exhibit a density-dependent blue shift. Second, the electric dipole moment of an indirect exciton is much larger - due to spatial charge seperation - so it is shifted much more by an electric field. A discussion of the indirect exciton fit at low density is discussed in the following section.

2.3.2 Piezoelectric Effect

The piezoelectric effect refers to the appearance of an electric field in a crystal under stress. It is caused by charge separation due to the deformation of the crystal lattice. In GaAs, the induced polarization in the z-direction, P_z, in GaAs and AlAs due to the piezoelectric effect [48] is given by,

$$P_z = e_{14}\epsilon_{xy}. \tag{2.20}$$

where e_{14} is a constant determined by the material. In the *p-i-n* doped samples, the top and bottom layers of the sample can be assumed to be conductive. Therefore, the potential is mostly constant across the top and bottom faces and there will be charge buildup in the structure to cancel out the overall effect of any piezoelectric-induced field. The only additional field felt by the indirect excitons will be due to the imbalance of induced charge in the GaAs and $Al_{0.45}Ga_{0.55}As$ layers, as discussed below.

Solving for the field in each well, there will be two constraints. First, that the total voltage drop across the sample at any point is fixed (given by the applied voltage plus the built-in voltage). Second, the z-component of the electric flux density must be constant at each interface - as required by Gauss' Law. The transverse component of the electric field is assumed to be negligible [5]. Setting up these equations and solving them for the electric field, F, in the GaAs and $Al_{0.45}Ga_{0.55}As$ regions gives[6],

$$F_W = \frac{\epsilon_B}{L_W\epsilon_B + L_B\epsilon_W} V_{\text{Total}} + \frac{L_B}{L_W\epsilon_B + L_B\epsilon_W}\left(P_B - P_W\right) \tag{2.21}$$

$$F_B = \frac{\epsilon_W}{L_B\epsilon_W + L_W\epsilon_B} V_{\text{Total}} + \frac{L_W}{L_B\epsilon_W + L_W\epsilon_B}\left(P_W - P_B\right) \tag{2.22}$$

and the difference in the polarization is given by the difference in the piezoelectric constant values for GaAs and $Al_{0.45}Ga_{0.65}As$:

$$P_B - P_W = (\epsilon_{14}^B - \epsilon_{14}^W)\epsilon_{\text{xy}}. \tag{2.23}$$

In the above expression, the lengths, L_W and L_B, are the total thicknesses of GaAs and $Al_{0.45}Ga_{0.55}As$ in the structure, respectively. In the 2D profile of the indirect exciton luminescence, it is observed that the trap profile is wider along one crystal direction and narrower in the other. This asymmetry is not observed in the direct luminesence. One possible explanation is that the indirect exciton - due to its large electric dipole moment - is shifted

[5] The voltage drop across the z-direction occurs over a 500 nm length scale, whereas any variation in the potential due to polarization charge occurs over length scales associated with the strain, typically tens to hundreds of microns.

[6] From here, 'W' will be used to indicate the GaAs regions - which is the material associated with the wells - and 'B' will be used to indicate the $Al_{0.45}Ga_{0.55}As$ regions - which is associated with the barriers

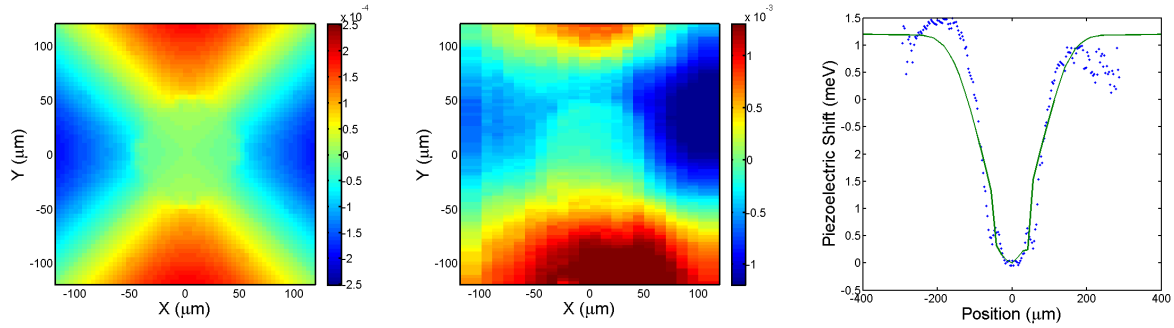

Figure 13: Comparison between (a) ϵ_{xy} term from ANSYS calculations (b) and measured deviation between DX and IX lines. (c) Model fit (green line) to measured spatial energy deviation between direct line and indirect line (blue data points). Fit is given by $\alpha\epsilon_{xy} + \beta$, where fitting parameter α gives the proportionality factor described in the text and β is an overall energy shift.

significantly in the presence of an induced piezoelectric field. Recall that the ϵ_{xy} component of the strain has a four-lobed structure, so it would make sense that the field would oppose the overall electric field along one one crystal axis ([110] or [1$\bar{1}$0]) and enhance it along the other.

To get an estimate of this shift, one can take a 2D profile of the indirect and direct luminesence lines at relatively low density. The energy difference, $\Delta E_{\text{IX-DX}}$, between the two lines is,

$$\Delta E_{\text{IX-DX}} = -(\mu_{\text{IX}} - \mu_{\text{DX}})F_W \tag{2.24}$$

where the μ values are the dipole moments for the indirect and direct excitons. This analysis was done on a low-stress trap in a sample with 14 nm wells with a 4 nm barrier. The expected dipole length for the heavy holes in this structure should be around 22 nm (see Figure 5). In Figure 13, this measured energy difference is shown next to a representative image of the ϵ_{xy} component of the strain showing that they have the same symmetry.

The proportionality constant between ϵ_{xy} and the energy deviation can be calculated

entirely from geometric and material parameters,

$$\left[\frac{\Delta E_{\text{IX-DX}}}{\epsilon_{xy}}\right]_{V_{\text{Total}}=0} = -e(\mu_{\text{IX}} - \mu_{\text{DX}})(e_{14}^{B} - e_{14}^{W})\frac{L_B}{L_W\epsilon_B + L_B\epsilon_W}. \tag{2.25}$$

Using parameters from Adachi [48], this overall proportionality factor should be around 4.7 eV. The measured proportionality constant based on fitting the shear strain calculated from ANSYS to the measured $\Delta E_{\text{IX-DX}}$ was found to be 2.4 eV (using the proportionality constant and an overall energy shift - due to the overall applied bias - as fitting parameters).

It is worth noting that this result is dependent on the relatively small difference in the piezoelectric constant in the GaAs wells and the $Al_{0.45}Ga_{0.55}As$ barrier - respectively -0.16 C/m^2 and -0.19 C/m^2 at room temperature [48]. Not only is the limited precision a possible source of discrepancy, the measurement was performed at low temperature. There do not seem to be any temperature dependent measurements of the piezoelectric constant available for the $Al_xGa_{1-x}As$ system in the literature. A relatively small variation in the difference between the two parameters at low temperature could explain the factor of two difference in the results.

A more in-depth analysis of this nature could be a useful method for measuring the piezoelectric constant in this type of system. For it to be useful, a more careful calibration of the direct- and indirect-dipole moments would need to be performed. This could be done, for example, by carefully measuring the Stark shift of both lines for small pertubations around this applied bias.

2.3.3 Oblong Trapping Potential

It is interesting to note that the characteristics of the trap are partially determined by the symmetry of the trapping geometry. One simple way to modify this geometry is to break the circular symmetry of the geometry discussed above. For the coupled-quantum well system, this asymmetry is already built-in due to the piezoelectric effect described above. But it may also be of interest to generate an asymmetric trap for direct excitons. For example, one might expect that by using a trap geometry that is stretched along one direction, it is also possible to make a trap with similar symmetry.

ANSYS was used to calculate the strain resulting from a circular pin pushing into a sample mounted on a rectangular hole in a fixed plate. The main results are shown in Figure 14. Recall that the trapping profile is primarily determined by the energy shift of the conduction band given in 2.9; this is proportional to the hydrostatic component of the strain: $\epsilon_{xx}+\epsilon_{yy}+\epsilon_{zz}$. From the shape of the hydrostatic strain, it is evident that the trapping potential in this configuration would be slightly asymmetric, as expected.

Another feature of this geometry is the enhancement of the shear strain term, ϵ_{yz}. Note that in Figure 11, the terms ϵ_{yz} and ϵ_{xz} are only significant near the edges and - even there - have a maximum value of less than half the central value of ϵ_{xx}, ϵ_{yy} and ϵ_{zz}. For the rectangular case, ϵ_{yz} is approximately the same value as these terms. Similar calculations show that this is further enhanced if the pin is off-center along the y-axis - for an applied stress at $y = +125\mu$m, the ratio of $\max(\epsilon_{yz})$ to $\max(\epsilon_{xx}+\epsilon_{yy}+\epsilon_{zz})$ is around 1.29, compared to the circular hole and the centered-pin case for the rectangular hole - where the same ratio is around 0.30 and 1.06, respectively.

One can see from the Pikus-Bir Hamiltonian that the primary role of the ϵ_{xz} and ϵ_{yz} terms is to mix the $\mathrm{m}_j = \pm\ 3/2$ valence band state with the $\mathrm{m}_j = \pm\ 1/2$ state. In the exciton picture, this term mixes the hh exciton state with the lh exciton state with opposite spin orientation. Selection rules will be discussed in more detail in Section 2.6, but essentially these strain components mix bright heavy-hole exciton states with dark light-hole exciton states, and dark heavy-hole exciton states with bright light-hole exciton states. Design of a stressor geometry which maximizes these shear components could be one way to study a persistent population of dark excitons - by making them partially bright - or for studying two-photon processes - which are allowed for $\Delta\ell = 2$ transitions, but suppressed for $\Delta\ell = 1$ transitions.

A similar trapping geometry was experimentally studied by Bryan Nelsen [84]; in this study, it was found that samples stressed in this geometry are strongly inclined to fracture. It seems likely that the strain terms discussed here - ϵ_{xz} and ϵ_{yz} - are responsible for this tendency. From the perspective of the stress tensor, one can picture σ_{xz} as a force shearing an x-oriented crystal face in the z-direction - basically the same motion one would use in cleaving a sample.

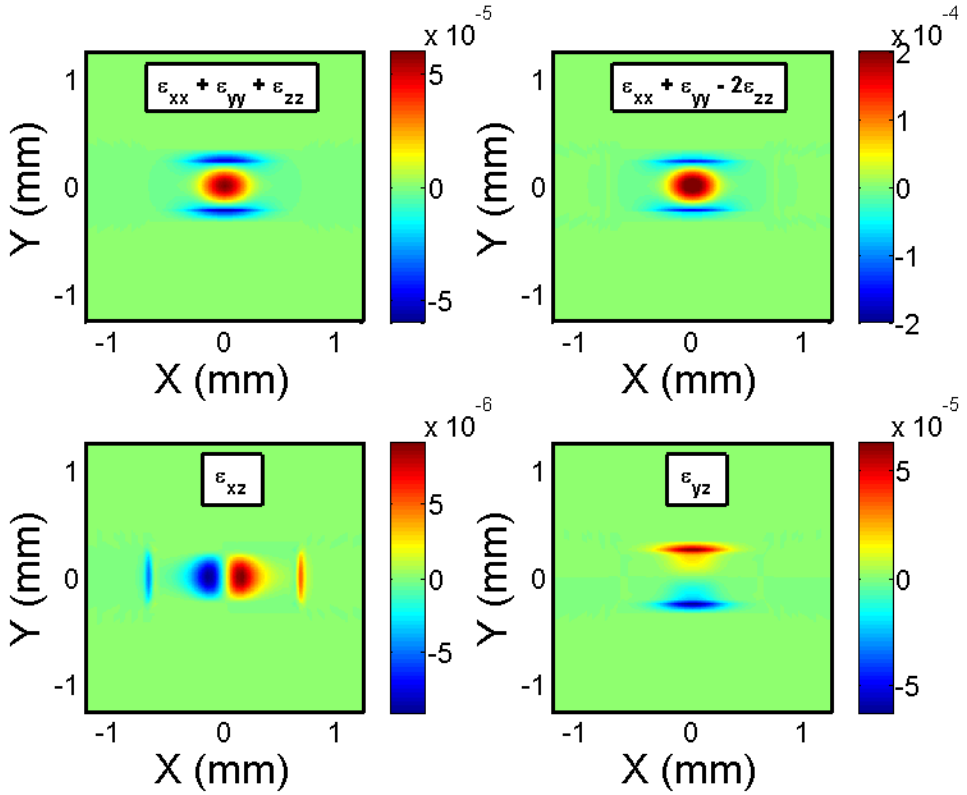

Figure 14: ANSYS results near the bottom surface of a 250 μm thick GaAs sample, stressed with a 25 μm pin, on top of a 1.25 mm $\times$ 0.50 mm hole in a fixed plate. Applied force is nominally 1 N (not calibrated to any experimental stressor force). The plots shown are a cross-section of the strain in the plane 2.5 μm from the bottom of the sample.

2.4 INTERSUBBAND MIXING

The primary focus of Section 2.3 was on calculating the spatial dependence of the ground state energy as a function of applied stress. No explicit mention was made about the eigenvectors or the character of the ground state. In the presence of shear strain, there will also be some degree of mixing between the heavy hole and light hole valence bands.

The normalized eigenvectors associated with eigenvalues in (2.19) can be expressed in the hh-lh basis,

$$\psi_{\pm} = g_{hh}(z)\eta_{hh}^{\pm}\left|hh\right\rangle + g_{lh}(z)\eta_{lh}^{\pm}\left|lh\right\rangle \tag{2.26}$$

where the analytical expressions for the eigenvector components are as follows:

$$\eta_{hh}^{\pm} = \frac{1}{\sqrt{2}}\frac{|R_s|}{\left[\left(Q_s-\frac{\Delta}{2}\right)^2+|R_s|^2 \mp \left(Q_s-\frac{\Delta}{2}\right)\sqrt{\left(Q_s-\frac{\Delta}{2}\right)^2+|R_s|^2}\right]^{1/2}} \tag{2.27}$$

$$\eta_{lh}^{\pm} = \frac{1}{\sqrt{2}}\frac{\left(Q_s-\frac{\Delta}{2}\right) \mp \sqrt{\left(Q_s-\frac{\Delta}{2}\right)^2+|R_s|^2}}{\left[\left(Q_s-\frac{\Delta}{2}\right)^2+|R_s|^2 \mp \left(Q_s-\frac{\Delta}{2}\right)\sqrt{\left(Q_s-\frac{\Delta}{2}\right)^2+|R_s|^2}\right]^{1/2}}. \tag{2.28}$$

The functions *g(z)* correspond to the envelope wave functions associated with the heavy-hole and light-hole state in the quantum well; it is assumed that, for in-plane motion, $\vec{k}_{||} \approx 0$. While complicated, there are a few important features to these terms. Provided $Q_s < \frac{\Delta}{2}$, which corresponds to the low-stress regime where the heavy-hole state is the ground state, the magnitude of η_{hh}^{-} (the minus term corresponding to the lower energy eigenvalue), goes to unity as expected in the limit of zero coupling, $|R_s| \to 0$. The heavy-hole amplitude is negative for both roots, the light-hole amplitude is negative for the higher-energy eigenvalue and positive for the lower-energy eigenvalue. This will play an important role in determining the polarization direction of the ground state, to be discussed in Section 2.6.

At trap-center, the shear strain is expected to be zero, by symmetry. In that case, the ground state is expected to be the heavy-hole state until the crossover point, where $Q_s = \frac{\Delta}{2}$. A plot of the heavy-hole and light-hole energies (for $\vec{k}_{||} = 0$) at the center of the trap is shown

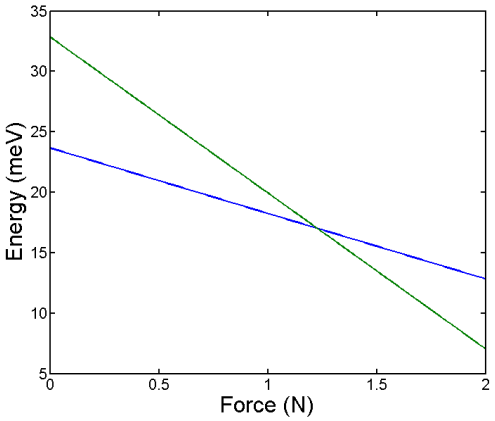

Figure 15: Using ANSYS results shown previously, a plot of the heavy-hole (blue) and light-hole (green) exciton energy at trap center, as a function of applied force.

for 14 nm quantum wells as a function of the nominal applied force. At high strain, the light-hole exciton is expected to become the ground state at trap center. This is something that is observed in the high-stress photoluminescence, as will be discussed in Chapter 3. At the edges of the trap, the presencence of shear strain at low stress results in a ground state which is primarily heavy hole, with a small light hole component.

2.5 ELECTRON-HOLE EXCHANGE

From the perspective of the Luttinger-Kohn and Pikus-Bir Hamiltonians, the dark and bright exciton states are degenerate near-zero in-plane k, and are not split by the non-zero strain terms caused by our trap.

The largest term expected to break their degeneracy - at least for direct excitons - is electron-hole exchange. Physically, electron-hole exchange can be thought of as a virtual photon-emission and recombination, coupling bright states with the same angular momentum. For example, an exciton composed of a spin-down electron and a $+\frac{3}{2}$ heavy hole can re-combine, emit a virtual photon of angular momentum +1, which can immediately create

an exciton composed of a spin-up electron and a $\frac{1}{2}$ hole. With a non-zero hh - lh splitting, this transition is suppressed by energy conservation, but the coupling will still be there, and create a small splitting.

For the transition between two exciton states, the relevant matrix elements for short-range exchange is given by [85],

$$H_{12} = -\langle\psi_{e,2}|\langle\psi_{h,2}|\left(a_x S_{h,x}S_{e,x} + a_y S_{h,y}S_{e,y} + a_z S_{h,z}S_{e,z}\right)|\psi_{e,1}\rangle|\psi_{h,1}\rangle \tag{2.29}$$

where typical exchange parameters for excitons in 7 nm GaAs quantum wells were measured by Balili, et. al to be $a_x = a_y = 1.14$ meV and $a_z = 0.84$ meV [80]; the spin-structure of this Hamiltonian can be seen in the same reference.

Recall that from Fermi's golden rule, the transition rate between two states depends on the Hamiltonian matrix element of their coupling term as follows:

$$r(i \to f) \propto |\langle f|H|i\rangle|^2 \tag{2.30}$$

Writing the rate and the energy matrix element between two exciton states in the same electron and hole quantum well subbands in terms of the envelope functions, defined in Section 1.3, one can see

$$\langle f|H|i\rangle \propto \left(\int g_e^*(z)g_h(z)\mathrm{d}z\right)\left(\int g_h^*(z)g_e(z)\mathrm{d}z\right) \tag{2.31}$$

and

$$r(i \to f) \propto \left|\int g_e^*(z)g_h(z)\mathrm{d}z\right|^4. \tag{2.32}$$

Recall that the overlap integral in the confinement direction is strongly suppressed due to the localization of the electron and hole for spatially indirect excitons. For a typical indirect lifetime of 1 μs, the transition rate associated with recombination is roughly three orders of magnitude less than for the direct case, as shown in the calculation by M. Szymanska in Figure 6. By the same logic, one can approximate that both the exchange splitting and the transition rates associated with electron-hole exchange will be - respectively - three and six orders of magnitude smaller than for the direct case. In the polariton system - based on

direct excitons in coupled quantum wells - the cited values of the coupling parameters were roughly on the order of 1 meV; for spatially indirect excitons, it can be approximated that the splitting associated with exchange will be on the order of 1 μeV or less. As this is far below the typical indirect exciton linewidth, effects due to exchange can likely be neglected.

2.6 LUMINESCENCE

In this section, the polarization-dependence of the exciton luminescence will be carefully derived. Pieces of this derivation can be found in Chuang [1] and Snoke [51], but this derivation will be careful to allow for complex polarization vector bases, which are associated with elliptical polarization.

In order to calculate the transition rate via recombination, we need the Hamiltonian for electron-photon interactions. This is usually approximated as,

$$H_{e-ph} = -\frac{e}{m}\vec{A}\cdot\vec{p} \tag{2.33}$$

where vector $\vec{A}$ represents the vector potential of the photon field and $\vec{p}$ represents the momentum of the electron. For a plane-wave basis, the vector potential can be written as:

$$\vec{A}(\vec{r},t) = \hat{\epsilon}\frac{A_0}{2}e^{i(\vec{k}\cdot\vec{r}-\omega t)} + \hat{\epsilon}^*\frac{A_0}{2}e^{-i(\vec{k}\cdot\vec{r}-\omega t)} \tag{2.34}$$

Dropping the time-dependence, gives the following expression for the Hamiltonian:

$$H_{e-ph}(\vec{r}) = -\frac{e}{m}\left(\hat{\epsilon}\cdot\vec{p}\right)\frac{A_0}{2}e^{i\vec{k}\cdot\vec{r}} - \frac{e}{m}\left(\hat{\epsilon}^*\cdot\vec{p}\right)\frac{A_0}{2}e^{-i\vec{k}\cdot\vec{r}} \tag{2.35}$$

Consider the transition rate from an initial state where there is an electron in the conduction band and zero photons, to a final state where there is an electron in the valence band and one photon; to calculate this, it is convenient to quantize the this Hamiltonian:

$$H_{e-ph}(\vec{r}) = -\frac{e}{m}\sum_{\vec{k},\lambda}\left[\sqrt{\frac{\hbar}{2\omega V}}\left(\hat{\epsilon}_\lambda\cdot\vec{p}\right)a_{\vec{k},\lambda}e^{i\vec{k}\cdot\vec{r}} + \sqrt{\frac{\hbar}{2\omega V}}\left(\hat{\epsilon}^*_\lambda\cdot\vec{p}\right)a^\dagger_{\vec{k},\lambda}e^{-i\vec{k}\cdot\vec{r}}\right] \tag{2.36}$$

In the notation of second-quantization, $a^\dagger_{\vec{k},\lambda}$ is an operator that creates a photon of wave

vector $\vec{k}$ and polarization state λ. The adjoint of this operator destroys a photon in that state. The sum over a λ indicates the sum over some complete basis of polarization vectors - for a given photon propagation direction, this will be a sum over two states. For the valence band eigenstates we use in the strain calculations, it is convenient to use right- and left-hand circular polarization states as the basis,

$$\hat{\epsilon}_{RHC} = \frac{1}{\sqrt{2}}(\hat{x} - \mathrm{i}\hat{y}) \tag{2.37}$$

$$\hat{\epsilon}_{LHC} = \frac{1}{\sqrt{2}}(\hat{x} + \mathrm{i}\hat{y}) \tag{2.38}$$

with the assumption that propagation is in the z-direction. This is appropriate when luminescnece is observed primarily normal to the surface of the sample. The entire second-quantized Hamiltonian is given by,

$$H_{e-ph} = \int d^3\vec{r}\Psi^\dagger(\vec{r})H(\vec{r})\Psi(\vec{r}) \tag{2.39}$$

where the Ψ operators are associated with the electron field. These can be expanded, assuming the electron is in the ground state of both the conduction band and valence band (in the lowest quantum well subbands and near $\vec{k} = 0$ in-plane). It can also be assumed for simplicity that the photon momentum is small compared to the electron momentum.

Photoluminescence arises from the transition of an electron from the conduction to the valence band through the emission of photon. The intensity of the PL is proportional the probability rate of the transition, the probability of a particular conduction band state being occupied, and the probability of a particular valence band state being vacant, as follows:

$$I = r(i \to f)f(E_i)(1 - f(E_f)) \tag{2.40}$$

The transition rate can be found from Fermi's golden rule:

$$r(i \to f) \propto |\langle i|\, \hat{\epsilon}_\lambda \cdot \vec{p}\, |f\rangle|^2 \tag{2.41}$$

Here $\hat{\epsilon}_\lambda$ refers to the electric field unit vector corresponding to a particular polarization state, denoted by λ, of the outgoing photon. To derive selection rules, one can decompose the valence band states into the tensor product of spherical harmonics and spin states. After

re-arranging the expression for the Hamiltonian given above, one arrives at the following matrix element for the recombination transition,

$$\langle f|\, H\, |i\rangle = -\frac{e}{m}\sqrt{\frac{\hbar}{2\omega V\epsilon}}\hat{\epsilon}^*_\lambda \cdot \langle v|\, \vec{p}\, |c\rangle\, I_{\rm vc} \tag{2.42}$$

where I_{vc} is the overlap integral between the conduction and valence band envelope wave functions in the z-direction:

$$I_{vc} = \int g^*_e(z) g_h(z) \mathrm{d}z \tag{2.43}$$

Note that the polarization vector does not act directly on the electron Hilbert space, so it can be factored out of the momentum matrix element. The momentum matrix elements are easily calculated for the relevant spherical harmonics [1]:

$$\langle S|\, p_x\, |X\rangle = \langle S|\, p_y\, |Y\rangle = \langle S|\, p_z\, |Z\rangle = \frac{im_0}{\hbar}P \tag{2.44}$$

The value P is referred to as the Kane's parameter. All other momentum matrix elements will be zero. These can be applied to the heavy- and light-hole valence band states:

$$\hat{\epsilon}^*_{RHC} \cdot \left\langle \frac{3}{2}, \frac{3}{2}\right| \vec{p}\, |iS\uparrow\rangle = \frac{m_0 P}{\hbar}, \tag{2.45}$$

$$\hat{\epsilon}^*_{LHC} \cdot \left\langle \frac{3}{2}, -\frac{3}{2}\right| \vec{p}\, |iS\downarrow\rangle = -\frac{m_0 P}{\hbar}, \tag{2.46}$$

$$\hat{\epsilon}^*_{RHC} \cdot \left\langle \frac{3}{2}, \frac{1}{2}\right| \vec{p}\, |iS\downarrow\rangle = \frac{1}{\sqrt{3}}\frac{m_0 P}{\hbar}, \tag{2.47}$$

$$\hat{\epsilon}^*_{LHC} \cdot \left\langle \frac{3}{2}, -\frac{1}{2}\right| \vec{p}\, |iS\uparrow\rangle = -\frac{1}{\sqrt{3}}\frac{m_0 P}{\hbar}. \tag{2.48}$$

All other transitions are forbidden, due to the fact that the underlying spin states of the electron do not line up, and their matrix elements are equal to zero for entirely in-plane polarization. A more general way of writing this, which will be useful in the following

section, is as follows:

$$\left\langle \frac{3}{2},\frac{3}{2}\right| \vec{p}\,|iS\uparrow\rangle = \frac{m_0 P}{\sqrt{2}\hbar}\left(\hat{x}-\mathrm{i}\hat{y}\right), \tag{2.49}$$

$$\left\langle \frac{3}{2},-\frac{3}{2}\right| \vec{p}\,|iS\downarrow\rangle = -\frac{m_0 P}{\sqrt{2}\hbar}\left(\hat{x}+\mathrm{i}\hat{y}\right), \tag{2.50}$$

$$\left\langle \frac{3}{2},\frac{1}{2}\right| \vec{p}\,|iS\downarrow\rangle = \frac{1}{\sqrt{6}}\frac{m_0 P}{\hbar}\left(\hat{x}-\mathrm{i}\hat{y}\right), \tag{2.51}$$

$$\left\langle \frac{3}{2},-\frac{1}{2}\right| \vec{p}\,|iS\uparrow\rangle = -\frac{1}{\sqrt{6}}\frac{m_0 P}{\hbar}\left(\hat{x}+\mathrm{i}\hat{y}\right). \tag{2.52}$$

The selection rules for recombination and absorption are relatively simple. Photons carry angular momentum $\ell = \pm 1$, so all transitions involving absorption or emission of photons must be characterized by $\Delta\ell = \pm 1$. The electron-photon coupling does not operate on spin, so $\Delta s = 0$. All of the valence band states listed here have orbital angular momentum of 1; so the only forbidden transitions are the ones where the spin quantum number is different. Recall that the light-hole states are composed of both spin-up and spin-down components, so light-hole excitons can always emit photons off of the normal axis.

Next, the polarization of emission from the ground state for spatially-indirect excitons is considered. In essence, the problem to be solved is to calculate the angular dependence of intensity measured through a linear polarizer at some angle, θ. For an arbitrary angle, the polarization angle can be defined in a linear basis as:

$$\hat{\epsilon}(\theta) = cos\left(\theta\right)\hat{x} + sin\left(\theta\right)\hat{y} \tag{2.53}$$

One major feature of a strain-based trap is that it alters the symmetry of the crystal. In the previous chapter it was shown that the heavy-hole and light-hole states are the eigenstates of the Luttinger-Kohn Hamiltonian when the in-plane k is equal to zero. By distorting the symmetry of the crystal, new eigenstates are also changed, according to the expressions in (2.26), (2.27), and (2.28).

Using the new eigenstates with the matrix elements calculated in Section 2.6, the follow-

ing matrix elements are found:

$$\langle\psi_{C\uparrow}|\,\epsilon(\hat{\theta})\cdot\vec{p}\,|hh\rangle \quad = -I_{hh}e^{\mathrm{i}\left(\frac{\theta_R}{2}+\frac{\pi}{4}\right)}\frac{P}{\sqrt{2}}e^{\mathrm{i}\theta} \tag{2.54}$$

$$\langle\psi_{C\downarrow}|\,\epsilon(\hat{\theta})\cdot\vec{p}\,|hh\rangle \quad = -I_{hh}e^{-\mathrm{i}\left(\frac{\theta_R}{2}+\frac{\pi}{4}\right)}\frac{P}{\sqrt{2}}e^{-\mathrm{i}\theta} \tag{2.55}$$

$$\langle\psi_{C\uparrow}|\,\epsilon(\hat{\theta})\cdot\vec{p}\,|lh\rangle \quad = I_{lh}e^{-\mathrm{i}\left(\frac{\theta_R}{2}-\frac{\pi}{4}\right)}\frac{P}{\sqrt{6}}e^{-\mathrm{i}\theta} \tag{2.56}$$

$$\langle\psi_{C\downarrow}|\,\epsilon(\hat{\theta})\cdot\vec{p}\,|lh\rangle \quad = I_{lh}e^{\mathrm{i}\left(\frac{\theta_R}{2}-\frac{\pi}{4}\right)}\frac{P}{\sqrt{6}}e^{\mathrm{i}\theta} \tag{2.57}$$

The terms I_{hh} and I_{lh} represent the overlap integrals between the envelope function of the valence and conduction band states.

Ultimately, we want an expression for the radiative rate of the ground state as a function of projection onto a linear polarization angle θ. This is found by combining the results from 2.26 with the expressions above:

$$|\,\langle\psi_{C\uparrow}|\,\hat{\epsilon}(\theta)\cdot\vec{p}\,|\psi_{\mathrm{gs}}\rangle\,|^2 = |I_{\mathrm{gs}}|^2||\eta^-_{\mathrm{hh}}|^2\frac{P^2}{4} + |I_{\mathrm{lh}}|^2||\eta^-_{\mathrm{lh}}|^2\frac{P^2}{12} + |\eta^-_{\mathrm{hh}}||\eta^-_{lh}||I_{\mathrm{hh}}||I_{\mathrm{lh}}|\frac{P^2}{2\sqrt{3}}cos(2\theta+\theta_R) \tag{2.58}$$

A convenient expression for the degree of polarization can be obtained from (2.58); the degree of polarization is defined in terms of the intensity at the angle of strongest transmission through a linear polarizer (I_{Max}) and the intensity at the angle of weakest transmission through a linear polarizer (I_{Min}):

$$D.O.P = \frac{I_{\mathrm{Max}}-I_{\mathrm{Min}}}{I_{\mathrm{Max}}+I_{\mathrm{Min}}} = 2\sqrt{3}\frac{|\eta_{\mathrm{hh}}||\eta_L|I_{\mathrm{hh}}I_{\mathrm{lh}}}{\eta^2_{\mathrm{lh}}I^2_{\mathrm{lh}}+3\eta^2_{\mathrm{hh}}I^2_{\mathrm{hh}}} \tag{2.59}$$

The predicted linear polarization component is defined entirely by the complex phase of the R-term in the Pikus-Bir Hamiltonian; from (2.59), one can see that the polarization is mostly strongly oriented at an angle of $\theta = -\theta_R$. In terms of the shear strain terms and the deformation potentials:

$$\tan(\theta) = -\frac{1}{2}\arg\left[\frac{\sqrt{3}}{2}b\left(\epsilon_{xx}-\epsilon_{yy}\right)-\mathrm{i}d\epsilon_{xy}\right] \tag{2.60}$$

The shear strain components all scale linearly with applied force, meaning that the polarization direction is independent of the magnitude of the force; it is determined entirely by the stressor geometry.

Also note that if the ground state were entirely heavy hole ($\eta_L = 0$) or entirely light hole ($\eta_H = 0$), the emission rate would be independent of polarization angle. These transitions correspond to circularly polarized light. The effect of shear strain is to mix the heavy-hole state that would emit right-handed circular polarization with the light-hole state that would emit left-handed circular polarization. A superposition of two circularly polarized states results in some degree of linear polarization.

A similar calculation can be done for the other three heavy-hole states. Surprisingly, the angular dependence of the polarization distribution is the same for the two bright heavy-hole states. One might expect that the linear polarized components of the two states should be orthogonal. In fact, they are orthogonal - one state is primarily right-circularly polarized with a small amount of left-circular polarization mixed in, the other is primarily is left-circularly polarized. The phase difference between the two components is such that the linear component of each state is in the same direction for both states.

Based on the plot shown in Figure 6, the overall oscillator strength of the indirect lh exciton is predicted to be approximately ten times that of the indirect hh exciton. Using this figure to calibrate the value of I_{hh} and I_{lh} - requiring that a pure lh state is ten times brighter than a pure heavy hole state - the end result is $I_{lh}/I_{hh} = \sqrt{30}$.

These predictions are shown in Figure 16. As one would expect, the brightness relative to an unmixed hh state rises linearly with light-hole fraction, starting at unity for the pure hh state and peaking at 10 for the pure lh state. The degree of polarization, on the other hand, rises very rapidly when a small amount of lh is introduced into the hh state. When the ground state is roughly 9% light hole, the mixed state is completely linearly polarized. At higher levels of mixing, the mixed state is dominated by the circular component contributed by the light hole.

A typical plot of the polarization profile from the indirect excitons at high stress is shown in Figure 17. This data was obtained by taking a number of 2D spatial images of the indirect exciton luminescence, passed through a linear polarizer. For each pixel, the intensity was plotted as a function of polarizer angle, and the degree of polarization and direction of strongest polarization were calculated. This data was taken in collaboration with Nicholas Sinclair; a more detailed discussion of the experimental and fitting procedure is presented in

his dissertation [86].

Next to the experimental data, a plot of the expected polarization angle in the trap based on the lh-hh mixing model discussed above is shown. It can be seen that the general spatial dependence in the bright-regions of the trap match the predicted dependence very well; the polarization is very close to radial and is stronger along the sides of the trap than in the center. The dark spot at the center of the trap is a feature of the luminescence at high stress and will be discussed in detail in the following chapter.

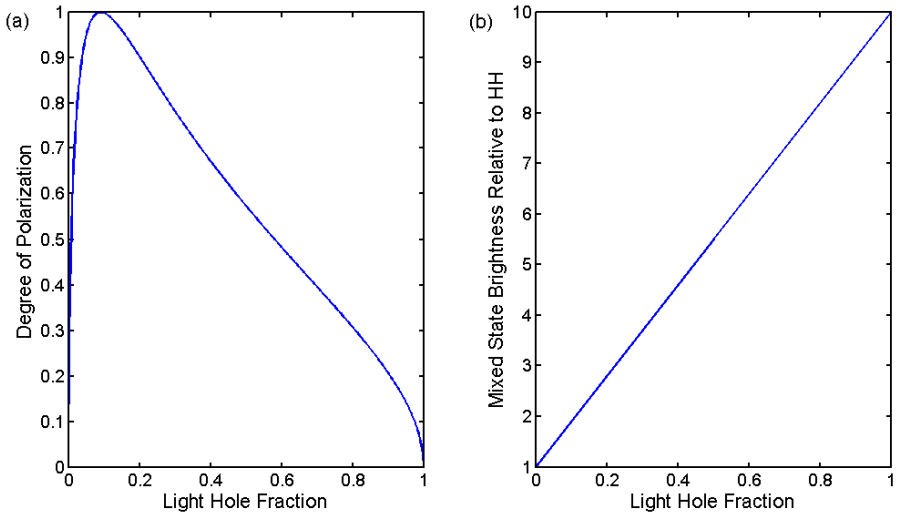

Figure 16: (a) The degree of polarization and (b) brightness of the IX ground state as a function of its light hole fraction, as predicted by the model discussed in the text. It was assumed that the oscillator strength of a pure IX lh exciton is roughly ten times brighter thana pure IX hh exciton.

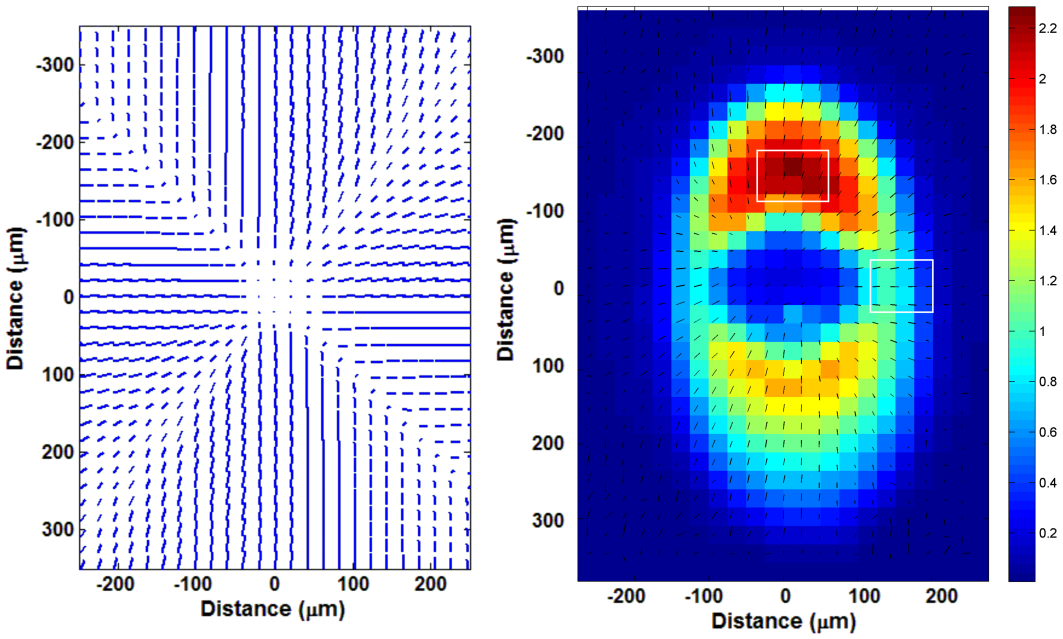

Figure 17: Spatial plot of the degree of polarization (arrow length) and polarization angle of maximum intensity (arrow direction) for the luminescence from the indirect line. Theoretical model (left) compared to measurement (right). Color in experimental plot indicates the log-intensity, in arbitrary units. White boxes in experimental plot highlight the clearly radial polarization at points along [110] and $[1\bar{1}0]$ directions.

3.0 BLACK HOLE EFFECT

The previous chapter dealt primarily with the properties of our system in the low-stress, low-density regime. To observe condensation at a reasonable critical temperature (ideally, within a range achievable with liquid helium-4), it is necessary to explore the high-density regime. The trapping potential is strongly renormalized by the presence of indirect excitons, so in order to maintain a trapped population, the high-density regime necessarily requires high stress.

In this chapter, the current experimental understanding of indirect excitons in coupled quantum wells will be reviewed, followed by a discussion of the experimental results for the strain trapped system. Specifically, the appearance of a "black hole" at trap center - a region of strongly suppressed luminescence that appears sharply at high stress - will be discussed, and two possible mechanisms for this effect will be considered.

3.1 REVIEW OF LUMINESCENCE STUDIES OF CQWS

In the search for excitonic condensation, the coupled quantum well system was not a viable candidate until the late 1990's and early 2000's; it was not until this time that the quality of molecular-beam epitaxial (MBE) growth techniques was high enough to produce sufficiently low-disorder quantum wells [87]. Low disorder is especially important for low-temperature studies, because even small, local variations of the confinement potential can act as traps for excitons. Recall that at 2 K, the thermal energy is around 170 μeV; so disorder in a trap of even a few hundred μeV can lead to localization. Experiments by Kash et al. [88] on 5 nm GaAs coupled-quantum wells with 4 nm $Al_{0.3}Ga_{0.7}As$ barriers indicated that when there is

significant localization due to impurity states, indirect excitons act more like a Fermi system at low temperature.

Some experimental studies in the late 1990's focused on Type II quantum wells formed between Γ-point holes and X-point electrons in adjacent GaAs/AlAs layers with a large magnetic field applied in the growth direction. The role of the magnetic field complicates these experiments, but it has been predicted that direct quantum well excitons in a transverse magnetic field act as an ideal Bose gas and exhibit an increased critical temperature over the zero-field case[89, 90]. A number of suggestive results were reported in this system by Butov et al. in the low-temperature (down to 350 mK) and high magnetic field regime, including enhanced cooling rates at high density [91], increased diffusivity and radiative rate, and a broad, low-frequency noise spectrum associated with the intensity [92]. While these properties could be indicative of superfluidity and stimulated scattering, other explanations were not ruled out [87]. For example, a study of the diffusion dynamics of indirect excitons by Rapaport et al., predicts a non-linear enhancement of the diffusion rate at high density due to the strong dipole repulsion [93].

Early experiments on untrapped indirect excitons in GaAs coupled quantum wells produced extremely suggestive results. Two experimental papers in 2002 revealed the formation of a bright ring hundreds of microns around a focused CW laser spot[94, 95]. The high power and low temperature onset of the ring suggested that it could correspond at the onset of superfluid flow away from the pump spot. Later analysis indicated that this effect (1) only occurred when carriers are excited at high energy (above the barrier band gap) and (2) was also observed in single quantum wells; instead a model based on carrier depletion was proposed [96, 97]. This picture relied on the faster diffusion rate of the lower-mass electrons, which causes a steady-state depletion of electrons and a surplus of holes near the pump spot. Drift-diffusion models accurately predicted a bright ring at the boundary of the electron- and hole-rich regions, and this explanation was generally accepted.

It has been proposed that the border of the electron-rich and hole-rich regions in this system may be a good place to look for exciton BEC. This region is far from the laser spot, and it is likely that these carriers are thermally equilibrated with the lattice. Periodic fluctuations in this region were initially presented as evidence of macroscopic order [98], but

further study revealed that such fragmentation can appear in a classical drift-diffusion model with dipole repulsion [99]. More recent experiments attempted to measure spatial coherence in the luminescence pattern from this system at 100 mK - particularly at the ring boundary and near localized bright spots in the interior of the ring; it was found that a coherence length of a few microns was observable in the ring and outside of localized bright spots[1] [100].

Other experiments have focused on trapped indirect excitons. In one system with a diamond-shaped electrostatic trap [2], High et al. observed spatial narrowing and a coherence length of a few microns (somewhat larger than the coherence length for a classical ideal gas at the same temperature, which is approximately 0.5 μm) [101].

Optical coherence measurements are one of the most common methods for detecting condensation in exciton systems. In a condensate, the entire population can be described by a single, macroscopic wave function with a well-defined relative phase between spatial locations. When an exciton within the condensate radiatively decays, the coherence of the population should be carried over into the luminescence. There are a number of methods for studying optical coherence; High et al. [101] employ a method called shift-interferometry. The goal is to find the first-order spatial coherence,

$$g_1(x, \Delta x) = \frac{\langle E^*(x)E(x+\Delta x)\rangle}{\langle |E(x)|^2\rangle} \tag{3.1}$$

where $E(x)$ is the electric field amplitude at a particular point x. In this measurement, the image of the exciton cloud is split in two in a Mach-Zehnder interferometer setup. One of the images is shifted along the x-direction, by a length Δx. The first-order coherence can be extracted by measuring the intensity of the images from both arms of the Mach-Zehnder interferometer independently (I_1 and I_2) and the intensity of the interference pattern between the two:

$$I_{int} = \frac{I_{12} - I_1 - I_2}{2\sqrt{I_1 I_2}}. \tag{3.2}$$

[1] In this work, localized bright spots are likely defect sites where current filaments through the wells lead to heating and reduced IX radiative lifetime. The reported coherence length drops off to about 1 μm at the center of these spots.

[2] The diamond shape causes the trap to have a harmonic profile alone one dimension. The length-scale of this trap was on the order of 10 μm.

A small tilt from the mirror on one arm of the interferometer along the y-axis results in an oscillating interference pattern in the y-direction. The visibility of the interference fringes is then proportional to the first-order coherence function. In the measurements described above, the coherence is typically characterized by a shift-dependence that looks like,

$$|g_1(\Delta x)| \propto \mathrm{e}^{-\Delta x/\xi}. \tag{3.3}$$

where ξ is a measure of the coherence length. For an ideal, thermal population, the coherence length is given by the thermal de Broglie wavelength (at the lowest temperature studied in [101], 50 mK, the de Broglie wavelength is around 500 nm). The measured coherence length is also dependent on the optical resolution, characterized by the point-spread function (PSF). The primary result of [101] is an increase in the measured coherence length at low temperature; at temperatures above 4 K, ξ sits around the PSF-limit (around 2 μ m) and increases to around 6 μm at 50 mK. In finite systems, a coherence length comparable to or longer than the length-scale of the system is a strong indicator of condensation. In the [101], the HWHM of the population is shown to be 2 - 7 μm at low temperature, depending on power.

A commentary on this work was written by Semkat et al. [102], noting that the inteference visibility is not only dependent upon the measurement resolution, but also can depend on the size of the intensity distribution. Semkat and coworkers claim to be able to quantitatively model the experimental results of [101] by including the exciton cloud size dependence and assuming the population is a thermal source (not a condensate). A reply by High et al. [103], rejects the quantitative result of the commentary - which, they claim, incorrectly assumes an error in the original paper - but does not directly address the dependence of their measurements on the exciton cloud size. Notably, in the original work [101], the rise of the fringe visibility - both in the temperature-dependence and the power-dependence - is accompanied by a drop in the exciton cloud spatial extent.

A recent high resolution shift-interferometry measurement by Repp et al. [104] has attempted to replicate the spatial coherence measurements described above. In this experiment, similar measured coherence lengths are observed at low temperature (250 mK), but it is confirmed by the authors that this observation is a result of the point spread function

of the measurement, not an indicator of spatial coherence in the exciton cloud. This result re-inforces the criticism of Semkat and coworkers [102].

It would be interesting to see if similar measurements in a trapped population with a larger spatial extent would produce similar coherence lengths or if the result scales with the size of the population, as would be expected of long-range coherence in a finite system. Coherence measurements in a trapped light-hole indirect exciton population with a length scale of 50 μm revealed no observable coherence (less than the resolution of the system, about 12 μm) at T = 2 K [86].

A similar experiment performed by Alloing et al. [105] featured coherence measurements in a wide[3], single quantum well system without a trap, in the regime where the aforementioned luminescence ring is observable. It was found that screening due to the spatial-distribution of free electrons and holes effectively results in an electrostatic trap at the edge of the ring at low temperature. In this study, a pulsed 1 μs pump was used to generate the ring, two weak probe pulses were used to study the spatial-dependence of the exciton blueshift shortly after the pulse (10 ns) and later (100 ns). The early pulse is intended to probe the indirect excitons density, the late pulse was intended to probe the low-density trap profile.

At low temperature (below 2 K), the probe measurements in [105] seem to indicate the appearance of a dark population of trapped excitons trapped at the outer edge of the ring, accompanied by a bright trapped population at the inner edge. Furthermore, shift interferometry measurements show a significant increase in the coherence length at a point 5 μm from the ring edge as temperature drops below 2 K, peaking at a coherence length of about 1.6 μm. At high temperature, both the coherence and the electrostatic trap seem to disappear, changing the spatial luminescence profile at the ring edge from the bright and dark populations with a sharp boundary to a broad profile associated, presumably, with untrapped excitons. It is unclear whether the coherence measurements here, due to the drastic change in the luminescence profile, suffer from the same problems associated with varying source size raised by Semkat and coworkers [102]. It is also unclear whether, due to

[3]In this study, the quantum well is wide enough (25 nm) that there is a significant spatial separation between electrons and holes under an applied field, making it similar to the CQW system. A radiative lifetime of around 20 ns is reported [105].

the changing shape of the luminescence profile with temperature, observing the coherence at a fixed distance from the ring is a fair comparison. Further study of this dark population may prove informative and may suggest further tests for condensation.

Other studies attribute the appearance of an dark indirect exciton population to Bose-Einstein condensation. Work with a circular electrostatic trap by Rapaport et al. also reported a drop in the radiative fraction of indirect excitons at low temperature, which coincides with an increase in the blue shift based on the expected bright exciton population [106]; the suggested interpretation was that this corresponds to a preferential population increase of an optically dark state, coinciding with suppressed spin-flip scattering. This hypothesis is inspired by theoretical work by Combescot et al. [107], which proposes that condensation is likely to occur in optically dark spin-states, or will appear as partially dark "gray" condensates [108].

Disorder is typically problematic because it lowers mobility and causes localization. However, a number of works by Timofeev et al. used disorder fluctuations as a trapping potential; these sites were isolated by patterning micron-scale windows in a metallic mask, and studying the luminescence through the windows. This method produced a number of interesting results, such as suppressed $J = \pm 1$ spin-flip times and an increase in the radiative rate below 3.5 K [109]. In later experiments, an electrical bias was applied to the windows, creating a ring-shaped trap at the window-perimeter; in these traps at low temperature, periodic pattern formation in real- and momentum-space were observed [110] as well as a gradual increase in the second-order correlation function above a critical power threshold [111].

While there have been a number of suggestive results reported in the literature, strong evidence of condensation in coupled quantum wells remains elusive. Although simpler to work with, solid state systems tend to be "messier" than similar studies in cold atom research; one must carefully rule out other physical effects which might look like condensation at first glance. In the following section, low temperature, high density experimental behavior of strain-trapped indirect excitons, that was initially suggestive of BEC, will be discussed using two models which rely only on the single particle physics.

3.2 EXPERIMENTAL RESULTS

In the search for evidence of Bose-Einstein condensation of spatially-indirect excitons, the primary interest is in the regime of low temperature and high density. High density is achieved through large optical pump power in conjunction with an applied DC voltage across the sample. As discussed earlier, the IX radiative lifetime increases exponentially with applied voltage in the vicinity of the built-in field. A larger radiative lifetime also leads to a larger steady-state population of indirect excitons. The experiments discussed here are typically either CW - where the steady-state luminescence is observed in the presence of a laser putting out roughly constant power - or chopped - where the laser is chopped on the time-scale of IX equilibration (on the order of microseconds) and the ICCD is gated to eliminate the short-lived DX luminescence.

The excitation source used in the following experiments was a laser diode with a Peltier cooler, which provided a temperature-dependent, tunable wavelength near-resonant to the DX line (which typically sits near 805 nm in 14 nm quantum wells). Indirect excitons were introduced into the system by pumping the direct line, as discussed in Chapter 2. This is typically far more efficient than pumping the indirect line and can also eliminate scattered laser light from the vicinity of the IX luminescence when it is spectrally resolved.

The initial experimental results were performed for 12 nm coupled quantum wells with a 4 nm $Al_{0.45}Ga_{0.55}As$ barrier. It was later observed that the black hole effect is similar in a system with 14 nm coupled-quantum wells, but appears at lower stress. This dependence on the well width is a critical clue to the origin of this behavior; that is, the black hole effect occurs in the stress regime near where the lh-exciton line crosses over the hh-exciton line. For narrower wells, the hh-lh splitting is larger, and this regime occurs at higher stress. The models discussed later will focus on the 14 nm system. Other than the larger critical stress in narrower wells, the experimental observations are qualitatively the same in both systems.

The most striking feature of the high-stress, high-density regime is the dramatic appearance of a dark population at trap center. In Figure 18, the stress dependence of the luminescence is shown. This series was taken with a CW laser at approximately 120 μW average power, resonant to the direct line and focused on the center of the trap. The DX-

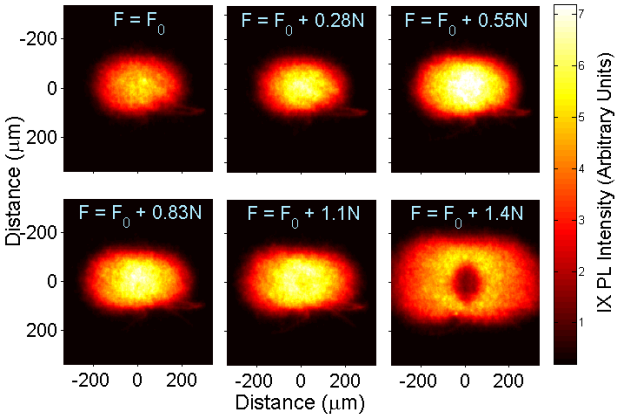

Figure 18: Two-dimensional spatial profile of indirect exciton luminescence at fixed temperature (2.2 K) and pump power (roughly 120 μW), with increasing applied force on pin. x- and y-position axes correspond to weak and strong confinement axes ([110] and [1$\bar{1}$0] crystal directions, respectively).

luminescence and scattered laser light were removed by an 819 nm $\pm$ 20 nm bandpass filter. It was taken at low temperature (2.2 K) and with an additional applied voltage of 0.5 V in the same direction as the built-in field due the p-i-n doping.

It was also observed that at lower optical pump power, the black hole would close up. In Figure 19, a spectrally-resolved, spatial cross-section of the IX luminesence through the trap center is shown as a function of optical pump power. As with the stress series, a CW laser is focused at trap center, resonant to the DX line. The blue shift at trap center starts off at $<$1 meV in the low-density case, but increases significantly (to 3-4 meV) at higher power. At low power, a dark region is not noticeable, but as the IX population spreads out in the trap, the dark region appears and seems to expand slightly. The dim, spatially narrow line at trap center is a background remnant of the tightly focused pump laser (specifically, it is luminescence from impurity states in the substrate). An additional 0.6 V bias was applied in the same direction as the built-in bias.

In Figure 20, it is also shown that the luminescence at trap center darkens significantly and sharply as the temperature drops. This series shows the two-dimensional profile of the

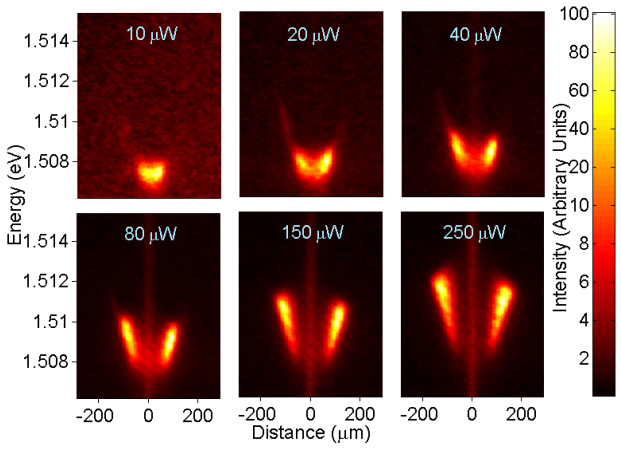

Figure 19: Spectrally resolved cross-section of the luminescence of indirect line at trap-center. Temperature is fixed at 1.5 K, stress is fixed, and optical pump power is varied as shown.x- and y-position axes correspond to weak and strong confinement axes ([110] and [1$\bar{1}$0] crystal directions, respectively).

luminescence at fixed pump power (50 μW) and a fixed stress. The DX luminesence is removed by a bandpass filter, as with the stress series. It is worth noting that the size of the black hole does not seem to grow as temperature drops - rather the brightness drops as temperature decreases. [4]

The experimental properties of the black hole effect in this system have been analyzed extensively by Nicholas Sinclair [86] and Zoltán Vörös [113]. While the details will not be repeated here, the general conclusions are as follows:

- The luminescence line broadening is largest at the center of the trap. For indirect excitons, it is expected that the majority of the energy broadening arises from IX-IX scattering, while the radiative lifetime should be negligible. This suggests that the density of indirect excitons is largest at the center of the trap, but the radiative lifetime of those excitons is relatively long compared to indirect excitons on the sides of the trap [62].

[4]Throughout this chapter, temperature refers to the ambient / bath temperature; it was shown in Vörös et al. [112] that the exciton population can equilibrate to the bath temperature roughly down to 4-5 K. Below that, the population temperature may be warmer than the bath.

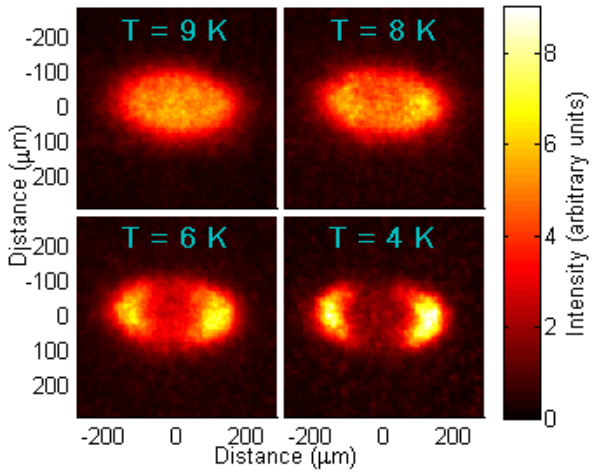

Figure 20: Two-dimensional spatial profile of indirect exciton luminescence at fixed pump power (50 μW) and stress, with varying temperature. Same data set as shown in Sinclair, et al [62]. x- and y-position axes correspond to weak and strong confinement axes ([110] and [1$\bar{1}$0] crystal directions, respectively).

- The general trend of total population lifetime for indirect excitons implies that the radiative lifetime increases with applied stress. It was observed that at the black hole onset, the radiative decay is best described by a double exponential fit, characterized by a short, early lifetime fit ($\sim$ 10 μs) and a noticeably longer, late lifetime (>30 μs) [86].
- New, bright excitons generated on the side of the trap flow through the black hole, indicating it does not act as a sink for particles and that there is not a significant source of non-radiative decay causing the darkening. This also indicates that is not likely a structural barrier [113].
- The relative brightness of the center changes only weakly with power, but at increased power the size of the black hole increases [113, 62].
- The size of the dark region increases with applied voltage. This is likely related to the increase of size with pump power; increased electric field results in a larger lifetime and increased indirect-exciton population [113].

- The geometry of the dark region does not seem to drastically change with temperature. Rather, the relative brightness of the center seems to increase with temperature (somewhat sharply, with the dark spot disappearing typically around 10 K; where $k_BT \approx 0.9$ meV) [113].
- The brightness contrast between the sides and the center varies with experimental parameters, but at high-stress the center can be 3-10 times less intense than the peak-intensity [86, 62].
- The black hole appears at lower stress in 14 nm quantum wells than in 12 nm quantum wells. In 14 nm quantum wells, it is possible to push the system into a stress regime beyond black hole onset where the light-hole indirect exciton becomes the ground state at trap-center. This is signaled by a bright spot at trap center; the black hole is still visible at the periphery of the bright spot. This behavior seems to suggest that the black hole may be related to the hh-lh splitting [86].

Bose-Einstein condensation or the formation of an electron-hole liquid as explanations for this effect were also explored elsewhere [62, 86] and will not be re-iterated. Instead, this work will focus on two possible ways that intersubband coupling (specifically, hh-lh coupling) could result in relative darkening at trap center, and the relative merits of the two models will be discussed.

3.3 MODELING THE BLACK HOLE

In the following sections, two different models for the black hole effect are discussed. From the observations discussed in the previous section, it seems very likely that this feature is related to a drop in the relative radiative rate at trap center - as opposed to a drop in the local indirect exciton density - so both models rely on mechanisms for altering the local lifetime in the trap.

It was mentioned that the IX energy scales linearly with density, but this is somewhat of a simplification. The next section will provide a more thorough discussion of the density-dependent blue shift and the IX-IX interaction.

3.3.1 Modeling Blue Shift

It is expected that the interaction between indirect excitons can be quite complex, particularly in the regime where quantum degeneracy is important and where phase changes may occur. A number of theoretical works have attempted to model this interaction.

In one analysis, theorists Lozovik and Berman examined the relative contributions of the different components of the exciton-exciton interaction in coupled quantum wells; it was shown that in the regime where the interwell seperation is large compared to the Bohr radius, the dipole-dipole repulsion is dominant, and other contributions - from inter-exciton exchange and van der Waals attraction - are negligible [114]. In fact, the reason that inter-exciton exchange is negligible is similar to the reason that intra-exciton electron-hole exchange is negligible; the dipole-dipole repulsion between excitons forms a potential barrier which prevents the overlap between electrons and holes.

A simple approximation showing the linear dependence of the energy on the local IX density can be found by assuming that the indirect exciton density is a uniform distribution. This is typically called the capacitor approximation, because in this picture the IX population is treated as a uniform positive charge density in one well and a uniform negative charge density in the other well. Integrating to find the total energy of this system gives an interaction energy of

$$E_{\text{int}} = \frac{4\pi e^2 d}{\epsilon} n \tag{3.4}$$

where d is the charge seperation length and n is the 2D IX density.

This model ignores the effect of spatial correlation between excitons. For example, one can calculate the indirect exciton density-dependent blue shift by considering the change in energy of one exciton due to the presence of a thermally equilibrated IX population. Imagine the case where a single, classical indirect exciton is pinned to the origin of a coordinate system ($\vec{r} = 0$). If a density of indirect excitons is then added to the system, in thermal equilibrium they will not uniformly distribute themselves in space; instead, they will prefer to avoid the origin due to the repulsive interaction from the initial indirect exciton at the origin. Instead,

one might expect that the distribution will look more like the following [115]:

$$n(\vec{r}) \propto \exp\left[-\frac{U_{\text{int}}(\vec{r})}{kT}\right] \tag{3.5}$$

where U_{int} is the two-particle IX-IX interaction potential, typically approximated as an aligned dipole repulsion. In this approximation, there is a region around a given IX where other indirect excitons are less likely to be found. An expression for the interaction energy between an indirect exciton and a thermally distributed density distribution of other IX would be [115]:

$$E_{Int} = \int n_0 U_{\text{int}}(\vec{r}) \exp\left[-\frac{U_{\text{int}}(\vec{r})}{kT}\right] \mathrm{d}^2\vec{r} \tag{3.6}$$

where n_0 is a scaling factor, such that the total number of indirect excitons in the population, N, is given by:

$$N = \int n_0 \exp\left[-\frac{U_{\text{int}}(\vec{r})}{kT}\right] \mathrm{d}^2\vec{r}. \tag{3.7}$$

The overall effect of correlations in this system is to reduce the effective blue shift; it can be shown that this reduction is most significant at low temperature [115, 116]. This picture is somewhat intuitive. At low temperature, the system is stuck near the most energetically favorable, highly correlated state; at high temperature, it is more likely to find indirect excitons in close proximity. But it is worth mentioning that this approximation still predicts a linear-dependence of the blue shift on density.

A more rigorous analysis of the IX-IX interaction energy was performed by Schindler and Zimmermann [116]; therein, an effective potential between two indirect excitons is calculated by taking the full, four-particle wave function into consideration. An experimental study by Vörös et al. [117] was able to test the temperature dependence of the interaction energy without directly knowing the density by measuring the slope of spectral broadening versus blue shift. The slope measured within the range of 2-20 K agreed with the predictions of Schindler and Zimmermann within a factor of two.

In the density regime considered in this work, the indirect exciton population exhibits a non-negligible amount of density-dependent blue shift, typically on the order of a few meV. For the sake of observing BEC, increasing density requires a deeper strain trap, as a larger

density will fill up the trap quickly, flattening the trap. As far as this study is concerned, the primary problem is how to include the IX-IX interaction in the calculation of the steady-state density in a strain trap.

One simple approach is to assume the the blue shift is proportional to the local density, with proportionality constant γ. Assuming Boltzmann statistics,

$$n(x,y) = n_0 \exp\left[-\frac{V(x,y)}{kT} - \frac{\gamma n(x,y)}{kT}\right] \tag{3.8}$$

where the density relative to n_0 at any point can be uniquely determined by the trapping potential $V(x,y)$, the temperature T, and the blue shift at trap center γn_0. While this expression is clearly non-linear in density, it is relatively easy to solve numerically. It is convenient to re-arrange it as follows:

$$\ln\left[\frac{n(x,y)}{n_0}\right] + \frac{V(x,y)}{k_B T} + \frac{\gamma n_0}{kT}\frac{n(x,y)}{n_0} = 0. \tag{3.9}$$

If the potential is scaled so that $V = 0$ at trap center, n_0 can be interpreted as the density at trap center in the absence of blue shift. Careful experimental analysis of 10 nm coupled quantum wells by Z. Vörös suggested a value for γ of around 10^{-10} meV cm^2 [113]. This measurement differs from predictions by Schindler and Zimmermann [116] by about a factor of 5; it is suspected that the error may lie largely in the difficulty in calibrating the density [113]. It was mentioned earlier in this section that similar measurements which do not require an estimate of the density match the theoretical predictions much more closely [117]. In any case, is important to know this parameter to translate a particular density-dependent blue shift into an absolute density; but the spatial-dependence of the density can be calibrated directly from the blue shift, assuming the blue-shift actually does scale linearly with density.

Note that Boltzmann statistics are used in this model for simplicity. It is not clear whether the black hole effect occurs in a regime where quantum degeneracy is important. But - as the next few sections will show - it may be possible to explain this effect without invoking Bose-Einstein statistics.

3.3.2 Radiative Enhancement from Mixing

One consequence of shear strain at the edges of the trap - as discussed in Section 2.4 - is that the ground-state exciton is a superposition of the light-hole state and the heavy-hole state. The presence of mixing is confirmed by the observation of linear polarization on the edges of the trap with applied strain. It was also shown by the numerical results in Figure 6 that the light-hole exciton is characterized by a distinctintly shorter radiative lifetime (predicted by this calculation to be shorter by roughly a factor of ten).

At first glance, this could result in a relative darkening of the center of the trap in the presence of applied strain. The black hole effect appears in the stress regime near the hh-lh crossover, where hh-lh mixing would be significant. It also appears at lower stress for wider quantum wells, where the hh-lh splitting is smaller [86, 113].

To check this model, the intensity as a function of applied force, temperature and power can be considered. For a given trapping potential, the density can be calculated using (3.9). The density is entirely a function of the local trapping potential, $V(x, y)$, the temperature, and the total trap population. Within the model, the total trap population can be calculated by integrating the density over the trap area. Experimentally, determining the density is somewhat challenging; a measurement of the intensity only provides direct information of the density if the radiative lifetime and the collection efficiency are known. Instead, it is more convenient to use the blue shift at trap center, which - for a given temperature and interaction parameter, γ - will have a one-to-one correspondence to the total trap population in equilibrium.

Assuming non-radiative recombination is small, the intensity of radiative emission can be approximated as the local density times the radiative rate τ_{gs}^{-1},

$$I(x, y) = \frac{n(x, y)}{\tau_{gs}(x, y)} \tag{3.10}$$

where the lifetime of the ground state, $\tau_{gs}(x, y)$, is given by the relative hh and lh contributions,

$$\frac{1}{\tau_{gs}(x, y)} = \frac{|\eta_{hh}^{(gs)}(x, y)|^2}{\tau_{hh}} + \frac{|\eta_{lh}^{(gs)}(x, y)|^2}{\tau_{lh}} \tag{3.11}$$

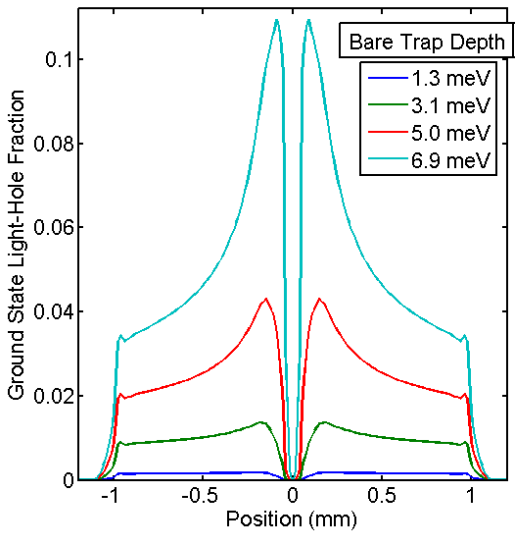

Figure 21: The light-hole fraction of the ground state along a cross-section that goes through the center of the trap, as a function of stress (parameterized by trap depth).

and the hh and lh fractions, $|\eta_{hh}^{(gs)}(x,y)|^2$ and $|\eta_{lh}^{(gs)}(x,y)|^2$, are calculated using the normalized eigenvector components calculated in Sections 2.27 and 2.28. Recall that these are functions of strain, and will also be functions of position in the trap. For simplicity, the mixing fraction is calculated with a single quantum well model. The only parameter in this calculation that could be different for coupled quantum wells is the hh-lh splitting due to confinement; for 14 nm wells with a 4 nm barrier, the difference will not be significant.

Figure 21 shows the light-hole fraction of the ground state as a function of strain trap depth along a cross-section through the center of the trap. At higher stress, the light-hole is predicted to punch through the heavy hole at trap-center (the center of the trap goes from being entirely hh to being entirely lh). For 14 nm quantum wells, it is expected that the lh fraction at the edges of the trap will be not much more than 0.1 before this happens. Using a lh radiative rate of ten times faster than the hh rate, this means that the largest observeable rate will be about twice that of the hh exciton.

Figure 22 shows the simulated dependence of the intensity at fixed temperature ($k_BT =$

0.4 meV) and increasing stress. The blue shift at trap center is fixed at a constant fraction (0.6) of the total trap depth; this condition keeps the size of the IX cloud relatively constant as the stress is increased. It can be seen that at low stress, the intensity profile matches what might be expected for a population of excitons in a harmonic trap with a uniform radiative rate. At higher stress, two bright lobes appear in the intensity. Regardless of blue shift, the density at trap center will always be greater than or equal to the density everywhere else; assuming a maximum mixed-to-unmixed radiative rate ratio of 2:1, this means the maximum observed intensity contrast in this model should be about 2:1.

Figure 23 shows the same model at fixed stress (4.8 meV trap depth) and temperature ($k_BT = 0.4$ meV). The total density in the trap is varied, parametrized by the blue shift at trap center. At low density, the IX population is primarily located in the dark region, making the spatial dependence of the lifetime unobservable. At higher density, the population is pushed further out towards the edges of the trap, causing the two-lobed structure to appear. In two-dimensions, this two-lobed structure would correspond to a bright ring around a dark center. Looking closely at the experimental power series in Figure 19, the interpretation that the population is being pushed out towards a relatively fast-radiative rate region does seem feasible.

In this model, lowering temperature simply reduces the average thermal energy of the IX cloud, which draws the population closer to the center of the trap. At low temperature the population would be primarily in the dark region of the trap and the contrast that causes the black hole would disappear (basically, the same result as lowering power). In other words, it predicts that the black hole should appear strongly at high-temperature, not low temperature. This, of course, is the exact opposite of what is observed experimentally and is a major issue with the radiative enhancement model.

If the IX-IX interaction was strongly temperature dependent, a lowering of temperature could increase IX-IX blueshift; from the semi-classical model discussed in Laikhtman et al. [115], it is expected that there would be an increase in the effective IX-IX interaction strength at low temperature. But, in any case, a drastic increase in the blue shift as temperature drops - which would be necessary to produce black hole onset - is not observed [117].

Furthermore, from Figure 20, it is clear that the shape of the cloud is not drastically

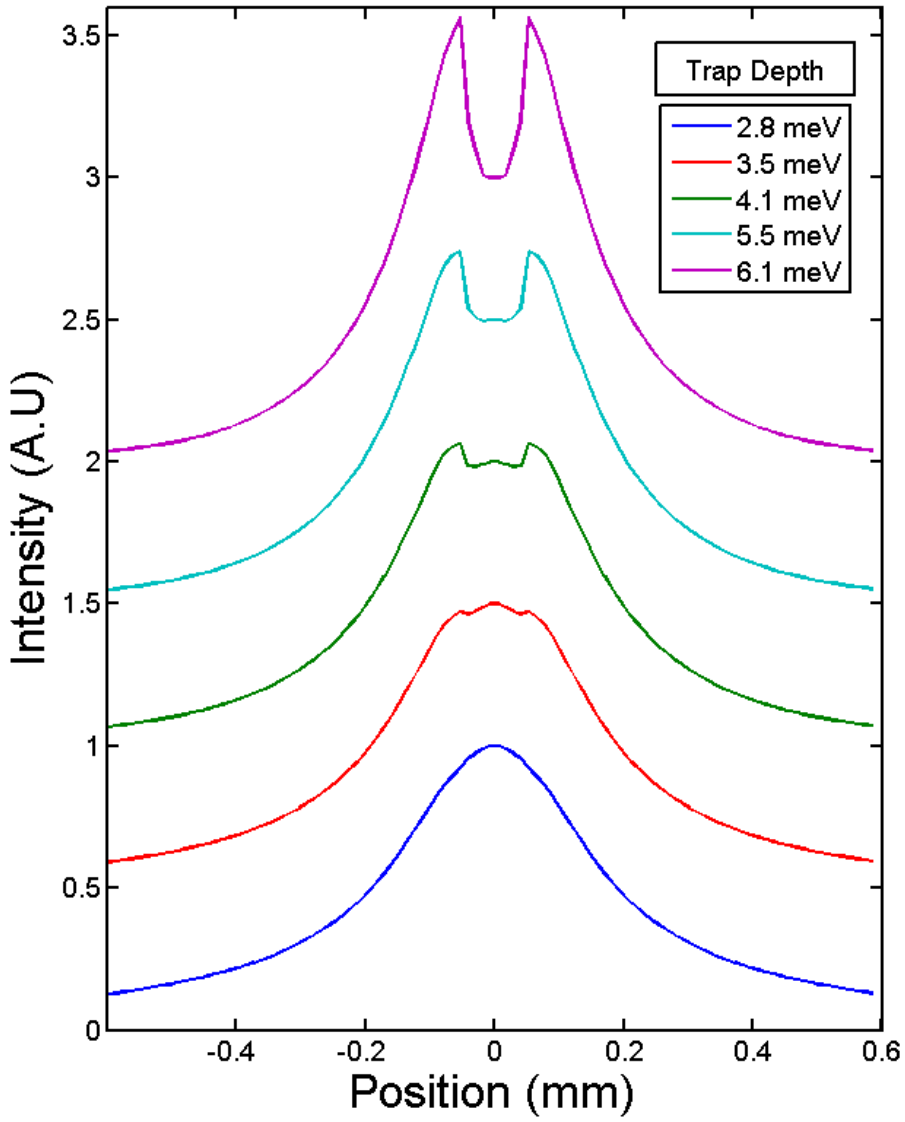

Figure 22: Simulated intensity cross-section through the center of the trap, as a function of trap depth (varying applied force). Temperature is fixed at $k_BT = 0.4$ meV and the density is scaled such that the blue shift at trap center is fixed at 0.6 times the trap depth. Model assumes a single, 14 nm quantum well in GaAs/$Al_{0.45}Ga_{0.55}As$ and that the light-hole radiative rate is ten times faster than the heavy-hole rate.

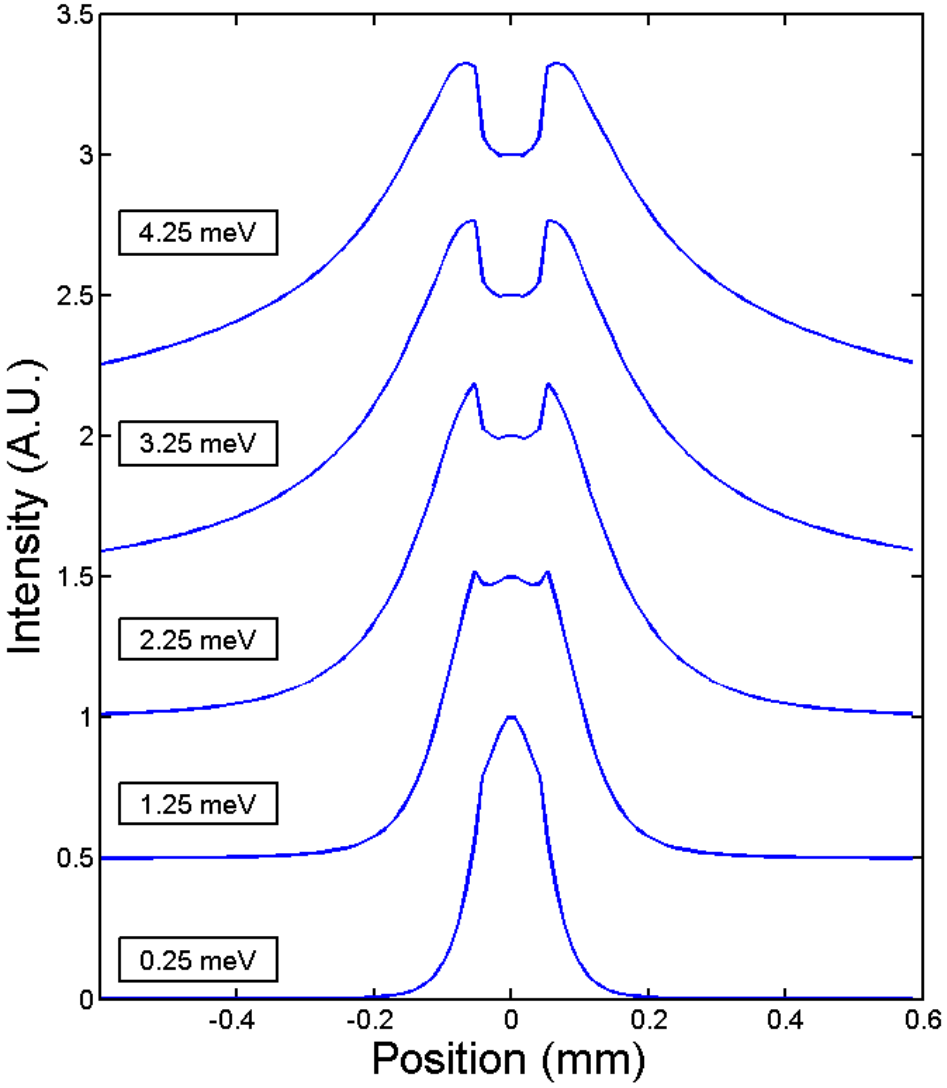

Figure 23: Simulated intensity cross-section through the center of the trap, as a function of density, parametrized by the density-dependent blue shift at trap center. Temperature is fixed at $k_BT = 0.4$ meV and the empty trap depth is fixed at 4.8 meV. The model assumes a single, 14 nm quantum well in GaAs/$Al_{0.45}Ga_{0.55}As$ and that the light-hole radiative rate is ten times faster than the heavy-hole rate.

changing in the regime that the black hole appears. Measurements of the spectral broadening at trap center verify that the density at the center of the trap does not drop when the black hole appears. This strongly suggests that the black hole onset must be occuring due to a relative drop in the radiative rate at the center of the trap with respect to the sides. Within the radiative enhancement model, this comes about due to the appearance of a non-zero light hole component at the edges of the trap; in this model, the intensity contrast between the center and the sides is entirely determined by (1) the spatial variation of the density, (2) the fraction of light-hole in the ground state as a function of position, and (3) the ratio of the radiative rate between the hh and lh components. Having excluded a drastic drop in density as the cause of the black hole, the radiative enhancement model could only explain the temperature dependence if the mixing fraction or the ratio between the hh and lh rates were strongly temperature dependent. It is expected that the mixing fraction depends primarily only on the strain and there is no reason to expect that the radiative rate of the heavy-hole exciton would exhibit drastically different temperature dependence than that of the light-hole exciton.

Despite the suggestive appearance of a region of suppressed luminescence, there are a number of other issues that indicate that the radiative enhancement picture is not sufficient to explain the black hole effect.

The simulated intensity profile also does not seem to have the same intensity contrast that is observed in the experimental data. From the calculations shown in Figures 21, 22, and 23, it appears that the model predicts that the maximum intensity along the sides of the trap are at most 2:1. Experimentally, 3:1 to 10:1 intensity contrast is observed between the sides and the center of the trap. The contrast can be increased somewhat by adjusting model parameters, but this sort of ad-hoc fix seems dubious.

If the radiative enhancement due to mixing is significant enough to cause a relative darkening of the center, the black hole onset should also coincide with decreased population lifetime. Given that the experimentally measured population lifetime increases with stress, as discussed in the list of experimental observations in Section 3.2, it seems that the radiative enhancement due to the lh fraction is overwhelmed by some other effect which increases the population lifetime. It is also worth noting that a dramatic reduction in population lifetime

is not observed when the light-hole crosses the heavy-hole and becomes the ground state at trap center, which seems to contradict the prediction in Figure 6. When the ground state at trap center becomes entirely light hole, one would expect that if the light hole does exhibit a much faster radiative rate, the population lifetime would decrease dramatically. However, this plot is calculated at zero stress; the effect of strain on the effective mass of the light-hole band is not considered and - as will be discussed in the following section - can be significant.

3.3.3 Momentum-Space Indirect Valence Band

In Chapter 1, the dispersion relationship for unstrained GaAs quantum wells was plotted, showing that the light-hole band is k-space indirect (Figure 3). This is consistent with photoluminescence studies, in which the light-hole exciton line is only visible in the spectrum at high-stress and at elevated temperature [86].

This observation seems to indicate that the heavy-hole band may become momentum-space indirect at high stress, as the darkening at trap center seems to occur near the lh-hh crossover point. One theoretical analysis of the effect of a compressive uniaxial stress on the band structure of a 10 nm GaAs/$Al_{0.21}Ga_{0.79}As$ quantum well, performed by Andreani et. al. [118], predicted that the hh band does become indirect near the hh-lh crossover point[5].

To test the strain dependence of this property, the expected single-particle dispersion relationships at trap center were calculated, where $\epsilon_{xx} = \epsilon_{yy} \approx -\epsilon_{zz}$ and $\epsilon_{xy} = \epsilon_{xz} = \epsilon_{yz} = 0$. This was done using the code presented in Appendix A. These calculations include single-particle effects for both the conduction and valence bands, but do not include the binding energy.

In Figure 24, the results are shown for 14 nm GaAs coupled quantum wells with 4 nm $Al_{0.45}Ga_{0.55}As$ barrier, in an electric field of 1 mV/nm. In (a), the energy at trap-center for the hh- and lh-excitons is shown as a function of applied force (excluding changes in the binding energy with strain). Note that the absolute scale of the applied force should be taken with skepticism; due to uncertainty regarding the contact area, it is difficult to

[5] A compressive or tensile strain can push the hh and lh bands closer together, provided $Q = \epsilon_{xx} + \epsilon_{yy} - 2\epsilon_{zz}$ is greater than zero. This will still accompany an overall increase in the exciton energy, which is typically dominated by the electronic term and is proportional to $\epsilon_{xx} + \epsilon_{yy} + \epsilon_{zz}$

calibrate the absolute value of the force. In comparing experimental data with this model, it is more appropriate to pay attention to the bare trap depth.

Note that in Figure 24(a), the lh-state is predicted to cross over the hh-state around F = 1.2 N. Experimentally this serves as a point of reference; at higher stress than that associated with black hole onset, the light-hole exciton line appears and punches through the heavy-hole line. This bright spot starts off at comparable energies to the dim luminescence at trap center, then moves below hh trap center at higher stress.

One possible explanation for the appearance of the black hole is that the heavy-hole subband (or more, generally, the highest valence subband) becomes momentum-space indirect in the presecence of strain. Recall that an indirect-gap semiconductor is one in which the highest valence band state does not line up with the lowest-conduction band state in k-space. In semiconductors with indirect gaps (such as silicon), radiative recombination is strongly suppressed.

In Figure 24(b), a plot of the difference between the energy at $k = 0$ and the lowest hole energy subband minima along the (110) axis is shown. At zero stress, the ground state (the heavy hole) is momentum-space direct, so the minimum is at band-center, and this difference is equal to zero. At an intermediate stress around the hh-lh cross-over point, there appears to be a minimum at non-zero k which quickly appears and then disappears past the cross-over point. The energy minimum along the (110) direction is the overall minimum of the subband; this can be seen from Figure 25, which shows calculated 2D k-dependence of the energy of the (a) ground and (b) excited hole subbands near the $F = 1.2N$ case shown in Figure 24.

To better illustrate what is happening, the plots in Figures 24(c)-(f) show cross-sections of the dispersion along the (100)- and (110)-directions at varying force. First at zero strain (a), right after the indirect minimum appears (b), where the indirect minimum is deepest (c), and after the ground state has become direct again (d).

Using the same numerical procedure, it is possible to determine the location of the valence band maximum and the direct-to-indirect gap - where applicable - for any given strain. This was performed for the 2D strain profile at a range of applied force values; the calculated intensity profile was plotted in Figure 26. It is assumed in these calculations that

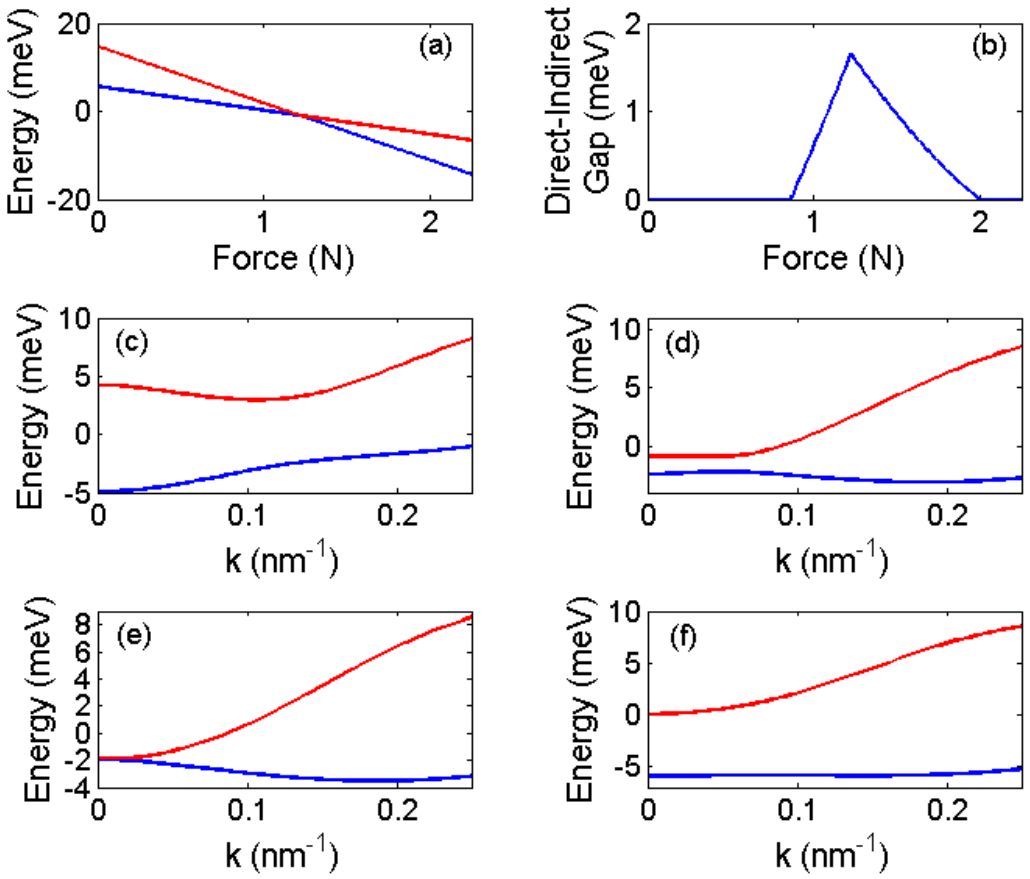

Figure 24: Modeled behavior of the hh- and lh-bands at trap center as a function of applied force (14 nm CQW, 4 nm barrier, 1 mV/nm electric field). In (a), the energy of the lowest two hole subbands. As shown in Figure 25, indirect-minima appear around F = 0.86 N, with an energy gap shown in (b) along the (110) axis. This is further illustrated by band-digram cross sections at (c) F = 0, (d) F = 1.0 N, (e) F = 1.2 N and (f) F = 2.0 N. In all sub-figures, blue and red lines indicate the lower- and upper-states, respectively.

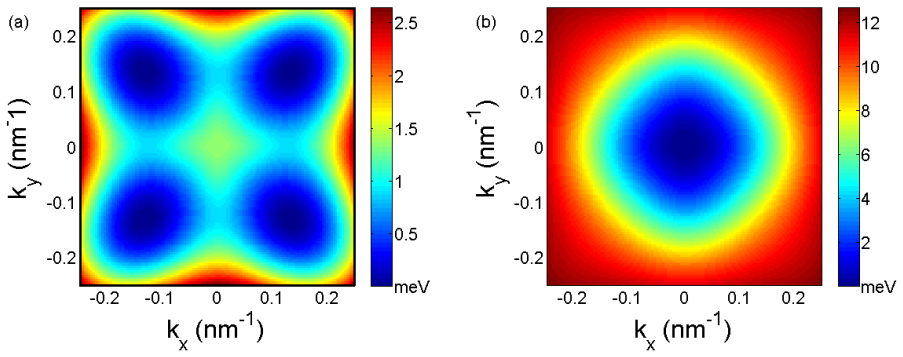

Figure 25: The calculated in-plane k-dependence of the (a) lowest and (b) second-lowest hole energy subbands near the hh-lh crossover, roughly where the expected direct-to-indirect gap is the greatest ($F = 1.2N$ in Figure 24)

.

the indirect gap, ΔE_I reduces the recombination rate as follows:

$$\frac{1}{\tau} = \frac{1}{\tau_0} \exp\left[-\frac{\Delta E_I}{k_B T}\right] \tag{3.12}$$

where τ_0^{-1} is the rate for direct recombination and the energy gap is the difference between the valence band maximum and the energy at $k = 0$. In other words, in order for recombination to occur, holes must be thermally excited to near $\vec{k} = 0$ [6].The density was calculated using the same mean-field approximation employed in the previous section. The temperature is fixed at 4 K and the density-dependent blue shift is scaled at 20% of the trap depth. Encouragingly, in the simulation a dark region appears sharply at trap center at a critical stress value.

A similar calculation was done at fixed stress (6.2 meV) and density, while varying the temperature. Of course, due to the assumed exponential suppression of radiative recombination, the trap center brightens at higher temperature, as shown in Figure 27. Recall that this feature is completely absent from the radiative enhancement model. Also, the fact that the onset temperature predicted by the direct-to-indirect gap is roughly the same as the critical

[6]Recall that the center-of-mass momentum of the electron-hole pair must be near-zero to lie within the light-cone.

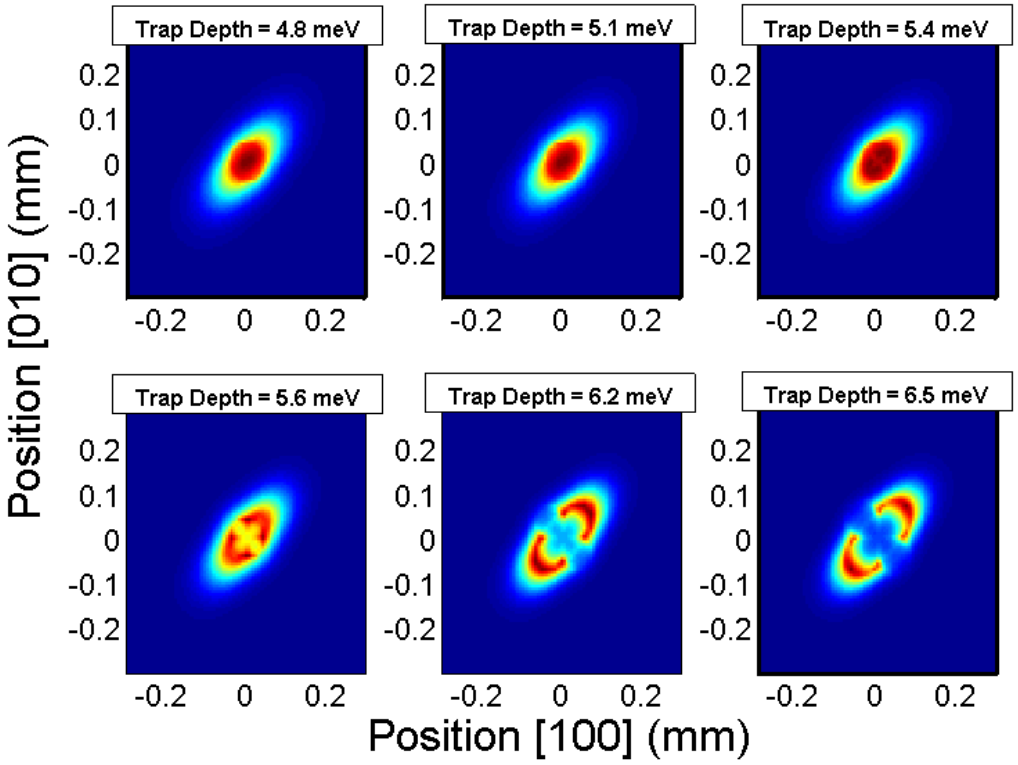

Figure 26: Simulation of the intensity as a function of position, using the indirect-gap model discussed in the text. Stress is varied, temperature is fixed at 4 K ($k_BT = 0.34$ meV), and the density is scaled such that the blue shift at trap center is 20% of the trap depth. Effect of radiative enhancement from the light hole fraction is excluded, piezo-electric effect included. Compare to data shown in Figure 18 (note that elongation direction along [110] direction is consistent with weak axis in Figure 18).

temperature observed experimentally may be persuasive. The maximum gap predicted by Figure 24 is between 1-2 meV, which corresponds to roughly 10-20 K.

While the approximation in (3.12) predicts the stress- and temperature-dependence well, the power dependence of the black hole shape is not as accurate at first glance. This can be seen in Figure 28(b); at the chosen stress and temperature, the size of the black hole is essentially independent of power (the peak values staying fixed around $\pm$ 60 μm as the blue shift at trap center is varied). The reason for this is that the appearance of the direct-to-indirect gap is spatially sharp (the rate predicted by Equation (3.12) as a function of position is shown in Figure 28(a)). For a more gradual spatial change in the local lifetime, the blue shift renormalizes the trap and pushes the population more towards the brighter sides of the trap. The compromise between the weaker emission near the center and the larger population will produce maxima that shift outward as the total density in the trap increases. With a sharp spatial cutoff to the luminescence suppression, the intensity peak locations will be independent of power.

The simple exponential dependence given in (3.12) is a rather rough approximation. It assumes that the electrons and holes are acting entirely as free carriers and only recombining at $\vec{k}_h = 0$. The most accurate way to do this calculation is to re-calculate the bound exciton states associated with the hole dispersion relationship at each particular spatial location. Performing this calculation at each spatial location for each strain value would be extremely computationally intensive. A simple approximation to model this behavior is to fit an effective mass to each new local valence-band minimum and relate them to an exciton state with effective mass:

$$m_{\mathrm{ex}} = m_{\mathrm{e}} + m_{\mathrm{h}}(x, y). \tag{3.13}$$

The effective mass of the electron is independent of stress. The effective mass of the holes is found by fitting the hole dispersion relationship near the minima as a 2D parabola with principal axes along the (110) and $(1\bar{1}0)$ directions,

$$E_{\mathrm{hole}} = \frac{\hbar^2}{2m_{h,110}} k_{110}^2 + \frac{\hbar^2}{2m_{h,1\bar{1}0}} k_{1\bar{1}0}^2. \tag{3.14}$$

It was observed that, in the indirect regime, there are typically five minima in the hole

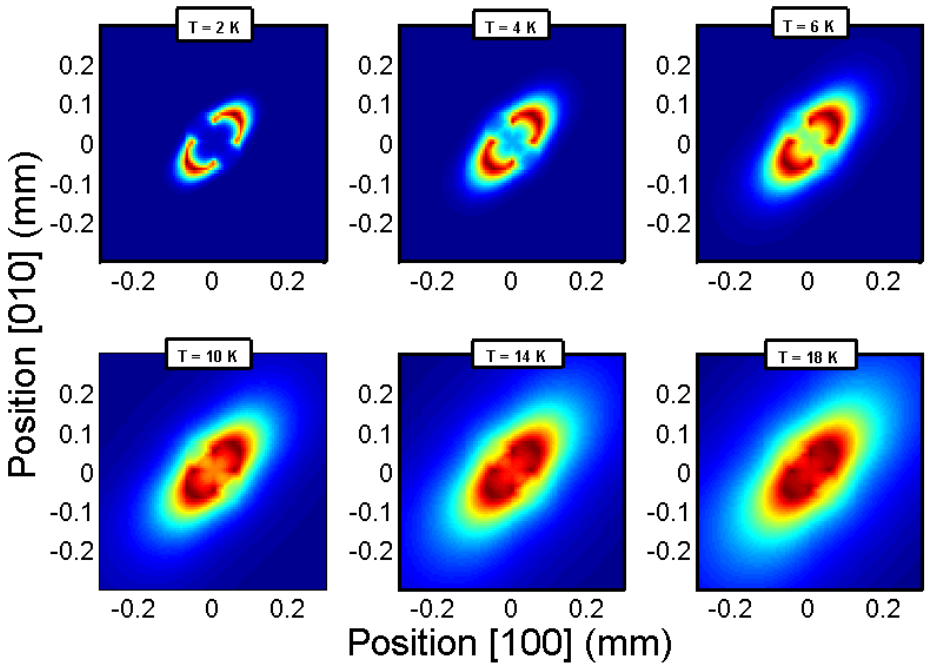

Figure 27: Simulation of the intensity as a function of temperature, using the indirect-gap model discussed in the text. Stress is varied, the trap depth is fixed at 6.2 meV, and the density is scaled such that the blue shift at trap center is 20% of the trap depth. Effect of radiative enhancement due to the light hole fraction is excluded, piezo-electric effect included. Compare to data shown in Figure 20 (note that elongation direction along [110] direction is consistent with weak axis in Figure 20).

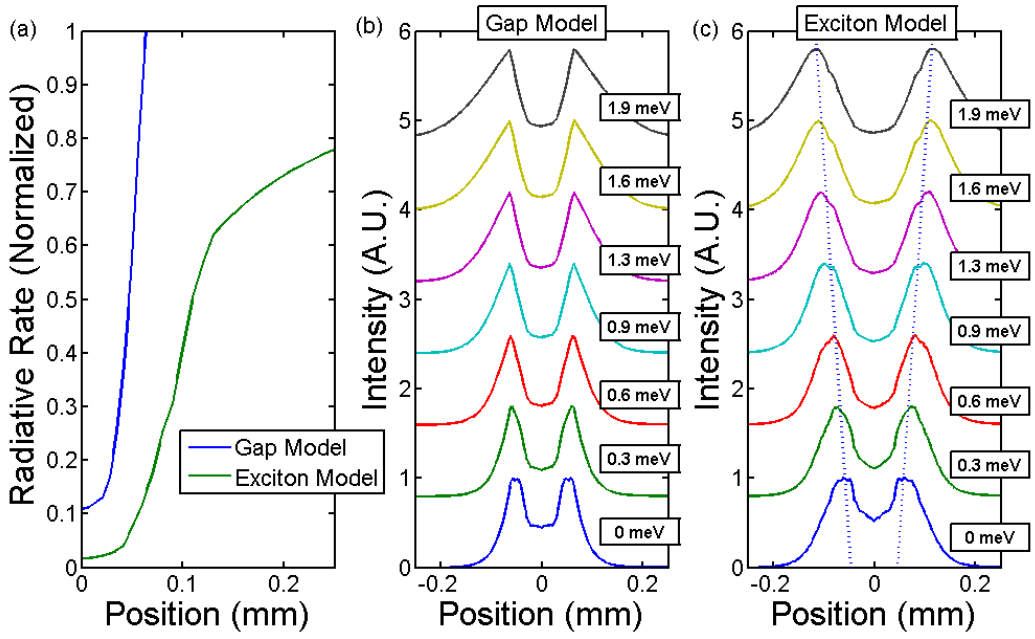

Figure 28: Simulation of the intensity as a function of density-dependent blue shift at trap center - using the rate calculated from the strain-dependent band structure (blue) and a more complex model treating each minima as a distinct exciton state (green). The rate is normalized such that it goes to unity far from trap center. The temperature is fixed at 4 K and the total trap-depth is fixed at 6.6 meV. Effect of radiative enhancement due to light hole fraction is excluded, piezo-electric effect included. Compare to experimental series shown in Figure 29.

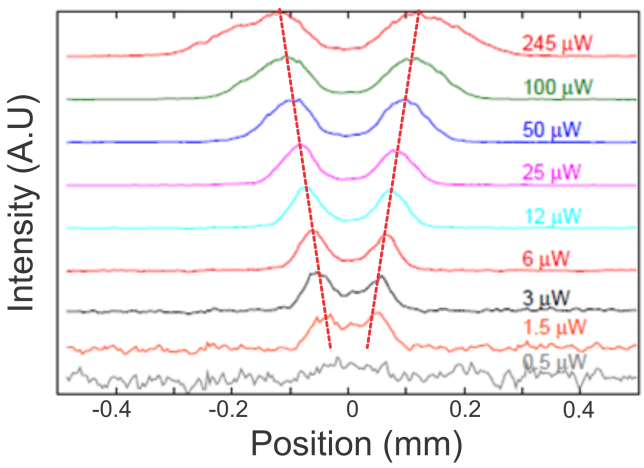

Figure 29: Measurement of intensity as a function of pump power for 12 nm quantum wells at varying pump power resonant to direct line. Held at fixed temperature (1.8 K) and applied bias (0.51 V), using bandpass filter to remove direct luminescence. Using data originally presented in [113].

dispersion - a shallow minimum at $\vec{k} = 0$, two minima approximately along the (110)-axis, and two minima along the $(1\bar{1}0)$-axis. For simplicity, these three types of states will be labeled A, B, and C. Considering a cross-section through the strong axis, symmetry requires that the two B exciton states are identical and the two C exciton states are identical. At trap center, all four states are identical; away from trap center, the B states will be slightly lower than the C states.

Away from trap center, the A exciton state will also lower until the valence band becomes direct; meanwhile, the B and C states will become shallower until they disappear entirely. It is assumed in this model that all three exciton states have identical binding energy. Although they are associated with different effective masses, the binding energy depends on the reduced mass of the electron/hole pair, which will be dominated by the much lighter electron mass ($0.067m_0$).

Assuming the form of the dispersion relationship in 3.14, the exciton density of states

will be given by:

$$\frac{g(\epsilon)}{A} = \frac{\sqrt{m_{ex,110} m_{ex,1\bar{1}0}}}{\pi\hbar^2}. \tag{3.15}$$

For Figures 28(a) and (c), the hole dispersion relationship was calculated at a range of points along the (110) axis, starting at the trap center and increasing up to 400 μm from the center. At each point, the effective mass (m_{eff}), energy at the minimum (E_0), and depth of the minimum (ΔE) was calculated. Under the assumptions above, the total number of excitons - $N_A + N_B + N_C$ - can then be calculated as follows [7]:

$$N_A \propto \int_{E_0^{(A)}}^{E_0^{(A)}+\Delta E^{(A)}} g_A(\epsilon) \mathrm{e}^{-\epsilon/k_B T} \mathrm{d}\epsilon, \tag{3.16}$$

$$N_B \propto 2 \int_{E_0^{(B)}}^{E_0^{(B)}+\Delta E^{(B)}} g_B(\epsilon) \mathrm{e}^{-\epsilon/k_B T} \mathrm{d}\epsilon, \tag{3.17}$$

$$N_C \propto 2 \int_{E_0^{(C)}}^{E_0^{(C)}+\Delta E^{(C)}} g_C(\epsilon) \mathrm{e}^{-\epsilon/k_B T} \mathrm{d}\epsilon \tag{3.18}$$

with the end result,

$$N_{\mathrm{A}} \propto k_B T \left[\sqrt{m_{\mathrm{ex},110}^{(\mathrm{A})} m_{\mathrm{ex},1\bar{1}0}^{(\mathrm{A})}} \mathrm{e}^{-E_0^{(A)}/k_B T} \left(1 - \mathrm{e}^{-\Delta E^{(A)}/k_B T} \right) \right]. \tag{3.19}$$

The expressions for the B and C states will be identical, changing only the three relevant parameters. It is assumed that only direct recombination is allowed (meaning only the A excitons can recombine) and only excitons within the light cone can recombine. Recall from the discussion in Section 1.2 and Figure 1 that conservation of momentum and energy limits the range of exciton k-values that can radiatively recombine. In order to couple with photons outside of the sample (in air), energy must be conserved,

$$\hbar c \sqrt{k_{z,ph}^2 + k_{||}^2} = E_{\mathrm{ex}} \left(\vec{k} = 0 \right) + \frac{\hbar^2 k_{||}^2}{2 m_{ex}} \tag{3.20}$$

where conservation of momentum requires that $k_{||}$ be the same for the exciton and photon. The edge of the light cone is where $k_{z,ph} = 0$, meaning all energy is going into matching the

[7] Ultimately, the goal is to calculate the ratio of radiatively accessible excitons to the total exciton population, which will then be normalized to the unstressed value. So, for simplicity, these terms will only be calculated up to a proportionality constant.

in-plane momentum. In the limit where the energy gap is large compared to the exciton in-plane kinetic energy, the light cone is defined by the following condition:

$$k_{||} \leq \frac{E(k_{||} = 0)}{\hbar c}. \tag{3.21}$$

For a gap energy of 1.52 eV near T = 0 and a confinement energy of about 30 meV, this corresponds to a k-value of 7.9 μm^{-1}. For an exciton dispersion relationship $E_{\text{ex}}(\vec{k})$, the fraction of carriers within the light cone is given by:

$$f_{\text{LC}} \propto \frac{1}{N_A}\left(\frac{L}{2\pi}\right)^2 \int_{\text{k in LC}} \mathrm{e}^{-E(\vec{k})/k_B T}\mathrm{d}^2\vec{k} \tag{3.22}$$

The energy spread associated with carriers in the light cone is expected to be on the order of a few μeV, which will be small compared to $k_B T$ at 2 K. Under this approximation, the integrand of (3.22) is approximately unity. This means that the number of excitons within the light cone can be approximated as:

$$N_{\text{LC}} \propto \left(\frac{L}{2\pi}\right)^2 \pi \left(\frac{E_{\text{gap}}}{\hbar c}\right)^2 \mathrm{e}^{-E_0^{(A)}/k_B T} \tag{3.23}$$

Finally, assuming the radiative rate is slow enough for the system to remain in thermal equilibrium, the rate will be proportional to the overall fraction of excitons within the light cone:

$$\frac{1}{\tau_{\text{rad}}} \propto \frac{N_{\text{LC}}}{N_A + 2N_B + 2N_C} \tag{3.24}$$

Using this expression and fitted values for the exciton parameters, the radiative rate as a function of position is plotted in Figure 28(a). Compared to the model using only the direct-to-indirect gap, this result is characterized by a distinctly lower radiative rate at the center of the trap and does not exhibit a sharp cutoff at the point where the band structure becomes indirect. Instead, the rate slowly approaches the expected unstressed radiative rate; the curve is normalized so that the tail approaches unity far from the center of the trap. Outside of the k-space indirect region, the variation in the rate comes from the changing fraction of excitons within the light cone (due to the varying effective mass).

From the expression in (3.24), a plot of the intensity distribution along the strong axis as

a function of total density (parametrized by the blue shift at trap center) is shown in Figure 28(c). In the gap model (using the expression in (3.12)), shown in Figure 28(b), the size of the dark region is constant. In the exciton model, the size of the black hole is small at low density and grows as the blue shift pushes excitons into the brighter region. The dotted line on plot Figure 28(c) roughly traces out the peak intensity across the series; the position of the peak intensity grows from around 60 μm at the lowest density, to around 110 μm. This result compares well to a similar experimental series shown in Figure 29, where the indirect exciton density is changed by varying the optical pump power.

3.4 CONCLUSIONS

A number of explanations have been considered for the sharp suppression of radiative emission of indirect excitons at trap center. Initially, Bose-Einstein condensation was an attractive possibility, given that the effect appears to have a dramatic high density and low temperature onset [119]. Since this effect has been observed, a number of works, both theoretical [107] and experimental [106], have proposed that a condensate of indirect-excitons will be optically dark, or that a persistent dark population of indirect excitons might be a symptom of a condensate. But subsequent tests for BEC in the black hole regime, such as measurements of optical coherence from the emitted light at trap center, did not support this hypothesis [62].

The radiative enhancement model discussed in Section 3.3.2 was presented in Sinclair et al. [62] as one possible explanation for the darkening effect, with the caveat that many of its features were not explained by the model; e.g, the temperature-dependence, the fact that the modeled relative degree of darkening was not as significant as observed, and the lifetime variation with strain. In that analysis, it was suggested that the black hole effect may appear because of radiative enhancement due to the light hole fraction in conjunction with some other effect, such as an electron-hole liquid phase transition.

The appearance of a momentum-space indirect bandgap at intermediate strain seems to the explain all the major features of the luminescence suppression, tying together most of the

information that has been gathered about this effect since it was first observed in 2007. Still, there are a few experimental tests that could be used to verify that it is the dominant factor in the black hole effect. For example, one strong point in favor of this model is that it would exhibit the same lifetime characteristics observed experimentally - a relatively short initial lifetime (associated with the high density black hole regime), followed by a longer lifetime at low density (where the majority of the population is in the dark region). The temperature dependence of the radiative lifetime was not studied extensively in the black hole regime; it would be expected that the late lifetime associated with emission at trap center should drop exponentially as temperature decreases, as the population of holes at $k = 0$ drop.

Assuming that the proposed model is correct, where does it leave this system in the search for Bose-Einstein condensation of indirect excitons? At face value, the suppression of direct-bandgap emission at trap center could be problematic, particularly if optical measurements are the primary tool of investigations Even if the direct transition is thermally allowed, the ground state of the system - which is momentum-space indirect, may not be optically accessible in the BEC regime. Still, it is worth remembering that one reason indirect excitons are a desirable system in the search for BEC is that they have a long radiative lifetime. If this effect is now understood, this method could provide an additional tool for enhancing the radiative lifetime of indirect excitons. Furthermore, the interaction between the hh-lh bands could open the door to experiments that are not possible with other trapping techniques.

Alternatively, this regime can be avoided entirely by switching to narrower quantum wells. If a structure were designed with a hh-lh splitting of greater than 20-30 meV, it is likely the sample would break well before any band-mixing effects became noticeable. While there are trade-offs with going to narrower wells (such as increased disorder scattering), it could allow for a much less complicated strain trap.

It is also worth considering that it may not be as easy to detect condensation in the IX system; in the microcavity polariton system, optical coherence is easily observable in the BEC regime. But, in the same way that liquid helium-4 does not exhibit the same, drastic k-space narrowing that is observable in weakly interacting atomic systems, it may be likely that such signatures will not be as dramatic in IX systems.

Another approach to this system is to search for superfluidity by performing transport

measurements. However, because excitons are charge neutral, performing transport experiments on indirect excitons is not as straightforward as it is for unbound carriers. In Chapter 4, a method for making transport measurements on optically injected excitons will be explored in detail.

4.0 TRANSPORT

Transport measurements are one of the primary tools of semiconductor physics. Transport typically refers to the motion of charge carriers in response to some stimulus, usually to an applied electric potential gradient. Transport measurements are not as straightforward in excitonic systems; due to the charge neutrality of excitons, they do not experience drift in response to an in-plane electric field.

The experimental work discussed in the previous chapters dealt with excitons that are optically generated and studied with optical measurements (predominantly photoluminescence spectroscopy). However, there has been a great deal of work in the study of coupled electron-electron, hole-hole and electron-hole 2D layers (typically called bilayers), which - in certain regimes - strongly resemble indirect excitons in coupled quantum wells. There have been a number of claims of condensate-like effects in these systems. In the following section, a brief literature review of these experimental studies will be presented.

For a number of reasons, there has been little overlap between optical studies and transport measurements. In the remainder of this chapter, a method of doing transport measurements on optically generated excitons will be proposed and the preliminary results will be discussed.

4.1 REVIEW OF TRANSPORT EXPERIMENTS IN BILAYERS

The Eisenstein group at Caltech was one of the first to explore independent contacting of coupled bilayer systems. Generally, these structures utilized coupled 2D electron gases (2DEG); in other words, structures where selective doping sets up equilibrium electron populations

in both wells. This method of achieving independent well contact requires thin samples ($\approx 50\mu$m) patterned with etched mesa structures. Diffused indium contacts are used to provide contact with both wells and bias contacts are patterned on both top and bottom surfaces to cut off individual wells [120]. By adjusting the bias values, the conducting path between any two diffused indium contacts can be restricted to either individual well, both wells, or neither (cutoff behavior is demonstrated by the conductance dropping off with two distinct plateaus as a function of cutoff bias, corresponding to cutoff of both wells). This behavior is similar to the operation of a MOSFET, where the flow of current can be cut off by an applied bias at the gate. The bilayer structure in this type of system is typically composed of two wide quantum wells (around 20 nm) and a relatively thick $Al_xGa_{1-x}As$ barrier. The barrier thickness and height are both typically larger than in CQW optical studies, to strongly suppress tunneling between wells.

Another method for constructing 2D electron-hole systems is the undoped electron-hole bilayer (uEHBL) device used by the Sandia National Labs group [121]. The basic idea behind this system is that n-type NiGeAu contacts and p-type BeAu both make contact with the wells. The sample is thinned carefully using an epoxy bond and stop etch (EBASE) technique. This approach uses a preliminary HF wet etch, employing an $Al_{0.55}Ga_{0.45}As$ layer as a stop-etch, then a secondary citric acid etch step, using GaAs as a stop-etch. This precision is necessary, because the relative position of each well with respect to the top and bottom contacts determines the majority carrier in each well. For example, the population in the bottom well is independently controlled by the bottom gate, and the population the top well is independently controlled by the top gate. This allows a balanced population of electrons and holes to be established without resorting to a large magnetic field or optical pumping.

It is possible to explore electron-hole pairing in 2DEGs under a large magnetic field in the growth direction. In the presence of a magnetic field perpendicular to the plane of the quantum well, confined electrons will undero cyclotron motion in the plane of the well. If the magnetic field is sufficiently large, the radius of that motion will be small enough that quantization effects are important (the electron must fit an integer number of wavelengths in a round trip). Depending on the radius of these orbits, a finite number of electrons can

fit in a particular spatial area. The degenerate states associated with electrons moving in orbits of the same size is referred to as a Landau level. When the number of electrons is such that no more electrons associated with the minimum cyclotron radius can fit in a particular spatial area, that is referred to as the first Landau level being filled. In the same way that vacant electronic states can be treated as positively charged holes, a partially filled Landau level of a 2DEG can also be treated as a mixed population of electrons and holes [122].

In the bilayer 2DEG system, interesting effects can be observed when the two layers are coupled. If the two layers are close enough[1] they effectively share their Landau level. In other words, an electron in either the top or bottom well will take up the spatial area associated with a particular Landau level. If the magnetic field is such that the Landau level of a single well would be filled (referred to as unity total filling fraction, $\nu_T = 1$), the system is expected to be in a state such that each well is effectively in filling fraction 1/2. So each layer can be treated as equal populations of electrons and holes.

The Eisenstein group published a number of papers where they examine interlayer tunneling current as a function of magnetic field. There are three primary experimental results which are cited as being indicative of coherent pairing: resonant tunneling between layers, strong Coulomb drag between layers, and a drastic drop in the counterflow Hall resistivity [124, 125].

Tunneling conductance is typically measured by using a small-AC signal (in the range of 10-100 μV) on top of a larger DC bias; in experiments by Spielman et al., the small signal bias is placed across the two wells, and the resulting current through the wells is measured as a function of DC bias[126, 123]. In these papers, a large small-signal differential conductance (dI/dV) is measured at zero interlayer voltage (peaking at around 20-50 times higher than the conductance at non-zero DC bias). This resonant peak is only observed near $\nu_T = 1$, disappears at larger effective barrier widths d/ℓ, disappears at high density [126], appears gradually below 200 mK [123], and is quenched by in-plane magnetic field [123]. The resonant peak corresponds to a width of a few μV and is associated with a current discontinuity of around 30 pA; in the non-differential I-V curve, the current peak near zero bias is around

[1] In these systems, the relevant length scale is the magnetic length, $\ell = (\hbar/eB)^{1/2}$; effects attributed to coupling are typically observed around $d = 1.6\ell$ [123].

15 pA, dropping off to around 10 pA away from the resonant peak [123].

The significance of tunneling measurements is that a resonant enhancement of tunneling can be indicative of high correlation between electrons in neighboring layers. In the $\nu_T = 1$ regime, there should be an equal population of electrons and holes in the two layers. In the completely uncorrelated case, an electron attempting to make the jump between the two wells has a high chance of being blocked by the presence of another electron. In a strongly correlated system where electrons in one layer are perfectly lined up with holes in the other layer (and vice-versa), the conditions are far more favorable to tunneling.

Another interesting feature of this system is a dramatic drop in the counterflow resistivity in the same regime as the resonant tunneling effect (low temperature, $\nu_T = 1$). The counterflow configuration is when the current in one layer is directed opposite to the flow of current in the other layer. In the exciton picture, this corresponds to a current of excitons; electrons flowing in one layer are bound to holes flowing in the opposite layer, which corresponds to equal and opposite current flow within the two wells. One counterflow method is to flow current through one well, pass it through a shunt resistor, and re-direct it (in the opposite direction) through the other well; this method is typically called either series or shunt counterflow [125]. Measurements by Kellogg et al. [127], reveal a drop in the longitudinal and Hall resistivity in the counterflow configuration below 500 mK and at $\nu_T = 1$. Around the same time, similar results were published for a similar system by Tutuc et al. [128]. In both cases, the parallel current resistivity also drops drastically with temperature, while the direct Hall resistivity does not change (as expected from the quantum Hall effect) [127].

Another variation on the counterflow configuration is a counterflow drag experiment, where current is passed across one well in a closed circuit; a sensing resistor is then placed in parallel with the other well and is used to measure the induced current. If there is significant drag between the two layers, the current passing through the top well will induce an opposite current in the opposite well. In a population of excitons, this would correspond to inducing a current of holes in one well by pushing their corresponding electrons (or vice versa). In a paper by Nandi et al., "perfect" Coulomb drag is reported in a bilayer system near $\nu_T = 1$; i.e., the ratio of the induced current to the drive current was measured to be nearly unity (at T = 17 mK, $d/\ell = 1.5$, and near zero DC bias) [129]. An earlier work by Morath et al. [130]

report similar measurements in the uEHBL system discussed earlier in this section; in this paper, a fit to the drag resistance versus temperature closely matches a theoretical model by B.Y.K. Hu [131] which assumes a superfluid transition. However, Hu's model predicts that the drag resistance should be sharply peaked when the electron and hole populations are balanced; instead, measurements by Morath and coworkers reveal an exponential increase in drag resistance when the electron density is decreased relative to the hole density [130].

Early analysis of these results suggested that they were a signature of Bose-Einstein condensation [132]. One criticism of this claim is that all effects described above - resonantly enhanced tunneling, decreased counterflow , and strong drag effects - could be signatures of electron-hole pairing, rather than condensation. After exciton formation, there will be strong spatial correlation between electrons and holes in the neighboring layers; one would expect that the tunneling rate would jump, simply because of the heigtened probability of an electon in one well being adjacent to a hole in the other well.

A defense against this criticism is that pairing should only increase the tunneling rate by roughly a factor of two. If the motion of an electron is completely uncorrelated to the presence of an electron-or-hole in the half-filled neighboring well, one would expect that it has equal probability of being adjacent to an electron or hole. If instead it is perfectly bound to a hole, that probability is raised from 50% to near 100%. However, one must pay attention to the fact that differential resistance is typically being measured. In a direct measurement of the current in [123], the actual current peak near zero bias is less than double the tunneling current observed in the "incoherent" regime, although it is very narrow.

It may turn out that it is difficult to distinguish between pairing and condensation in this system. The reported effects tend to appear at very low temperatures, typically in the 100 mK range. Due to the large barrier typically used - typically 10-20 nm with 20 nm wells - the binding energy between interlayer electrons and hole may be very small. In the CQW system described in earlier chapters, where the electron-hole separation, is around 10-20 nm total (4 nm barriers with 14 nm wells, will give an average e-h separation around 20 nm), with - based on the result in Figure 5 - an expected binding energy of around 3 meV (35 K). If pairing only occurs below 150 mK (as shown in [123], in a system with a 10 nm barrier), this would correspond to a binding energy of around 12 μeV. It is also unclear whether in

this density regime Coulomb screening significantly lowers the expected binding energy of pairing.

In BCS superconductors, the binding energy for Cooper pairs tends to be higher than the thermal energy associated with the "condensation" threshold, which means that as soon as Cooper pairs form, they will immediately condense into a coherent state; it is not entirely clear whether the dramatic effects observed in this system, while clearly indicative of enhanced electron-hole correlation, are also indicating the appearance of a coherent state of excitons [133].

4.2 FABRICATION

The desired structure differs from previous systems described in Section 4.1 in a number of ways. In these systems, a balanced population of electrons and holes are generated in the system, either by applying a large magnetic field and tuning the filling fraction or through a complicated bias configuration in a self-aligned structure. The goal here is to enable transport measurements in a system where a balanced population of electrons and holes can be generated optically. First, it is necessary to use a structure with a small barrier width; the large barrier width used by other groups essentially eliminates tunneling current between the wells. However, in order to optically generate indirect excitons, it is necessary to either generate direct excitons and let them tunnel to form IXs or optically excite indirect excitons directly, both require some coupling across the barrier.

It is also desireable to have a thicker sample, with the eventual goal of performing transport measurements on a strain-trapped population of indirect excitons. While thin samples are more susceptible to stress, they are also more fragile. This is a significant risk with samples that require time-intensive processing. A sample thickness of 100 μm is far easier to work with than a 50 μm sample. This also would lower the bias voltage necessary for cutoff behavior.

The wafer this structure is fabricated from is similar to that described in previous chapters; the coupled quantum well structure is composed of 14 nm quantum wells with a 4 nm

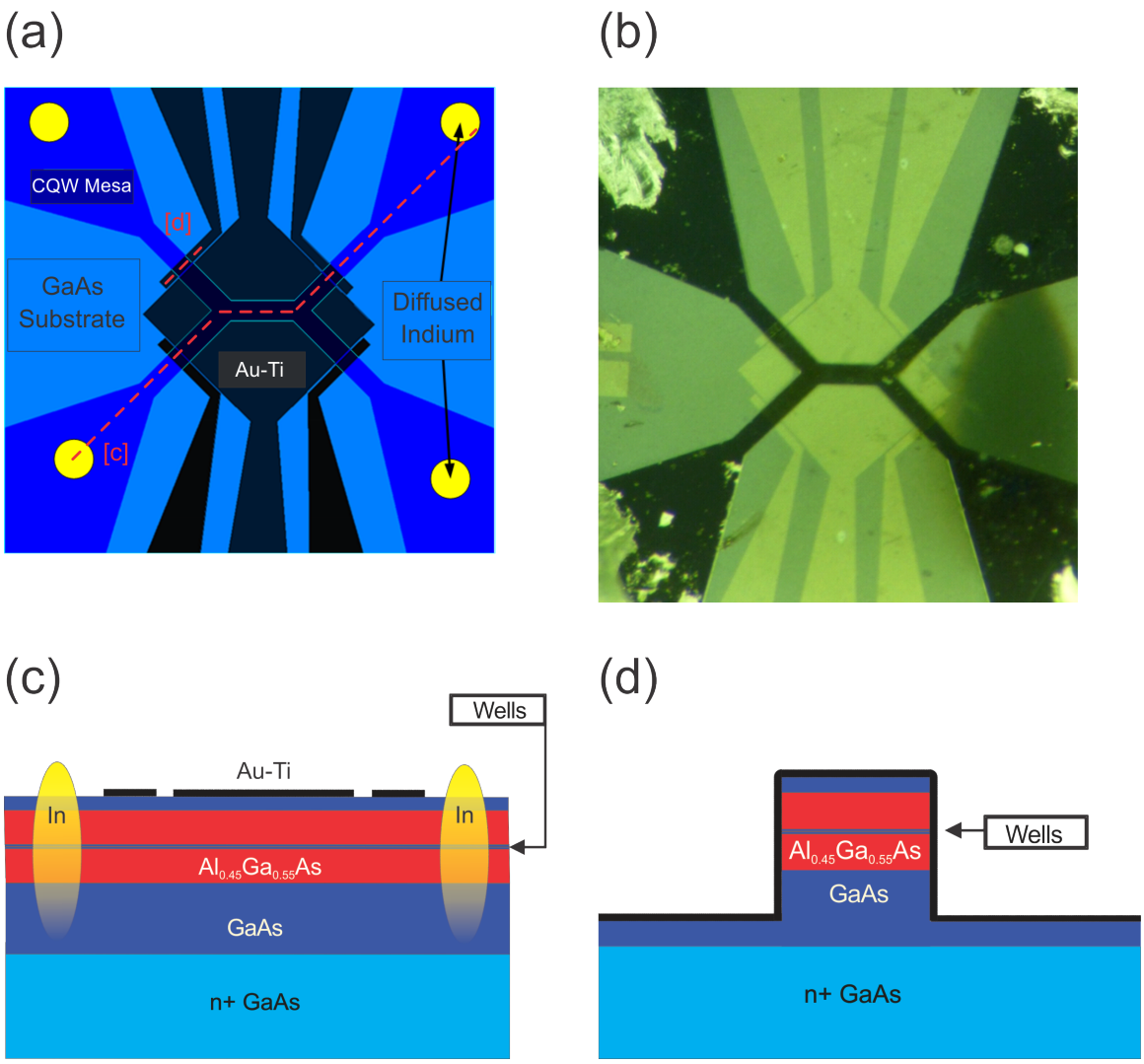

Figure 30: (a) An illustration of the sample design. The black layer represents the thin / optically transparent top contact, the dark blue region represents the unetched mesa and the lighter blue represents the etched region. (b) An image of an actual sample under a microscope. (c) and (d) show cross-sections along the respective paths shown in part (a).

barrier in a GaAs/$Al_{0.45}Ga_{0.55}As$ system. For simplicity, the superlattice was replaced with $Al_{0.45}Ga_{0.55}As$ (compare Figure 7 in Chapter 1 with the structure shown in Figure 30(c)).

The desired sample has several basic features. First, the flow of indirect excitons needs to be able to be cut off with an applied bias. To do this, they must be constricted to flow within a channel. As indirect excitons are restricted to the coupled quantum wells, channels can be fabricated by etching away the coupled quantum well region. This region is labeled as the "CQW mesa" in Figure 30(a) and is shown in cross-section in Figure 30(d). The channel width is designed to be 100 μm.

Second, to establish a population of indirect excitons with tunable lifetime, it must be possible to apply a DC bias to the central region. To achieve this, a Au-Ti contact is deposited over this area (the large black box with two contacts coming in from the top and bottom, in Figure 30(a)). Likewise, it is necessary to put a bias contact over each channel, so that it can be independently biased at high or low voltage compared to the central bias. These are the four other black contacts shown in Figure 30(a). The width of the bias contact arms across each channel is 50 μm, with a 5-10 μm gap between the arms and the central contact (the structure shown in Figure 30 has a 10 μm gap). The central contact must be somewhat transparent, so that light can be injected into the central region.

A sketch of the cutoff behavior is shown in Figure 31 for free carriers and in Figure 32 for indirect excitons. The cutoff arm is designed to form a barrier or a trap for electrons or holes, depending on the relative bias voltages in the central bias region and under the arm contacts. It is expected that the trap configuration will not dramatically impede the motion of carriers; in steady-state, the net number of carriers falling into the trap must equal the population leaving the trap on the other side.

The response of indirect excitons to the cutoff bias is a little different; indirect excitons will always be trapped under the highest voltage contacts, because indirect excitons experience the lowest energy in regions of highest electric field in the growth direction. The indirect exciton energy barrier height (or trap depth), as shown in Figure 32, is proportional to the change in the electric field in the growth direction and the electric dipole moment of

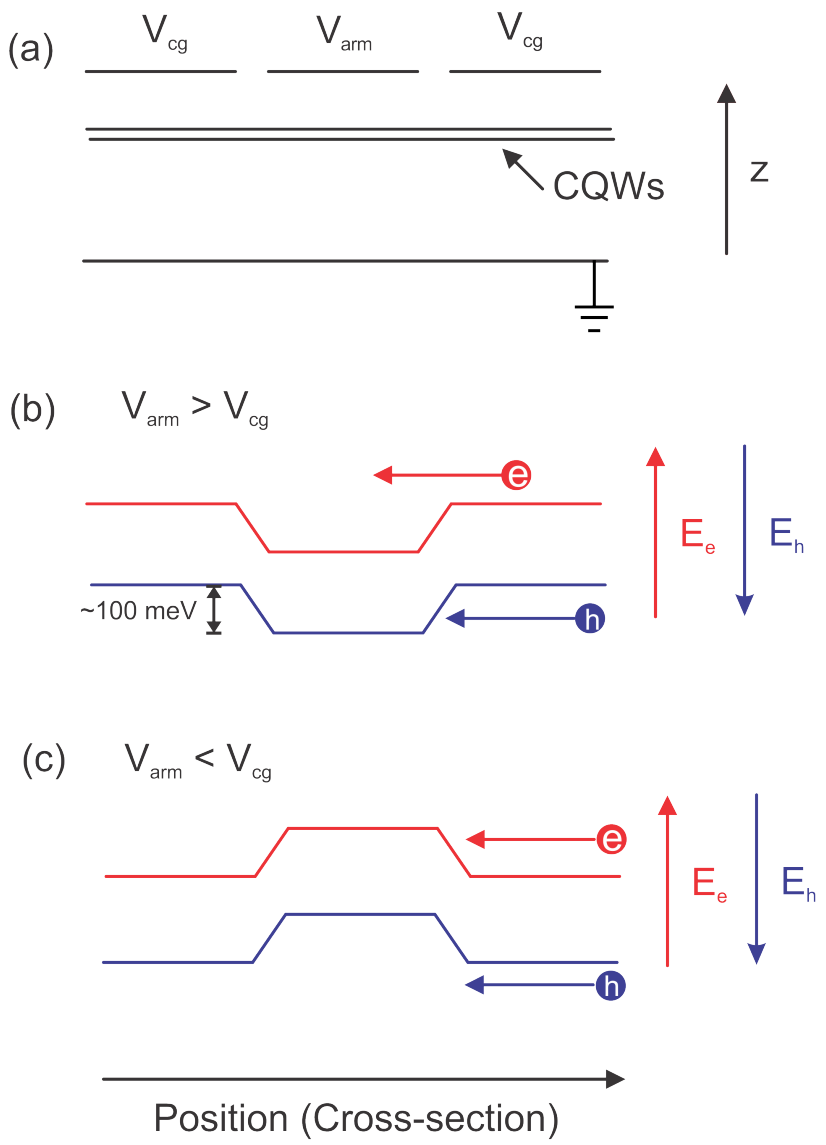

Figure 31: A sketch of the expected cutoff behavior, dependent on the cutoff arm voltage V_{arm} and the central bias voltage V_{cg} applied to the central contact and the diffused contact. Real-space cross section of sample shown in (a), energy diagrams in (b) and (c). In the regime where the arm voltage is greater than the central bias voltage (b), the cutoff arm acts as a barrier for hole transport. In the opposite regime (c), the cutoff arm acts as a barrier for electron transport. Barrier heights will be proportional to the voltage difference and are expected to be on the order of 100 meV.

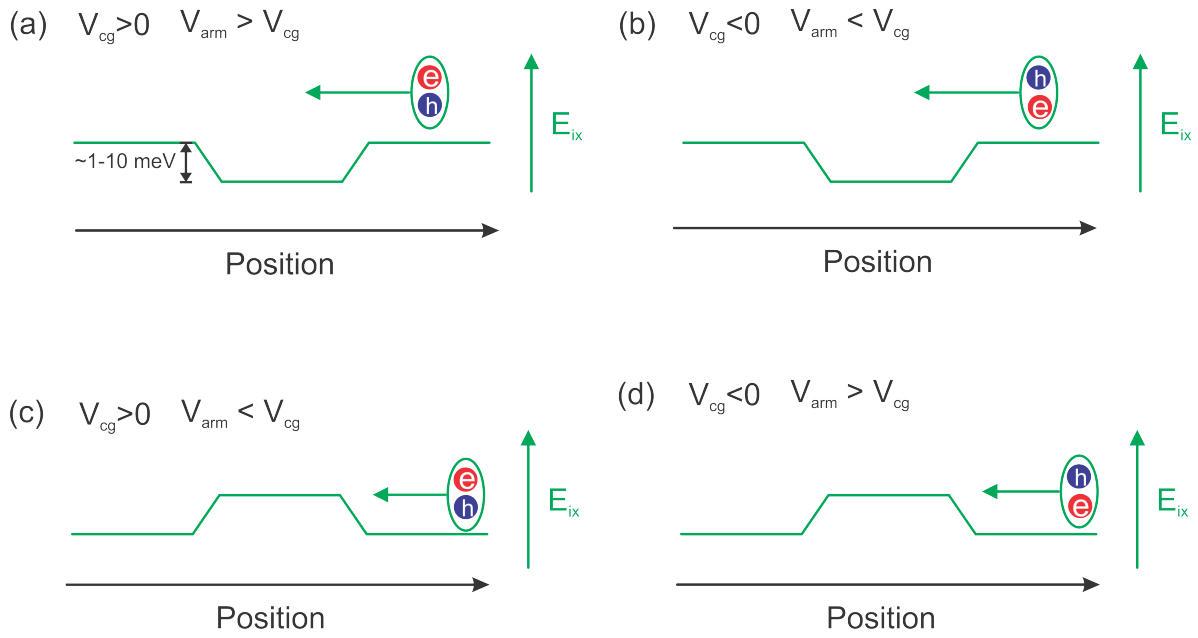

Figure 32: A sketch of the behavior of indirect excitons in response to the cutoff arm voltage V_{arm} and the central bias voltage V_{cg}, based on geometry in Figure 31(a). Indirect exciton energy is proportional to the field (barrier height is discussed in Section 4.2, will be roughly 1-10 meV for votlages used). When the magnitude of the arm voltage is higher than that of the central bias voltage, as in (a) and (b), indirect excitons will see a trap at the arm contact. When the magnitude of the arm voltage is lower than that of the central bias voltage, as in (c) and (d), indirect excitons will see a barrier at the arm contact. The direction of the bias voltage determines the orientation of the electron and hole in the coupled quantum wells. For simplicity, the charge polarization of the indirect excitons are assumed to be the same in the two regions.

the indirect exciton,

$$\Delta E_{IX} = \mu \frac{\Delta V}{\Delta z} \tag{4.1}$$

where a typical dipole moment is given by the electron charge multiplied by 20 nm and Δz (the thickness of the insulating layer) is around 1 μm. This gives an expected barrier height of 2 meV for every 100 mV offset between the cutoff arm and the central bias. Recall that indirect excitons do not directly move in the response to in-plane field, so any observed current will ultimately be due to the presence of free carriers entering or leaving the arm bias regions. However, in steady state the population of indirect excitons is in equilibrium with the population of free carriers at the edges of the contacts, so it is expected that the motion of free carriers can still be used to probe the population of indirect excitons.

Third, it must be possible to inject current into the wells. Diffused indium contacts are shown in yellow on the CQW mesa contact pads in Figure 30(a). These contacts extend into the structure and provide a path for current injection directly into both wells. Alternatively, indium alloys, such as InSn or InZn, can be used as n-type or p-type contacts, respectively (see discussion in Section 4.2.2); to avoid shorts to the n-type substrate, InZn was used for our samples.

4.2.1 Lithography and Etching

The fabrication of the structure in Figure 30(a) requires two lithography steps; one to establish the mesa structure and one to define the contact geometry. Both photolithography steps described below were performed using AZ 5214 E Image Reversal Photoresist. For these two steps, both positive and negative photoresist is necessary; image reversal photoresist can be used as either with essentially the same process, making it a convenient choice.

This type of photoresist is initially insoluble in its respective developer solution (AZ 300 MIF). After exposure to UV light, the exposed region becomes soluble. At this point, the sample could be developed and the photoresist would act as positive resist (the exposed region would be removed). However, if the sample temperature is elevated a second reaction occurs in the resist, causing the exposed region to become permanently insoluble to the

developer solution. The entire sample can then be flood exposed with UV light, which causes all photoresist not exposed during the first run to become soluble. Thus, everything exposed during the first step would act as negative resist (everything outside the initially exposed region would be removed).

The image reversal heat treatment is very sensitive to temperature and bake time. A reversal bake of 120 ° C for 90 seconds on a hot plate worked well. It is critical that the hot plate is properly calibrated and the temperature is reliable.

The first step in the fabrication process is establishing the mesa structure. This creates a microscale channel (channel thickness approximately 100 μm) in which the excitons are confined. This is achieved through a simple lithography process; an unprocessed sample is coated with photoresist and exposed in a manner that ensures that only the photoresist covering the mesa region is insoluble in a particular developer solution. After rinsing the sample in developer, the photoresist in the mesa region remains. The photoresist used does not react to the etchant solution, and thus provides a barrier for wet etching.

Typically, all wet etching methods for GaAs include two steps - oxidation of the top surface and removal of that oxide [134]. For the stress trapping experiments discussed in Chapters 2 and 3, it is necessary to simply thin samples in a uniform fashion. A simple method for doing so is through polishing the sample with a solution of bromine and methanol (between 1:10 to 1:20 dilution). In this solution, bromine acts as a strong oxidizer and the methanol is an inactive diluting agent. The removal of the oxide layer is achieved by mechanically polishing the sample.

This solution is inappropriate for patterning / selective etching; without the polishing step, the oxide layer is not removed efficiently, leading to extremely uneven etch rates across the sample. For the purposes of patterning, a 1:1:10 solution of phosphoric acid, hydrogen peroxide, and DI water were used. In this case, the hydrogen peroxide acts as the oxidizing agent and the phosphoric acid dissolves the oxide once it is formed [134].

It is important for the etch step to penetrate the quantum wells, but not to reach the substrate (see Figure 30 (d)). If the Au-Ti bias contact is deposited directly to the n+ GaAs substrate, it forms a relatively good contact - essentially shorting the bias contacts to the substrate. For most of the samples discussed here, the insulating region of the sample is

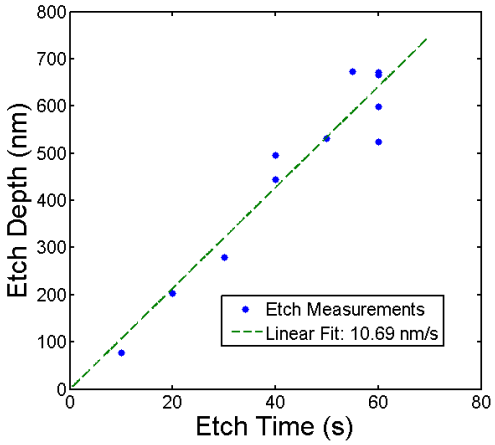

Figure 33: Plot of etch depth as a function of time for GaAs/$Al_{0.45}Ga_{0.55}As$ structure shown in Figure 30. Etching process uses 1:1:10 solution of phosphoric acid, hydrogen peroxide, and DI water near room temperature (around 20° C). Solution is gently stirred during etch process.

around 1 μm thick.

To avoid overetching it is necessary to have a good calibration of the etch rate. This calibration was performed by taking six small test chips and partially covering them with glyptol (red enamel paint). Each sample was then immersed in the aforementioned phosphoric acid solution for time intervals ranging from 10 s to 60 s. The glyptol acts as an etch barrier, producing a step between the etched and unetched regions. The glyptol is then removed with acetone and the step height is measured at several different points along each sample using a surface profiler. A plot of depth versus etch time is shown in Figure 33. Subsequent etches with the shown sample have been consistent with the fitted etch rate of 10.7 nm/s $\pm$ 0.81 nm/s. Variation in the etch rate can be reduced through more careful calibration of the concentration; however, this level of variability is adequate for ensuring that the etch does not proceed into the doped substrate.

In general, dry etch techniques - specifically reactive ion etching (RIE) - are preferable due to a higher degree of directionality. Wet etch techniques tend to be mostly isotropic;

as the solution etches down into the sample, it also etches sideways into the region covered by photoresist, a process called undercutting. With RIE, it is possible to etch straight down, producing much straighter sidewalls. Undercutting is problematic if the feature size is comparable to the etch depth; with this structure, the feature size (100 μm) is much larger than the etch depth (less than 1 μm), so a wet etch is possible. This can be desireable, as wet etching is cheaper and more convenient; RIE systems typically involve strongly reactive gases and are more often designed for silicon etching than GaAs [2].

4.2.2 Contacts

Metal-semiconductor contacts fall under two classifications: Ohmic contacts and rectifying, or Schottky, contacts. An Ohmic contact is characterized by a linear voltage drop across the contact as a function of voltage. Schottky contacts are characterized by a potential barrier at the semiconductor-metal interface and typically exhibit an exponential I-V curve at low voltage.

According to the early Schottky model of rectifying contacts, the height of the potential barrier is determined by the work function of the metal, that of the semiconductor, and the position of the semiconductor Fermi level within the bandgap. If the work function of the metal is higher than that of the semiconductor, the interface can lower energy by transferring charge from the semiconductor to the metal. This results in the distortion of the valence and conduction bands until the Fermi levels line up in equilibrium. In general, this will result in a barrier for the injection of electrons (or holes).

There are primarily two mechanisms for the transfer of charge across a Schottky barrier. For a population of carriers at finite temperature, some fraction will have enough thermal energy to hop over the barrier. This process is called thermionic emission, the current from which is determined by the barrier height ϕ_B and the temperature [135]:

$$I(V) \propto T^2 \exp\left(-\frac{q\phi_B}{k_B T}\right)\left[\exp\left(\frac{qV}{k_B T}\right) - 1\right]. \tag{4.2}$$

This expression assumes that the barrier height is large compared to the temperature. Al-

[2] Silicon RIE typically involves fluorine-based chemistry, while GaAs requires chlorine-based gas mixtures [134].

ternatively, if the barrier is thin enough, there is a non-negligible probability of the carriers tunneling through it. This process is typically called field emission. It is strongly dependent upon the width of the barrier (called the depletion region) is determined by the doping concentration of the semiconductor [135].

Early on, it was apparent that the Schottky model did not accurately predict the Schottky barrier height observed experimentally [136]. It was found that the height of the potential barrier at a metal-semiconductor interface is relatively insensitive to the work function of the metal, a phenomenon called Fermi level pinning. It was later realized that the surface states of the semiconductor are the primary factor in determining the barrier. Beyond this, the specifics can be quite complex and can depend strongly on surface treatment and quality, making the barrier height somewhat difficult to predict [137].

Typically, there are two strategies for producing an Ohmic contact to GaAs. The first is to reduce the height of the barrier. Due to Fermi level pinning, this is not particularly easy. Furthermore, thermionic emission drops off exponentially at low temperature. At $T = 4$ K, the thermal energy $k_B T$ is 0.34 meV. At this temperature, a barrier of even one percent of the GaAs band gap (1% of 1.43 eV, or 14 meV), is a substantial barrier. Alternatively, by increasing the doping concentration of the semiconductor at the interface, the thickness of the depletion region can be reduced, which can drastically lower the resistance due to improved tunneling current [134].

In practice, Ohmic contacts to GaAs involve some method for alloying GaAs to produce an intermediate, low-bandgap layer. Usually, one component of the contact alloy acts as a p-type or n-type dopant for GaAs. One common example is Au/Ge/Ni - where Ge can act as a p or n-type dopant for GaAs, depending on preparation [134].

The method of Ohmic contact that we use for injection into the quantum wells is a simple diffused indium contact. Based on a model by Sebestyen [138] and Auger electron spectroscopy measurements by Lakhani [139], the indium diffuses into the GaAs crystal, with indium density varying with distance into the sample. Close to the contact will be a primarily InAs layer. Deeper, there will be a layer of $\mathrm{In}_{y(x)}\mathrm{Ga}_{1-y(x)}\mathrm{As}$ alloy, where the alloy fraction $y(x)$ decreases as the distance from the contact x increases. This prevents the formation of a sharp barrier and provides an Ohmic contact. InZn alloy contacts have

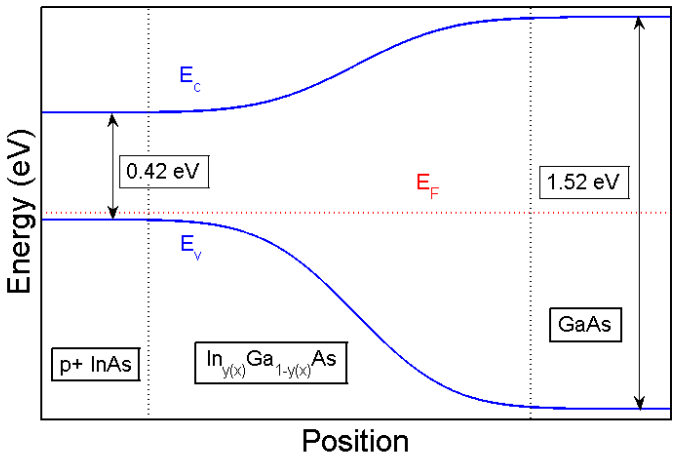

Figure 34: A sketch of the band diagram for a diffused indium contact with heavy zinc doping (p+). Low temperature band gaps for InAs (0.42 eV) and GaAs (1.52 eV) were used [1]. Solution to diffusion equation (error function) used to aproximate variation of band gap; a more rigorous profile can be calculated by following approach used by Sebestyen [138].

been reported to form Ohmic contact to p-type GaAs [140, 141] and InSn or pure indium [139] forms an Ohmic contact to n-type GaAs. For the purposes of these experiments, InZn contacts were used to avoid shorts between the diffused contacts and the n-type substrate. A sketch of the band diagram going from the InAs region to the GaAs is shown in Figure 34.

The bias contacts are not intended to inject current into the sample. In fact, current injection through the quantum wells results in heating, which is undesireable. The primary role of the bias contacts is to provide a constant electric field underneath the contact. So in this case the presence of a Schottky barrier is not an issue. For the bias contacts, a 10 nm layer of titanium was deposited onto the GaAs surface, followed by 60 nm of gold. The titanium layer prevents the diffusion of gold atoms into the gallium surface, while still allowing good adhesion between the gold and GaAs layers. For optical experiments, it is necessary to have some degree of optical transparency near 800 nm, hence the need for thin contacts. At 800 nm wavelength, the absorption from gold is the primary issue. Using the

extinction coefficients of gold [142] and titanium [143] at this wavelength , roughly 95% of the power is absorbed by a 10 nm Ti / 60 nm Au contact. Typical pump power for generating indirect excitons is on the order of 100 μW or less, so increasing the input power by a factor of 10-100 is not a major problem, other than the additional heating. However, it does make it difficult to perform time-gated experiments at late times after a pump pulse, where the photoluminescence tends to be dim.

4.3 CONDUCTIVITY MEASUREMENTS

The basic type of transport measurement employed here is the measurement of conductivity between the diffused contacts as a function of various bias and optical pumping conditions.

- To prove independent contact to individual quantum wells, it would be interesting to look for cutoff behavior as observed in [120]. In these experiments, it was possible to detect double-plateau behavior as the cutoff-arm bias voltage is increased. Due to the lack of an intrinsic electron population due to doping, this behavior may look different in our system.
- With a steady-state population of indirect excitons in the central region (due to optical pumping), it would be interesting to measure the conductivity as a function of density. Excitons should not inherently carry current, but the ionization of excitons near the edge of the bias contacts can generate current, potentially providing a tool for probing the IX population.
- The indirect exciton population is also dependent on the radiative lifetime, which is strongly dependent on the applied bias. The dependence of conductivity on the central bias would also be of interest.

In order to properly study the conductivity as a function of DC bias on the central and arm contacts, it is necessary to decouple the biasing voltage from the probe signal. One way to to do this is to apply a small AC signal on top of the DC voltage at the probe points and measure the resulting AC current. Effectively this gives a differential, small-signal measurement of

the conductivity around a particular DC bias. A common method of doing this type of measurement is to use a lock-in amplifier - an instrument designed to measure a small AC signal of a particular frequency from an input with a low signal-to-noise ratio.

The details of this measurement technique will be discussed in the following section.

4.3.1 Lock-in Amplifiers

A lock-in amplifier (LIA) is a device used to extract a small-AC signal of a particular frequency from a noisy background. Consider a signal sitting on top of large band-width noise:

$$v(t) = V_s \sin(\omega_0 t) + \int_{-\infty}^{\infty} V_{\text{noise}}(\omega) e^{\mathrm{i}\omega t} \mathrm{d}\omega. \tag{4.3}$$

A lock-in operates by multiplying the input signal by an internally or externally generated reference signal. The frequency of the reference is chosen such that it coincides with the signal being measured,

$$v_{\text{ref}}(t)v(t) = V_{\text{ref}} V_s \sin(\omega_0 t)\sin(\omega_0 t + \phi_{\text{ref}}) + \int_{0}^{\infty} V_{\text{ref}} V_{\text{noise}}(\omega)\sin(\omega_0 t + \phi_{\text{ref}}) e^{\mathrm{i}\omega t} \mathrm{d}\omega. \tag{4.4}$$

where ϕ_{ref} is the phase offset between the reference and the measured signal. The product of the signal and reference can be de-composed as follows:

$$\sin(\omega_0 t)\sin(\omega_0 t + \phi_{\text{ref}}) = \frac{1}{2}\left[\cos(\phi_{\text{ref}}) - \cos(2\omega_0 t + \phi_{\text{ref}})\right]. \tag{4.5}$$

It is easy to see that when the multiplied signal is passed through a low-pass filter with a cutoff frequency much less than ω_0,

$$\text{LPF}\left[v_{\text{ref}}(t)v(t)\right] = \frac{1}{2} V_{\text{ref}} V_s \cos(\phi_{\text{ref}}) \tag{4.6}$$

the first term is passed because it is DC (zero frequency). Thus, the output of the lock-in amplifier is a DC signal which is proportional to the amplitude of the component of the input at the reference frequency.

The second term in (4.6) is filtered out. For example, if a signal with frequency f_0 is

averaged for time T[3], the integrated $2\omega_0$ term will be multiplied by a pre-factor of $(2\omega_0 T)^{-1}$. For a $f_0 = 30$ Hz signal averaged over 1 s, this reduces the $2\omega_0$ term by a factor of about 380. This will appear as a small ripple on the DC output.

Likewise, the power associated with the noise is reduced in a similar fashion. Integrating the signal over time-scale T can be approximated as a low-pass filter with cutoff frequency $\frac{1}{T}$. For the case of of noise that is frequency-independent within a large bandwidth the RMS reduction is given by the following:

$$\sqrt{\frac{\langle v^2(t)\rangle_{Filtered}}{\langle v^2(t)\rangle}} = \sqrt{\frac{\int_0^{1/T} V(\omega)^2 \mathrm{d}\omega}{\int_0^{\omega_{BW}} V(\omega)^2 \mathrm{d}\omega}} \sim \frac{1}{\sqrt{\omega_{\mathrm{bandwidth}} T}}. \tag{4.7}$$

If the background noise is distributed over a band-width on the order of kHz, a one-second integration time could cut down the total power of the noise by a factor of 1000. More realistically, there will be sources of noise strongly peaked at particular frequencies; provided they are far from the reference frequency, they will be reduced even more strongly.

Ideally, the output of the LIA is a DC voltage, typically scaled so that the output is equal to the RMS voltage of the measured signal. Note that the input signal will not necessarily be in phase with the reference signal; typically, a LIA can output the RMS voltage of the component that is in-phase or the component that is 90° out of phase.

4.3.2 Measurement

With this sample geometry the primary goal was to be able to gate electrons and holes in either quantum well independently using the arm contacts.

The measurement setup, shown in Figure 35, was designed so that a small sensing resistance is used to measure the current going into the top-indium injection contact. For a small AC signal on top of a DC bias voltage, the current can be expanded around the bias voltage:

$$I\left(V_{DC} + v(t)\right) = I\left(V_{DC}\right) + \left(\frac{dI}{dV}\right)_{V=V_{DC}} V_s \sin(\omega t). \tag{4.8}$$

[3]Recall that an average over time T is essentially a low-pass filter with a characteristic cutoff frequency on the order of 1/T.

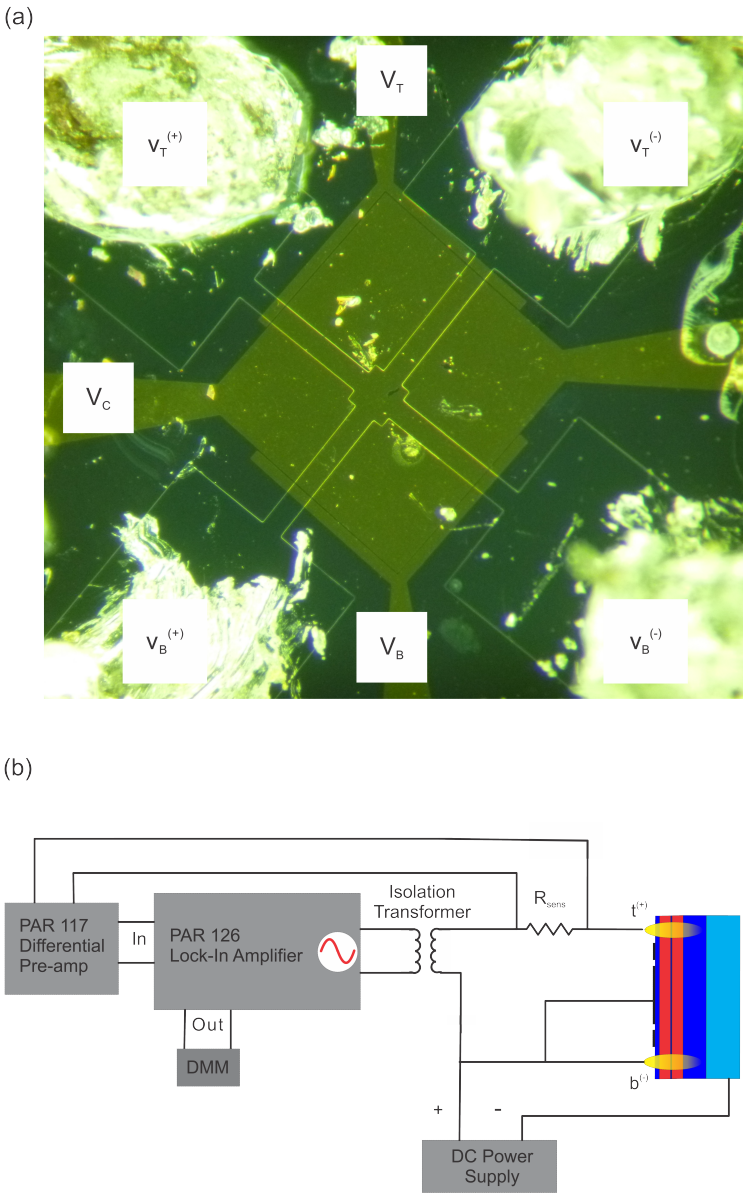

Figure 35: (a) A top-view of a typical cross-configuration sample with contacts labeled and (b) a diagram of the lock-in measurement setup. The central bias contact and two diffused contacts are biased at a fixed DV voltage with respect to the substrate. A small (10 mV RMS at 30 Hz) signal was applied across the diffused contacts ($V_t^{(+)}$ and $V_b^{(-)}$) and sensing resistor (980 Ω); the AC current was measured by detecting the voltage across the sensing resistor.

Provided the sensing resistance is small compared to the total resistance, the voltage measured by the LIA will be the small-signal AC current multiplied by the sensing resistance:

$$V_{\text{out}} = R_{\text{sens}} \left(\frac{dI}{dV} \right)_{V=V_{DC}} V_{s,\text{RMS}}. \tag{4.9}$$

In the following measurements, the system will occasionally in the regime where the small signal reistance is not much larger than the sensing resistance (typically a sensing resistance of approximately 1 kΩ was used). It is easy to correct for this by properly treating the system as a voltage divider. The choice of the sensing resistor is a trade-off; a small resistance will produce a small voltage, large resistors tend to exhibit higher thermal noise (due to the higher drive signal voltage necessary). Trial-and-error suggested that measurements below 0.1 mV tended be noisier and more prone to instability.

A sketch of the equivalent circuit diagram for these measurements is shown in Figure 36. This diagram will be discussed in more detail in Section 4.3.3.2 in the context of the experimental measurements.

4.3.3 Results

In the following sections, the results of transport measurements on the sample shown in Figure 35 are discussed. The AC small-signal conductance around each DC bias point was measured, as described in the previous section. Unless otherwise specified, the reference source was a 30 Hz signal with 10 mV peak-to-peak amplitude put out by the internal reference of the lock-in amplifier. A sensing resistance of around 1 kΩ was typically used to measure the injected current. The noise on the LIA input signal was reduced with variable cutoff high- and low-frequency rolloff filters, typically set to 3 Hz and 100 Hz. The output filter was typically set to a time-constant between 300 ms and 3 s, depending on the stability of the signal, with a 12 dB/octave rolloff rate.

All low temperature measurements were performed in a continuous flow cryostat with optical access. The sample was mounted on a piece of copper board with silver paste. The temperature sensor was mounted on the sample rod, less than 1 cm away from the sample,

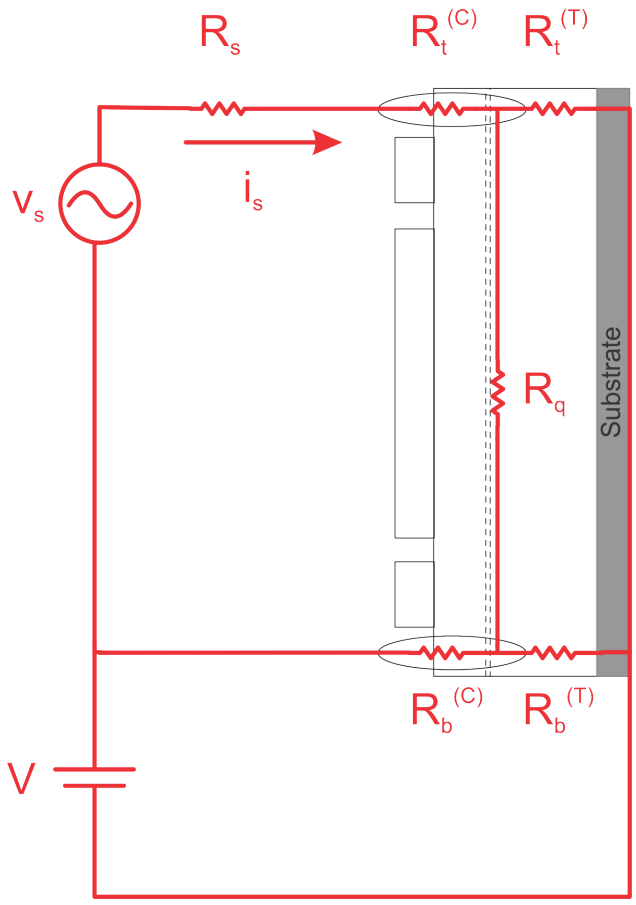

Figure 36: An equivalent circuit model of the measurement setup shown in Figure 35. Relevant parameters are the sensing resistor (R_s), the contact resistance of the top and bottom diffused contacts ($R_t^{(C)}$ and $R_b^{(C)}$), the tunneling resistance of the top and bottom difused contacts to the substrate ($R_t^{(T)}$ and $R_b^{(T)}$), and the resistance across the quantum wells (R_q). The small-signal AC source (v_s) and DC bias (V) are also shown.

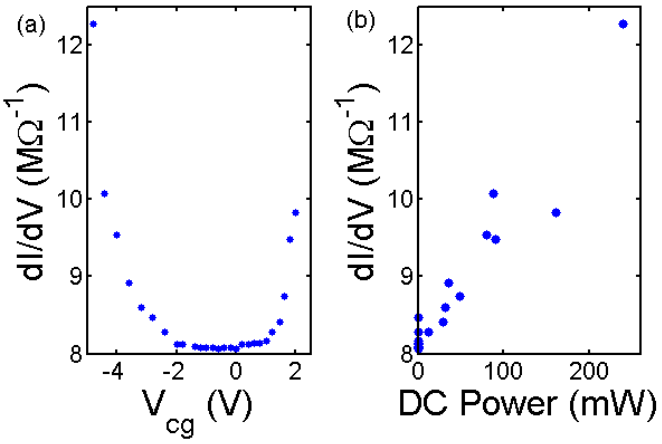

Figure 37: In (a), room temperature of dI/dV for overetched sample where there is low resistance (on the order of 100 Ω) between the bias contacts and the substrate, leading to significant leakage current. Increase in conductivity with bias likely due to heating, as suggested by plot of DC power through bias contacts, shown in (b).

but not in direct thermal contact with it. As such, the temperature reading is indicative of the ambient bath temperature, but heating due to current may make the sample somewhat hotter. With the exception of the "over-etched" sample mentioned in Section 4.3.3.1, the current injected into the sample through the DC contacts was relatively small, typically less than 50 μA. With bias voltages less than 1 V, this would correspond to heating of less than 100 μW. This is very likely to be much smaller than the heating due to optical pumping. This current restriction limited the bias ranges possible, but was necessary to avoid heating or damaging the sample.

4.3.3.1 Over-etched Samples Preliminary measurements were done on an early batch of samples with a thinner GaAs buffer layer, which resulted in undesirably high DC current between the bias contacts and the substrate. At room temperature, a typical differential conductance curve (between diffused contacts $V_t^{(+)}$ and $V_b^{(-)}$) with varying central bias voltage is shown in Figure 37(a), showing a relatively flat dependence at low voltage, followed by

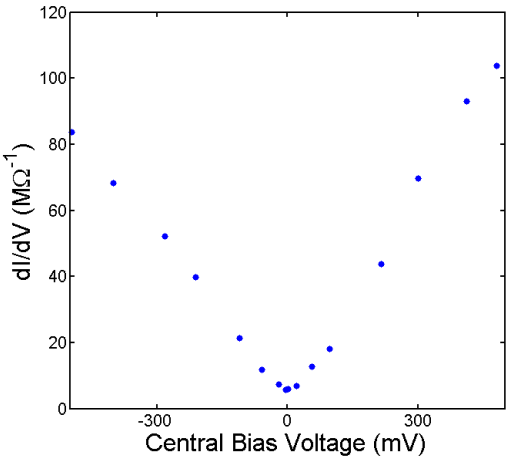

Figure 38: The small-signal AC conductance from $t^{(+)}$ to $b^{(-)}$ diffused contacts (see Figure 35) as a function of central bias voltage (V_{cg}) at low temperature (T = 4 K). Arm bias contacts are floating.

a gradual drop in resistance. Going far past this voltage range often resulted in irreversible damage to the contacts, characterized by shorts to the substrate.

Figure 37(b) shows that the drop in resistivity is strongly correlated with the DC electrical power dissipated by the sample through the bias contacts, suggesting that this effect was primarily caused by heating. These measurements were also performed with the diffused indium contacts floating with respect to the DC bias, suggesting there was likely also a large barrier to transport. This may be why the conductance is relatively flat at low bias voltages, compared to subsequent measurements.

New samples were prepared with a thicker buffer layer, preventing the etching process from uncovering the substrate and drastically reducing the leakage current between the bias contacts and the substrate. The thicker buffer layer samples are used for all other measurements in Section 4.3.3.2 and after.

4.3.3.2 Applied Central Bias To study the effect of the central bias contact on transport across the sample at low temperature, the small-signal AC conductance was measured,

as described in Sections 4.3.3 and 4.3.2. Conductance was measured between the diffused indium contacts labeled $t^{(+)}$ and $b^{(-)}$ (shown in Figure 35(b)), as a function of the DC voltage applied to the central bias contact with respect to ground (V_{cg}). The DC voltage at the indium contacts were also set to the central bias voltage (to minimize any voltage barrier at the edge of the central bias contact) and the arm bias contacts were left floating. The measurement was performed at 4 K.

It can be seen from the results of this measurement, in Figure 38, that the conductance is smallest at zero bias, and increases as the absolute value of the central bias increases. The conductance seems to be almost symmetric with respect to zero bias, but increases somewhat more rapidly at positive bias.

The transport path of interest is the one that goes straight through the coupled quantum wells; but it also possible for current to flow from the diffused contact and directly into the doped substrate. Ideally, the conductance of interest - that associated with the quantum wells - is much larger than that associated with leakage into the substrate. To determine the size of this effect, the DC I-V curve was measured between each of the diffused contacts and the grounded substrate. The I-V curve was used to approximate the differential conductance as a function of central bias voltage. This measurement was performed at room temperature, and is shown in Figure 39.

The conductance curve of the two diffused contacts, as well as the central bias contact, match the behavior of the small-signal conductance across the sample measured in Figure 38. This measurement was performed at high temperature for simplicity (to isolate the leakage current measurement from low temperature effects), but to provide a fair point of comparison, a plot of the temperature dependence of the conductance at a fixed central bias voltage (V_{cg} = 145 mV) is shown in Figure 40. It can be seen that the measured conductance at room temperature is comparable to the tunneling conductance between the diffused contacts and the substrate (roughly on the order of 100 $M\Omega^{-1}$).

This result suggests that the primary cause of the increase in conductance with bias voltage, shown in Figure 38, is due to increased carrier flow into the substrate from the diffused contacts. The significant drop in conductance as a function of temperature is likely also caused by the decreased population of thermally excited carriers and the thermal hopping

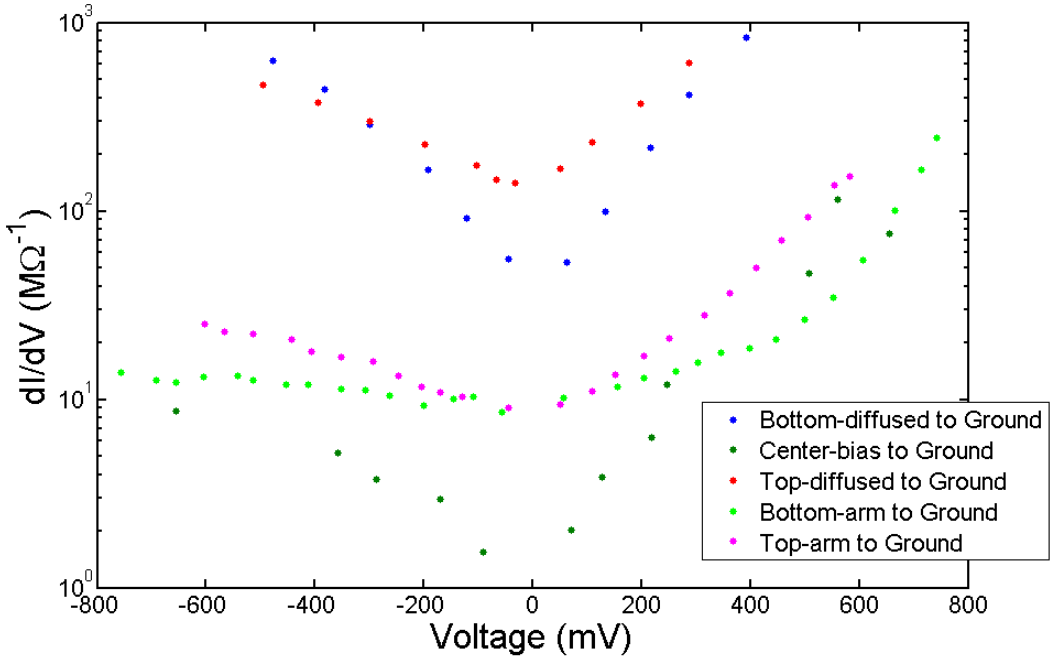

Figure 39: A plot of the differential DC conductance from ground to the top diffused contact, to the bottom diffused contact, to the central bias contact, to the top arm contact, and the bottom arm contact (as labeled in Figure 35(b)) as a function of the DC applied voltage between that contact and ground. Measurement performed at room temperature.

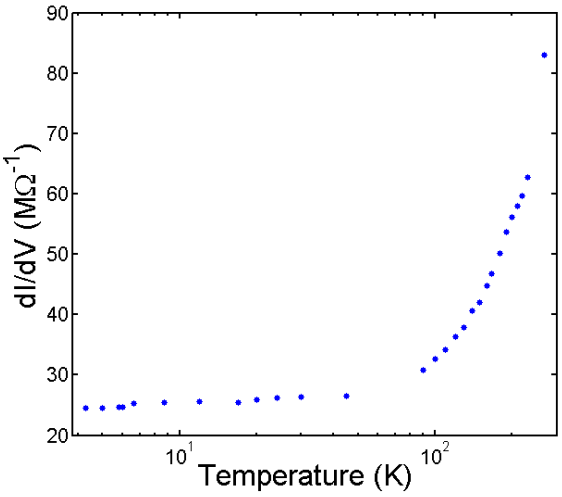

Figure 40: A plot of the small signal AC conductance with a fixed central bias voltage ($V_{\rm cg}$ = 145 mV) and floating arm bias contacts as a function of temperature.

of carriers over the energy barrier between the diffused contacts and the substrate.

To gain a better understanding of the effect of tunneling current, a simple equivalent circuit model of the measurement setup is shown in Figure 36. Based on the measurement from Figure 39, the resistance from the evaporated bias contacts to the quantum well and the substrate are ignored (assumed to be infinite). The sensing resistor is chosen so that it is small compared to the equivalent resistance of the sample and is used to measure the current injected into the sample (i_s). In the approximation where the sensing resistor can be ignored, the equivalent differential resistance of the sample is given by:

$$\frac{\partial v_s}{\partial i_s} = R_t^{(C)} + \frac{R_b^{(T)} + (R_b^{(C)} + R_b^{(T)})\frac{R_q}{R_b^{(C)}}}{\left(\frac{R_q + R_t^{(t)}}{R_t^{(T)}}\right)\left(\frac{R_b^{(T)} + R_b^{(C)}}{R_b^{(C)}}\right) + \frac{R_b^{(T)}}{R_t^{(T)}}} \tag{4.10}$$

The parameters in this expression are as labeled in Figure 36. It is expected that the contact resistance should be significantly less than the tunneling resistance; even if there is a barrier associated with injection of current from the indium contacts into the quantum wells (the contact resistance), it should be significantly less than the barrier associated with injection of

current into the substrate. In this approximation ($R_b^{(C)}, R_t^{(C)} \to 0$), the equivalent resistance is given by a much simpler expression:

$$\frac{\partial v_s}{\partial i_s} = \frac{R_t^{(T)} R_q}{R_q + R_t^{(T)}} \tag{4.11}$$

or, alternatively, in terms of the conductance:

$$\frac{\partial i_s}{\partial v_s} = \frac{1}{R_t^{(T)}} + \frac{1}{R_q} \tag{4.12}$$

While tunneling into the substrate is not ideal, it is not necessarily a major issue. Primarily, the goal is to look for cutoff behavior associated with variation of the arm bias contacts with respect to the overall, central bias. The evaporated contacts are also not significantly coupled to the substrate, as shown in the plot of the DC conductance between ground and the top arm, bottom arm and central bias contacts in Figure 39. At typical bias voltages of a few 100 mV, the conductance of the evaporated contacts are about one to two orders of magnitude lower than the diffused contacts. At a fixed central bias, it is expected that varying the arm bias voltages will not significantly effect the tunneling conductance to the substrate, but may change the conductance of the path through the quantum wells. Therefore any change in the equivalent conductance, as shown in (4.12), will be due to changes in the conductance of the path through the quantum wells.

4.3.3.3 Effect of Optical Pumping The effect of optical excitation on the conductance was measured by focusing a CW laser diode on the central mesa structure. The laser wavelength was tuned so that it was near resonant to the direct exciton line (between 800 nm and 805 nm). The small signal AC conductance was measured, in the same manner as discussed in previous sections, as a function of the laser pump power. To reduce the effects of heating, the laser was blocked after each measurement and the dark conductance was measured. In Figure 41, the conductance as a function of pump power is shown. For each data point, the result is normalized with respect to the dark value at that data point. This measurement was taken at fixed central bias voltage ($V_{\text{cg}} = 145$ mV) and temperature (5 K, with some instability over time within $\pm$ 1 K). The dark values were taken in a dimly lit

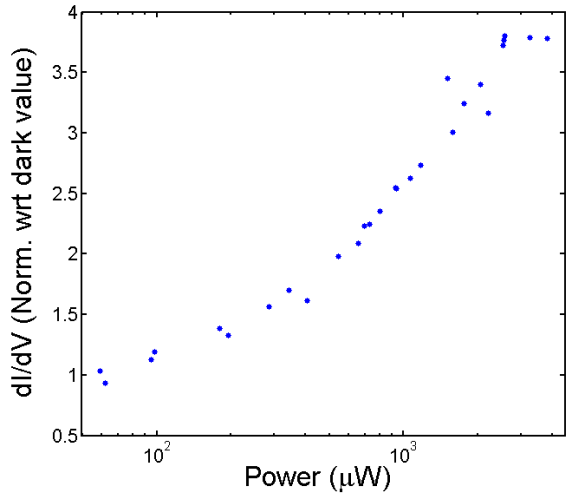

Figure 41: A plot of the small signal AC conductance with a fixed central bias voltage (V_{cg} = 145 mV) and floating arm bias contacts, as a function of optical pump power. Conductance is normalized with respect to dark value. Laser is focused on central mesa region, near resonant to direct line (λ between 800 nm and 805 nm). Temperature is fixed at 5 K $\pm$ 1 K.

room, with ambient light level significantly less than typical laser powers [4]

A clearer picture of the power dependence is seen by looking at the conductance versus central bias curve at several power values. A plot of the conductance as a function of V_{cg} is shown in Figure 42 at several different pump powers: 0 μW, 520 μW, 900 μW, 2000 μW, and 2900 μW. These curves are shown in Figure 42. It seems that the power dependence shown in Figure 41 is not due to an overall increase in the conductance, but rather due to a shifting of the conductance curve symmetry point. This likely results from the build-up of optically generated charge in the sample, causing a built-in field that increases with optical power. A positive built-in bias shifts the conductance minimum to lower applied bias (presumably, where $V_{built\text{-}in} + V_{applied} = 0$).

[4] A rough measurement of the ambient light levels were found by looking at the "dark" measurement of a silicon optical power meter head with an active area of ≈ 0.8 cm^2, calibrated to $\lambda = 800$ nm. In a dimly lit room, a power reading of ≈ 50 nW was observed; compared to ≤ 10 nW with all overhead lights off. Conductance variation between the dimly lit and entirely dark room was measureable, but was typically only a few percent.

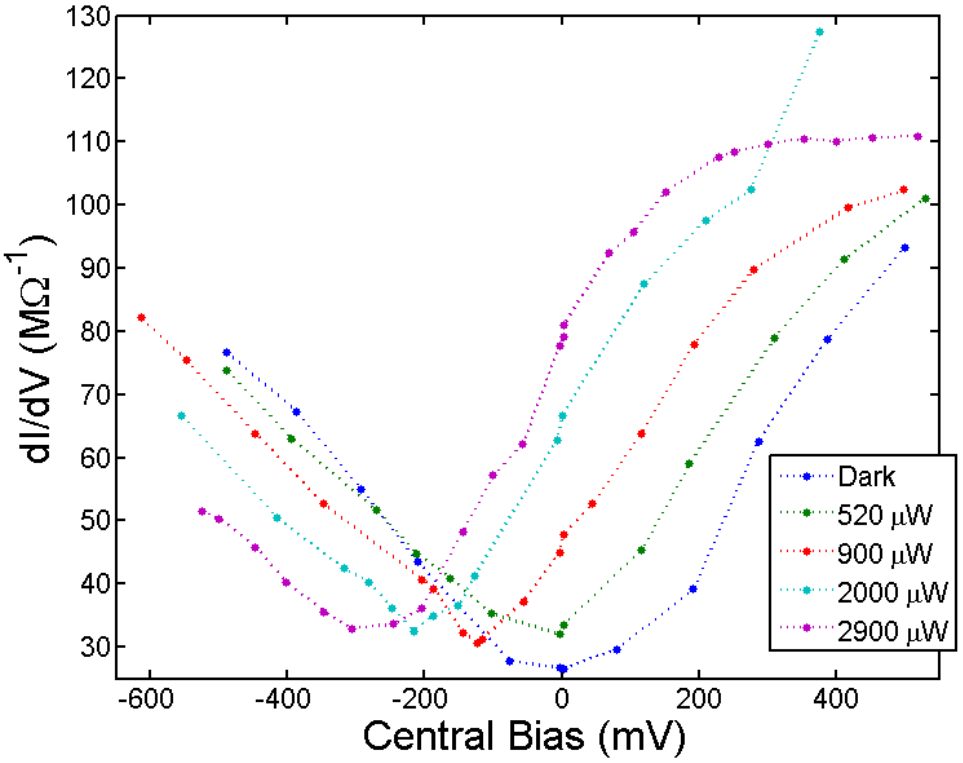

Figure 42: A plot of the small signal AC conductance as a function of central bias voltage (V_{cg}) and floating arm bias contacts, for varying values of optical pump power. Laser is focused on central mesa region, near resonant to direct line (λ between 800 nm and 805 nm). Temperature is fixed at 6.5 K $\pm$ 1 K.

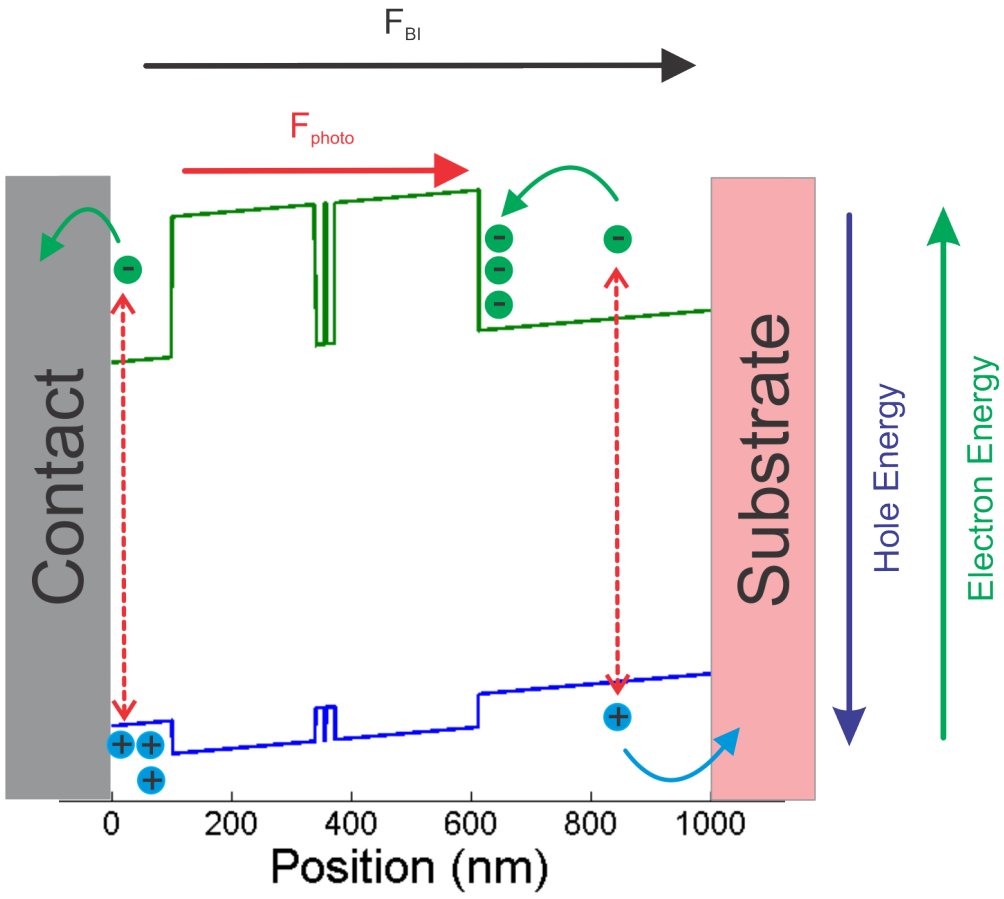

Figure 43: A to-scale plot of the band diagram along a cross section between the central bias contact and the substrate along the growth direction (for sample discussed in Sections 4.3.3.2 - 4.3.3.4. In the presence of a built-in electric field (F_{bi}) due to band bending, photogenerated carriers (indicated by dotted red line), will build up at the boudary of GaAs and AlGaAs layers, resulting in a photo-induced field (F_{photo}) in the quantum well region, pointed in the same direction as the built-in field.

The likely explanation for this behavior is illustrated in Figure 43. The sample under examination includes a 100 nm GaAs region directly under the metal contact and a 500 nm GaAs region directly on top of the doped substrate. Under illumination, electron-hole pairs will also be generated in this region. In the presence of a built-in field due to band bending, charge buildup will occur at the boundaries of the AlGaAs barriers, enhancing the built-in field across the AlGaAs barrier and the quantum wells. The observed behavior in Figure 42 is consistent with a positive built-in and photogenerated voltage from contact to substrate, as the flat-band peak seems to shift towards negative applied bias with increased power.

4.3.3.4 Cutoff-arm Behavior To look at the effect of the cutoff arm bias contacts, the small signal AC conductance is measured at fixed central bias. Ultimately, the goal is to use the cutoff arms to indepedently contact each quantum well, but for the purposes of testing, the top and bottom arms were tied together (such that $V_{\text{arm}} = V_{tg} = V_{bg}$). Ideally, this would allow the conducting path through the two wells to be entirely cut off in two steps, in a fashion similar to Eisenstein's work [120]. Under only ambient light in a dimly lit room, the dependence of the conductance on the arm voltage is measured at a fixed central bias value of 145 mV. This result is shown in the top plot of Figure 44. Unlike the central bias dependence shown in Section 4.3.3.2, this result is clearly asymmetric about zero bias. It also does not appear to be symmetric around the central bias voltage (145 mV).

The same measurement with optical excitation (at 1 mW and 3 mW power) are shown in the lower two plots of Figure 44. The same general trend persists, although there appears to be a relatively sharp step behavior that appears only under optical pumping. In the 1 mW case, the conductance seems to exhibit a 30 $\text{M}\Omega^{-1}$ step over 250 mV; in the 3 mW case, it is roughly a 20 $\text{M}\Omega^{-1}$ step over the same range. In the dark case, the change in the conductance over this range is only about 8 $\text{M}\Omega^{-1}$.

Taking into account the power dependence shown in Figure 42, the three plots shown in Figure 44 is not a fair comparison. At fixed applied central bias voltage, the effective bias changes with pump power. From Figure 44, it is impossible to tell whether the step-behavior is specifically due to carriers generated in the quantum wells or simply due to the shift in the bias voltage.

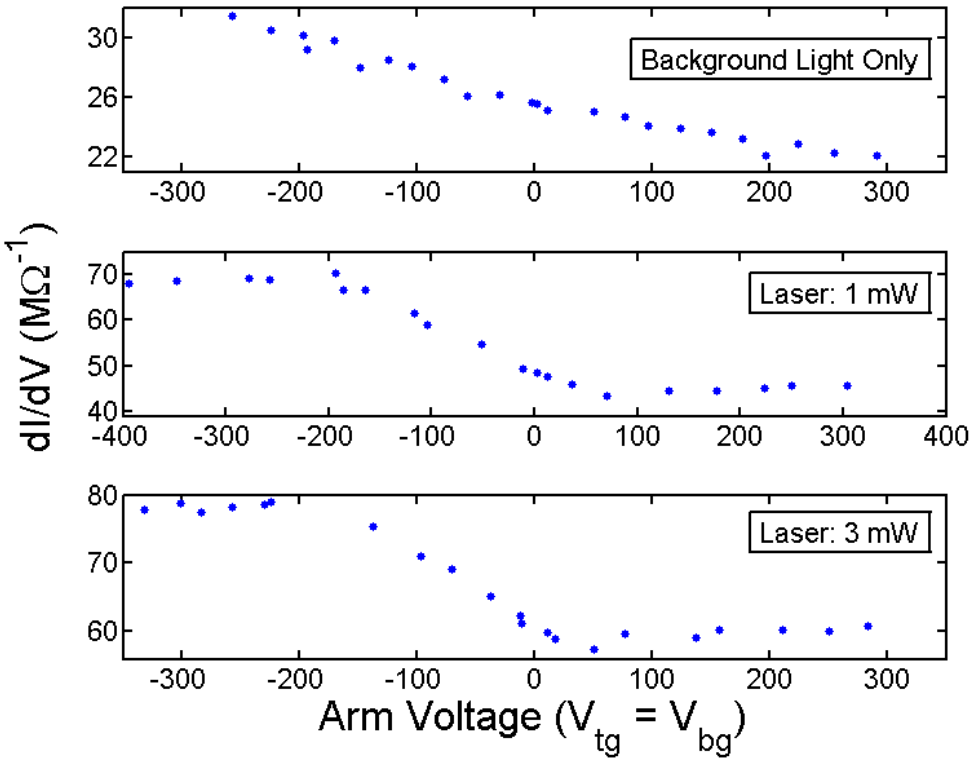

Figure 44: A plot of the small signal AC conductance at fixed central bias ($V_{\rm cg} = 145$ mV), as a function of arm bias voltage (top and bottom bias arms are tied together, $V_{\rm tg} = V_{\rm bg}$). Cases shown are for no pump laser (background light only), 1 mW optical power, and 3 mW optical power. Laser is focused on central mesa region, near resonant to direct line (λ between 800 nm and 805 nm). Temperature is fixed at 5 K $\pm$ 1 K.

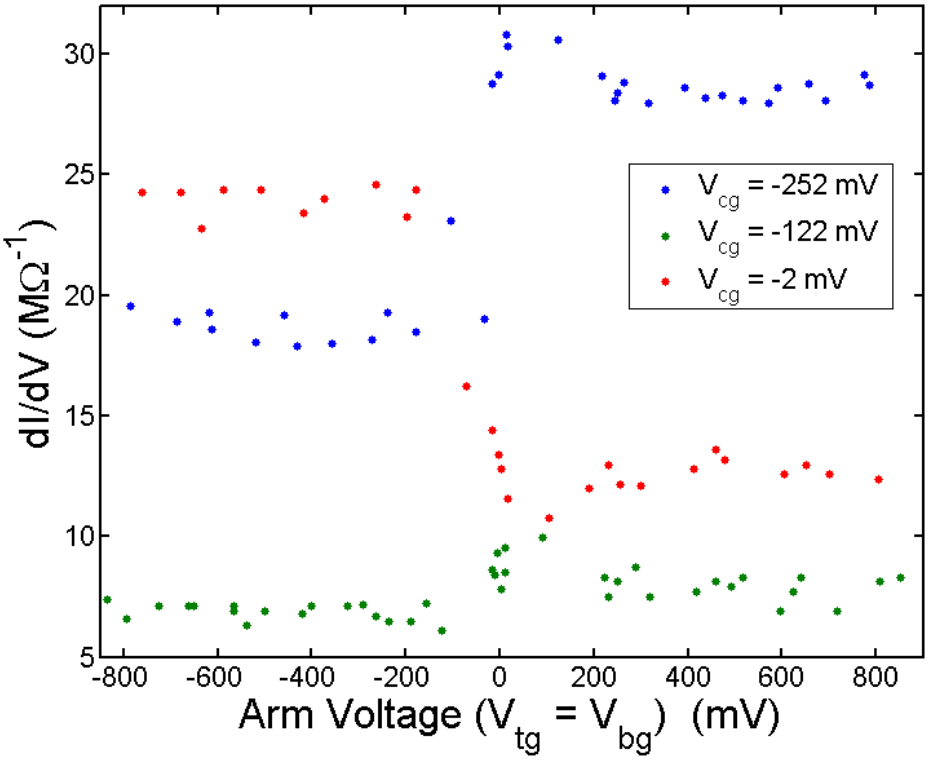

Figure 45: A plot of the small signal AC conductance as a function of arm bias voltage (top and bottom arm contacts are shorted together) at fixed optical pump power of 1100 μW, for varying values central bias voltage. Central value (V_{cg} = -122 mV) is near the conductance minimum for this pump power; other values are roughly equidistant from conductance minimum ($\approx \pm$ 120 mV). Laser is focused on central mesa region, near resonant to direct line (λ between 800 nm and 805 nm). Temperature is fixed at 4.5 K $\pm$ 0.5 K.

A more fair comparison is shown in Figure 45. In this plot, the dependence of the conductance on arm bias voltage is measured at fixed optical pump power (1100 μW) at several different central bias values. A rough measurement of the conductance versus V_{cg} was performed with the arm contacts floating, revealing that the conductance minimum occurred roughly at -120 mV. The curves in Figure 45 were measured at the floating conductance minimum value, -122 mV, and at points roughly equidistant from the central value (-2 mV and -252 mV).

The result of this measurement is interesting; near zero effective central bias (V_{cg} = -122 mV), there is little effect due to the variation of arm voltage. At positive effective central bias voltage (V_{cg} = -2 mV), the step behavior appears with high conductance at lower voltage. At negative central bias voltage, a similar step occurs with high conductance at negative voltage. In both cases, the step appears to be relatively sharp, occuring over 100-200 mV.

It is difficult to directly compare the magnitudes of the conuctance between the two curves in Figure 45; the conductance dependence on effective central bias is not completely symmetric (as can be seen in Figure 42). However, the shape of the curve is qualitatively different in the two scenarios.

One might expect that the arm voltage could slightly alter the tunneling into the substrate. In this scenario, one would expect that the conductance would increase when the arm voltage magnitude increases in the same direction as the effective central bias offset. That is, at negative effective central bias (V_{cg} = -252 mV in Figure 45), this effect would increase the conductance when the arm voltage is very negative. For both positive and negative effective bias points, this is the opposite of what is observed. This suggests that the tunneling current into the substrate is not significantly changed by the arm bias contacts.

It is worth noting that, based on Figure 31, an arm potential of $V_{arm} < V_{cg}$ corresponds to a barrier for electrons, while the opposite case indicates a barrier for holes. This seems to suggest that the observed asymmetry could be explained due to a change in the majority carrier when the polarity of the central bias is reversed. Using this interpretation, the curves in Figure 45 suggest that holes are the majority carrier when the effective central bias is negative (V_{cg} = -252 mV) and electrons are the majority carrier when effective central bias is positive (V_{cg} = -2 mV). It is not entirely clear why this change would occur. It may be

important that when the polarity of the central bias changes, the orientation of electrons and holes in the top and bottom wells also changes. Under positive bias, elecrons are expected to be primarily in the top well, under negative bias, holes are expected to be primarily in the top well.

While the step behavior only seems to appear under optical excitation, the asymmetry around $V_{\text{arm}} = 0$ does not go away. However, there are noticeable changes in the conductance when the ambient light is reduced by turning off all overhead lights in the lab, suggesting the system is very sensitive to background light (see footnote in Section 4.3.3.3).

The drastic change in the behavior under optical excitation seems to suggest that transport of excitons are involved. From the diagram in Figure 32, a cutoff in indirect exciton transport is expected to occur when the arm voltage opposes the direction of the central bias voltage. One can see from Figure 45, that this is the opposite of what is observed experimentally. For a net negative central bias, a positive applied arm bias increases the conductivity (and vice versa).

Alternatively, this effect could be attributed to a gradient of the potential across the sample, as illustrated in Figure 48. In this illustration, a DC voltage V is applied to the bias contacts and the diffused contacts. Directly adjacent to the diffused contacts, the voltage in the plain of the wells will be approximately V, assuming the contact resistance is negligible. Away from the diffused contacts, the GaAs can be treated as an insulating for calculating the DC electric field. Under the bias contact, the voltage at the plane of the quantum wells will be given by the distance from wells to the substrate / ground (0.34 μm) divided by the total distance from the contact to the substrate (1.08 μm), which will result in a voltage around 70% of the applied bias.

Also shown in Figure 48 is the effect of a positive and negative bias on the energy band diagram, taking this effect into consideration. If the indium contacts are sufficiently doped with zinc, near the contact the surrounding material can be treated as InAs [138] in the heavily p-doped regime. It is also assumed that the Fermi level stays fixed just above the InAs valence band; under the bias, this creates a trap for where carriers can accumulate (for positive potential, holes will accumulate, for negative potential electrons will accumulate).

This picture is consistent with the cutoff behavior in Figure 45. At positive total bias, an

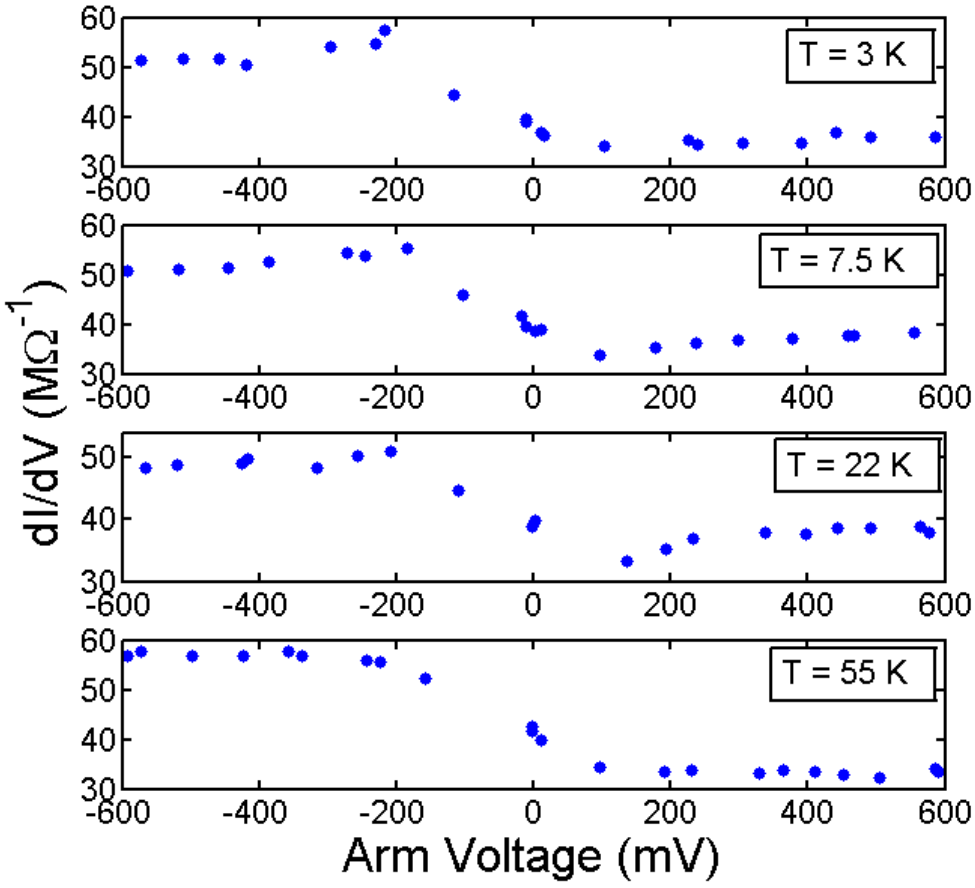

Figure 46: A plot of the small signal AC conductance as a function of arm bias voltage (top and bottom arm contacts are shorted together) at fixed optical pump power of 940 μW and constant central bias voltage (V_{cg} = +50 mV). Conductance minimum at this pump power was observed to be around V_{cg} = -100 mV. Laser is focused on central mesa region, near resonant to direct line (λ between 800 nm and 805 nm). Plotted for a range of temperature values: 3 K, 7.5 K, 22 K, 55 K

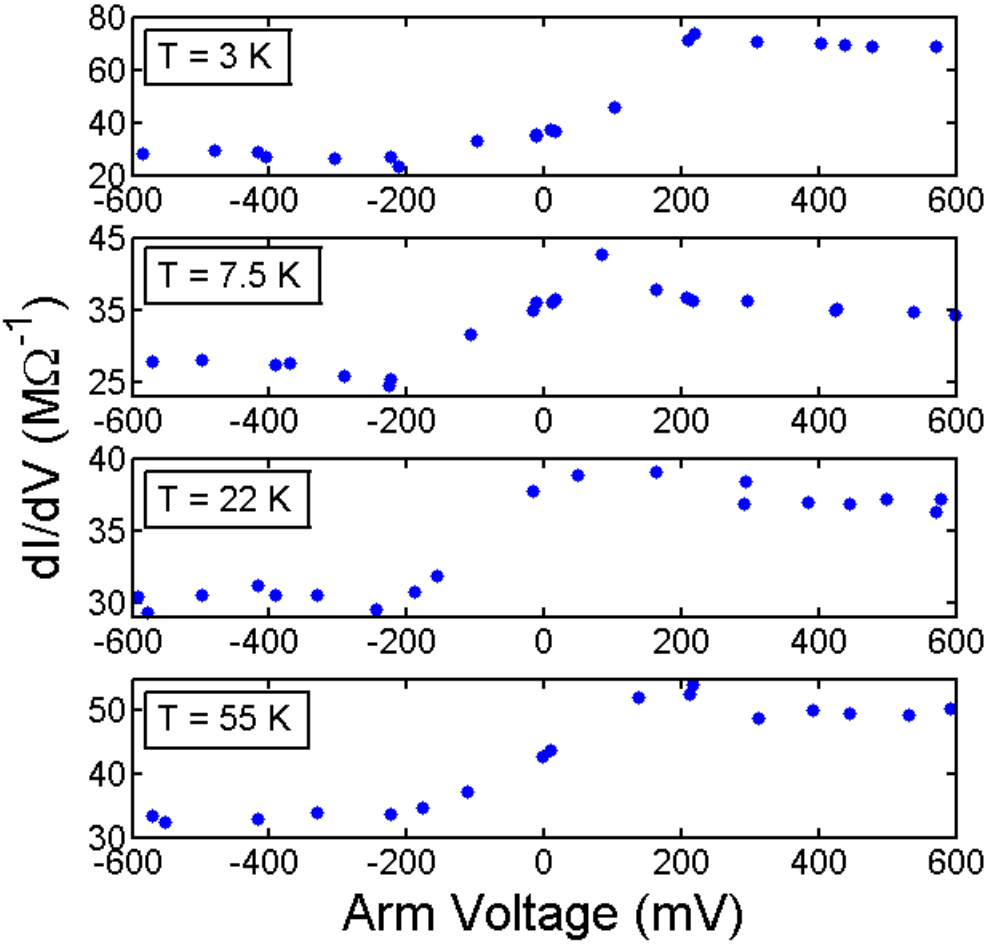

Figure 47: A plot of the small signal AC conductance as a function of arm bias voltage (top and bottom arm contacts are shorted together) at fixed optical pump power of 940 μW and constant central bias voltage (V_{cg} = -150 mV). Conductance minimum at this pump power was observed to be around V_{cg} = -100 mV. Laser is focused on central mesa region, near resonant to direct line (λ between 800 nm and 805 nm). Plotted for a range of temperature values: 3 K, 7.5 K, 22 K, 55 K

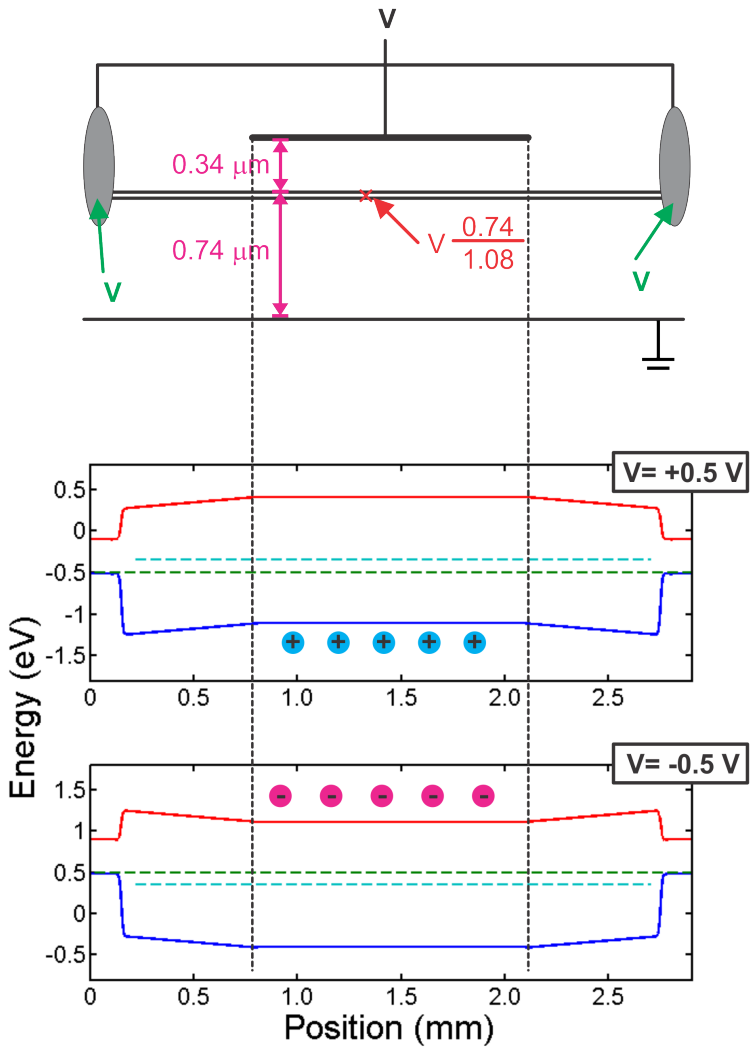

Figure 48: Shown is a cross-section of the sample, where a voltage V is applied to the central bias contact and the diffused indium contacts. Where the diffused contacts are in contact with the quantum wells, the voltage in the plane of the wells will be approximately V. Far away from the diffused contacts and under the bias contact, the voltage in the plane of the wells is reduced, as shown. In the bottom two panels, the energy bands for positive and negative applied voltage are shown, illustrating a shift in the Fermi level (green) relative to the intrinsic GaAs Fermi level (teal), resulting in an imbalance of electrons and holes under the contact, respectively.

excess of holes accumulates under the contacts which provide a conducting path across the sample. The flow of holes can be cut off by sufficiently positive arm bias, which is what is observed in the positive bias case in Figure 48. In the negative bias case, electrons will accumulate and the opposite behavior should be observed. Near zero bias, the structure should be near flat band, meaning there will be no accumulation of carriers under the contacts, and a uniformly low conductance is expected (and is observed). Recall that there will always be non-negligible conductance due to tunneling into the substrate, so it is not surprising that the conductance does not drop to zero in the cutoff regime.

The temperature dependence of this effect was tested up to 55 K, revealing that it persists up to relatively high temperature for both positive (Figure 46) and negative (Figure 47) effective bias. However, it does appear that magnitude of the step decreases significantly for the negative bias case for temperatures above 3 K (from, about 50 $M\Omega^{-1}$ at 3 K, to around 10 $M\Omega^{-1}$ in the range 7.5 K to 22 K, and 20 $M\Omega^{-1}$ at 55 K) while the positive bias curve is more or less constant (around 10-15 $M\Omega^{-1}$ for temperatures up to 22 K, increasing to around 30 $M\Omega^{-1}$ at 55 K). The sharp change in the negative bias case at low temperature could, alternatively, indicate that a sharp increase in the step size would also occur for the positive bias case, but at a temeprature lower than 3 K. It is worth noting that drastic change in the negative bias curve at low temperature occurs primarily on the high-conductivity size of the step. The low conductivity side of the step stays fixed around 25-30 $M\Omega^{-1}$.

4.3.4 Conclusions

From the results in Section 4.3.3.4, there is some indication that the cutoff arm bias has some effect on the transport, although the role played by electrons and holes within the structure is unclear. There is some indication that either one might play the role as the predominant charge carrier within certain regimes.

To fully understand the operation of this system, it would be useful to further isolate some of the many variables that are not well understood. For example, an identical sample could be grown in which the coupled quantum well structure is replaced with a single quantum well of equivalent width. This would help determine which experimental results are dependent

upon the orientation of electrons and holes within the coupled quantum well structure. It would also be useful to perform the same measurements on a sample with no quantum wells, to help identify which effects are simply related to properties of the contacts and the structure that surrounds the quantum wells.

A better understanding of the sysem could also be achieved simply by more thoroughly exploring the parameter space. It is clear that the conductance is strongly dependent on each of the bias voltage values, as well as the optical pump power. A more complete set of curves similar to Figure 45 could be informative. As would a more thorough exploration of the temperature dependence of the cutoff behavior.

In all the arm bias measurements discussed in the previous sections, the two arms were tied together. Measurements were also performed where the top and bottom arm contacts were varied independently; unfortunately, without a thorough understanding of what to look for, the parameter space in this scenario is very large (particularly when the central bias contact is also varied) and these measurements were not very informative.

If the model suggested by Figure 48 is correct, it means that the conductance is primarily a signature of free carriers, not excitons. However, the measurements shown here were performed using only two of the four diffused contacts in the sample. It may be possible to choose a bias configuration such that the region under the central bias contact is positively biased with respect to one set of the diffused contacts and negatively biased with respect to the other set; this would provide a conducting path for electrons through one set of contacts and a conducting path for holes through the other set, which was the primary design goal of this project (to achieve seperate contact to the top and bottom wells). It may also be possible to balance the bias voltages such that there is not imbalance of charge under the contacts (leading to an equal population of electrons and holes, and minimizing the presence of free carriers).

If the motion of charge in this structure can be thoroughly understood and reliable, independent contact of the wells can be demonstrated, drag and series counterflow measurements - as discussed in Section 4.1 - could be performed. For example, a series counterflow experiment could be performed by using the top contact to allow current to flow only through the top well and the bottom contact to allow current to flow only through the bottom well.

One side of the top well would then be shorted to one side of the top well, creating a path for current to go through the top well in one direction and in the bottom well in the opposite direction. The counterflow current can then be used as a tool to measure indirect exciton density or mobility. A sharp increase in the conductance at high pump power or low temperature could be an indicator of a superfluid transition.

A more ambitious goal would be to use this structure with the stress trapping technique discussed in previous chapters. Ideally, this could be a technique to probe the density of a dark exciton population. For the reasons discussed in Chapter 3, it seems unlikely that the sudden appearance of a dark population in the stress-trapped population is due to the appearance of a condensate, it does not rule out that there is some condensate fraction present. It may be possible that it is present, but more easily detected with transport measurements than via the photoluminescence.

APPENDIX A

MATLAB FUNCTION FOR FINDING SINGLE-PARTICLE ELECTRON AND HOLE ENERGY

The theoretical background needed to set up the single-particle eigenvalue equations for the conduction and valence bands are discussed in Chapter 2. Here, the numerical details and MATLAB code will be presented. The code presented here calculates the energy eigenvalues and eigenvectors for a particular value of in-plane $\vec{k}$, strain tensor ϵ_{ij}, structural parameters (e.g., well width, barrier composition, barrier width, etc.), and electric field. An example script that uses this function to calculate the trapping potential for a range of force values is presented in Appendix B.

A.1 CALCULATION DETAILS

There are several important components that go into calculating the energy eigenvalues of electrons and holes in the coupled quantum well system. First, the effect of the potential in the growth direction in conjunction with non-zero in-plane momentum must be considered. A quantum well is essentially a finite, one-dimensional potential well, which is an easily solved problem. However, there are important corrections that must be made due to subband mixing at finite k and due to the variation of the effective mass in the wells and in the barriers. Second, the strain contributions from the Pikus-Bir terms need to be included in the Hamiltonian. Third, the effect of an electric field in the growth direction must be

included. These issues will be outlined in the following sections.

A.2 LUTTINGER-KOHN HAMILTONIAN

The form of the Luttinger-Kohn Hamiltonian is shown in (1.24). While the kinetic energy terms are diagonal in the plane-wave basis, the potential is not. Due to the sharpness of the boundary, a plane-wave expansion of the potential would have components at very large momentum; this suggests it is more efficient to work in a spatial basis in the z-direction. In this case, all k_z terms must be re-written in terms of derivatives in z:

$$P = \frac{\hbar^2\gamma_1}{2m_0}\left(k_x^2 + k_y^2\right) - \frac{\hbar^2}{2m_0}\frac{\partial}{\partial z}\gamma_1(z)\frac{\partial}{\partial z}, \tag{A.1}$$

$$Q = \frac{\hbar^2\gamma_1}{2m_0}\left(k_x^2 + k_y^2\right) + 2\frac{\hbar^2}{2m_0}\frac{\partial}{\partial z}\gamma_2(z)\frac{\partial}{\partial z}, \tag{A.2}$$

$$R = \frac{\hbar^2}{2m_0}\left[-\sqrt{3}\gamma_2(z)\left(k_x^2 - k_y^2\right) + \mathrm{i}2\sqrt{3}\gamma_3(z)k_xk_y\right], \tag{A.3}$$

$$S = -\frac{\mathrm{i}}{2}\frac{\hbar^2}{2m_0}2\sqrt{3}\left(k_x - \mathrm{i}k_y\right)\left(\frac{\partial}{\partial z}\gamma_3(z) + \gamma_3(z)\frac{\partial}{\partial z}\right), \tag{A.4}$$

where the Luttinger-Kohn parameters - γ_1, γ_2 and γ_3 - have also been re-written to be functions of z. Note that when the mass is a function of position, the LK parameters do not commute with the momentum operator and one must pay close attention to their order. The shown expressions are symmetrized, as required to ensure continuity of the wave function and the probability current density [1]:

$$J_z(z) \propto \frac{1}{m(z)}\left[\psi^*\frac{\partial}{\partial z}\psi - \psi\frac{\partial}{\partial z}\psi^*\right]. \tag{A.5}$$

To project the LK Hamiltonian onto a discrete position basis, the partial derivatives in z need to be discretized. The discretization scheme must also be carefully considered to ensure that the continuity conditions are satisfied. One appropriate scheme requires that the material parameters and wave function be defined on a staggered grid [59]:

$$\frac{\partial}{\partial z}\gamma(z)\frac{\partial}{\partial z}\psi(z) \to \frac{\gamma_{n+\frac{1}{2}}}{\Delta z^2}\psi_{n+1} - \frac{\gamma_{n+\frac{1}{2}} + \gamma_{n-\frac{1}{2}}}{\Delta z^2}\psi_n + \frac{\gamma_{n-\frac{1}{2}}}{\Delta z^2}\psi_{n-1} \tag{A.6}$$

$$\frac{1}{2}\gamma(z)\frac{\partial}{\partial z}\psi(z) + \frac{1}{2}\frac{\partial}{\partial z}\gamma(z)\psi(z) \rightarrow \frac{1}{2}\gamma_{n+\frac{1}{2}}\psi_{n+1} - \frac{1}{2}\gamma_{n-\frac{1}{2}}\psi_{n-1} \tag{A.7}$$

$$V(z) \rightarrow \frac{1}{2}\left(V_{n+\frac{1}{2}} + V_{n-\frac{1}{2}}\right) \tag{A.8}$$

Here, each term has been re-defined on a discrete grid in the z-direction, with grid spacing Δz. The wave function and the material parameters have been on defined two separate grids that are offset by $\frac{1}{2}\Delta z$. For a grid with N points, this is converted from a 4×4 matrix to a 4N×4N matrix. Accuracy requires that the grid spacing be relatively small compared to the well size. The boundary conditions are effectively defined such that the wave function goes to zero at the edges of the problem space, so it is necessary that the edges are far away compared to the penetration depth into the barrier. In the code below, a barrier of 100 nm is assumed on each side of the well (unlike other geometric parameters, this was hard-coded and is not an input parameter of the function). It was found that a grid spacing on the order of 0.1 nm provided good agreement with analytical results at $k = 0$ (within a few percent for low lying eigenvalues for typical quantum well widths). Total mesh lengths on the order of 2000-5000 are typically used.

It is worth noting that, while the Hamiltonian in this basis is extremely large - a 20,000×20,000 matrix for N = 5000 - the number of non-zero elements is very sparse. In each N×N position-submatrix, only elements on the diagonal or one step away from the diagonal will be non-zero, which totals $3N - 2$ non-zero elements out of N^2. In the 4×4 Luttinger-Kohn submatrix, only 12 out of 16 elements are non-zero. In the end, only $\frac{3}{4}(3N - 2)$ elements out of $(4N)^2$ total elements will be non-zero. For N = 5000, there will be 45,000 non-zero elements out of 400 million. To store and diagonalize these matrices efficiently, it is necessary to use algorithms designed to deal with sparse matrices. Such tools are built in to MATLAB and are utilized by the script in Section A.7.

A.3 STRAIN

The role of strain in this calculation is discussed in detail in Chapter 2. Once the Hamiltonian is constructed as described in Section A.2, the strain terms of the Pikus-Bir Hamiltonian (as shown in (2.13)) can simply be added to the Hamiltonian along the diagonals of each position submatrix. The strain values are calculated using ANSYS, as discussed in Appendix C.

A.4 ELECTRIC FIELD

There are a number of ways to deal with an applied electric field, F_z. The simplest is to add the electric potential energy to the potential energy due to the quantum well structure:

$$V(z) \rightarrow V(z) + qF_z z. \tag{A.9}$$

This works well for small electric field values, where the total voltage drop from the well to the edge of the problem space is less than the depth of the well, and is the method used in the code in Section A.7.

If the electric field is too large, confined states that are lower in energy than the quantum well states will appear at the boundaries. In the actual structure, an extended tail into the structure will exist and there may be a continuum of free states that are below the confined states of the quantum well[1]. In practice, once carriers are localized in the quantum well, the tunneling rate out of the well is expected to be small compared to the radiative recombination rate, making confined quantum well states a reasonable approximation.

Another simple fix is to solve for the quantum well confined states at zero electric field, calculate the matrix elements of the electric field operator in this basis, and then re-diagonalize the Hamiltonian in the basis of the zero-field eigenstates. This approximates the Stark shift for confined states, but eliminates the component of the wave function ex-

[1] Analytically, the eigenstates for a quantum well in a constant electric field are Airy functions, which have an oscillating tail away from the quantum well [59]. The presence of a superlattice complicates the analysis.

tending far outside the quantum wells. This approach was implemented and compared to the case where the field is simply added to the potential energy. For electric field values relevant to this work (a few mV/nm), both methods produced similar results.

A.5 OPTIMIZATION

In MATLAB, it can be inefficient to define matrices element by element within a for-loop. It is typically far more efficient to vectorize this process. In the code below, for-loops are used extensively. This was a conscious decision, as the discretization scheme is somewhat complex and this approach makes the code more readable. It was also found that the diagonalization step is significantly more computationally intensive than the step where the matrices are defined [2], so any improvement due to vectorizing the matric element allocation would be incremental. Nonetheless, this is one way the code below can be optimized.

If only the lowest few eigenvalues are desired, the run time can be significantly reduced by properly setting the `numberEigenvalues` variable to the minimum possible value. It is possible to generate all $4N$ eigenvalues, but only a small number of the lowest eigenvalues are physically meaningful. When the energy eigenvalues are larger than the quantum well depth, the calculated eigenstates will be simply the quasi-continuum associated with unconfined states. In other words, the eigenvalues will be determined by confinement at the boundaries of the problem space.

A.6 REFERENCES

The material parameters used in the following code were taken from Chuang [1].

[2] In one characteristic run where N = 5000, over 98% of the run time was found to be devoted to calculating the eigenvalues and eigenvectors. Defining the matrix elements required 1-2% of the entire run time.

```
function [eigenStates,Xpts] = ...
    CarrierEigenStates(kVector, strainComponents, geometryParameters,...
    electricField, numberEigenvalues,showMsgsSwitch)

% Inputs:
% kVector = [kx, ky] — In plane k—vector of electron or hole
% strainComponents: Data structure containing exx, eyy, ezz, exy, eyz, exz
% geometryParameters: Data structure that describes whether single well or
%                     CQW, barrier width, well width, alloy fraction, and
%                     number of divisions
% numberEigenvalues: The number of lowest eigenvalues the program
%                    calculates — calculates four times as many for hole
%                    states
% electricField:     Transverse field in meV/nm
% showMsgsSwitch:    Boolean variable, shows progress messages and warnings
%                    in MATLAB command window if true

% Outputs:
% Xpts: 1xN vector containing the sampled positions
% eigenStates: Data structure containing electron and hole eigenvalues and
%              eigenvectors

% Harvesting input parameters

kx = kVector(1);
ky = kVector(2);

exx = strainComponents.exx;
eyy = strainComponents.eyy;
ezz = strainComponents.ezz;
exy = strainComponents.exy;
eyz = strainComponents.eyz;
exz = strainComponents.exz;

xAlloy = geometryParameters.alloyFraction;

Npts = geometryParameters.numberDivisions;

% Material Constants for GaAs

Egap_GaAs = 1519;                           % meV, T = 0 K

Egap_AlGaAs = 1519 + 1447*xAlloy — 0.15*(xAlloy^2);
% meV, T = 0 K, alloy fraction < 0.4, Chuang

if(showMsgsSwitch)
    disp('Warning: Assuming T = 0 K for band gap.' + ...
        'Arbitrary temperature not implemented yet.');
```

```
end

Vc = 0.67*(Egap_AlGaAs - Egap_GaAs);
Vv = 0.33*(Egap_AlGaAs - Egap_GaAs);      %% Chuang, 0.67/0.33

%% Transport parameters for valence band of GaAs, AlAs and alloy

gamma1GaAs = 6.8;           % From Chuang
gamma2GaAs = 1.9;
gamma3GaAs = 2.73;

gamma1AlAs = 3.45;
gamma2AlAs = 0.68;
gamma3AlAs = 1.29;

gamma1Well = gamma1GaAs;
gamma2Well = gamma2GaAs;
gamma3Well = gamma3GaAs;

gamma1Barr = xAlloy*gamma1AlAs + (1-xAlloy)*gamma1GaAs;
gamma2Barr = xAlloy*gamma2AlAs + (1-xAlloy)*gamma2GaAs;
gamma3Barr = xAlloy*gamma3AlAs + (1-xAlloy)*gamma3GaAs;

alpha0 = 38.1;          % meV*nm*nm, hbar^2/(2*m0)

% Generates potential as a function of position
[~,Velectron] = Potential1D(0,Vc,geometryParameters, Npts);
[Xpts,Vhole] = Potential1D(0,Vv,geometryParameters, Npts);

delta = (max(Xpts)-min(Xpts))/Npts;         % Grid size

% Generates transport mass parameters as a function of position
gamma1(1:Npts) = gamma1Barr;
gamma2(1:Npts) = gamma2Barr;
gamma3(1:Npts) = gamma3Barr;

gamma1(Vhole == 0) = gamma1Well;
gamma2(Vhole == 0) = gamma2Well;
gamma3(Vhole == 0) = gamma3Well;

%% Assigns effective electron mass as a function of position

electronMassGaAs = 0.067;
electronMassAlAs = 0.15;

electronMassWell = electronMassGaAs;
electronMassBarr = electronMassGaAs*(1-xAlloy) + electronMassAlAs*xAlloy;

electronMass(1:Npts) = electronMassBarr;
electronMass(Velectron == 0) = electronMassWell;

%% Generate deformation potential parameters as a function of position

acGaAs = -7.17e3;     % Chuang, in meV
```

```
avGaAs = 1.16e3;
bGaAs = -1.7e3;
dGaAs = -4.55e3;

acAlAs = -5.64e3;
avAlAs = 2.47e3;
bAlAs = -1.5e3;
dAlAs = -3.4e3;

acWell = acGaAs;
avWell = avGaAs;
bWell = bGaAs;
dWell = dGaAs;

acBarr = xAlloy*acAlAs + (1-xAlloy)*acGaAs;
avBarr = xAlloy*avAlAs + (1-xAlloy)*avGaAs;
bBarr = xAlloy*bAlAs + (1-xAlloy)*bGaAs;
dBarr = xAlloy*dAlAs + (1-xAlloy)*dGaAs;

ac(1:Npts) = acBarr;
av(1:Npts) = avBarr;
b(1:Npts) = bBarr;
d(1:Npts) = dBarr;

ac(Vhole == 0) = acWell;
av(Vhole == 0) = avWell;
b(Vhole == 0) = bWell;
d(Vhole == 0) = dWell;

% Generates Hamiltonian for electron states
if(showMsgsSwitch)
    disp('Generating the electron Hamiltonian...');
end

% Allocates Hamiltonian in position basis as sparse matrix
MatrixElectron = spalloc(Npts,Npts,3*Npts-2);

for nn = 1 : Npts

    if(nn  == Npts || nn == 1)
        MatrixElectron(nn,nn) = Velectron(nn) ...
            - electricField*Xpts(nn) + ...
            (alpha0/electronMass(nn))*(kx^2 + ky^2) + ...
            (2*alpha0/electronMass(nn))*(1/delta^2) + ...
            ac(nn)*(exx + eyy + ezz);
    end

    if( nn < Npts)

        MatrixElectron(nn,nn) = 0.5*(Velectron(nn)+Velectron(nn+1)) - ...
            0.5*electricField*(Xpts(nn) + Xpts(nn+1)) + ...
            (alpha0/(0.5*electronMass(nn) + ...
            0.5*electronMass(nn+1)))*(kx^2 + ky^2) + ...
            (alpha0/(delta^2))*((1/electronMass(nn))+...
```

```
            (1/electronMass(nn+1))) + ac(nn)*(exx + eyy + ezz);

        MatrixElectron(nn,nn+1) = ...
            -(alpha0/(delta^2))*(1/electronMass(nn+1));

    end

    if(nn > 1)
        MatrixElectron(nn,nn-1) = -(alpha0/(delta^2))*(1/electronMass(nn));
    end

end

if(showMsgsSwitch)
    disp('Calculating the electron eigenvalues and eigenvectors...');
end
[electronEigenvectors,electronEigenvalues] = ...
    eigs(MatrixElectron,numberEigenvalues,0);

% Sort eigenvalues and eigenvectors (from smallest to largest)
[electronEigenvalues, order] = sort(diag(electronEigenvalues),'ascend');
electronEigenvectors = electronEigenvectors(:,order);

% Generates Luttinger-Kohn Hamiltonian for hole states in position basis

if(showMsgsSwitch)
    disp('Generating the hole Hamiltonian...');
end

M11 = spalloc(Npts,Npts,3*Npts-2);
M12 = spalloc(Npts,Npts,3*Npts-2);
M13 = spalloc(Npts,Npts,Npts);
M22 = spalloc(Npts,Npts,3*Npts-2);

for nn = 1 : Npts

    if(nn  == Npts || nn == 1)

        M11(nn,nn) = Vhole(nn) + electricField*Xpts(nn) + ...
            2*(alpha0/(delta^2))*(gamma1(nn) - 2*gamma2(nn))  + ...
            alpha0*(gamma1(nn)+gamma2(nn))*(kx^2 + ky^2) - ...
            (av(nn) + 0.5*b(nn))*(exx + eyy) - (av(nn) + b(nn))*ezz;

        M22(nn,nn) = Vhole(nn) + electricField*Xpts(nn) + ...
            2*(alpha0/(delta^2))*(gamma1(nn) + 2*gamma2(nn))  + ...
            alpha0*(gamma1(nn)-gamma2(nn))*(kx^2 + ky^2) - ...
            (av(nn) - 0.5*b(nn))*(exx + eyy) - (av(nn) - b(nn))*ezz;

        M13(nn,nn) = alpha0*(-sqrt(3)*gamma2(nn)*(kx^2 - ky^2) + ...
            1i*2*sqrt(3)*gamma3(nn)*kx*ky) + ...
            (sqrt(3)*b(nn)/2)*(exx-eyy) - 1i*d(nn)*exy;

        M12(nn,nn) = 0.5*d(nn)*(exz-1i*eyz);
```

```
    end

    if(nn < Npts)

        M11(nn,nn) = 0.5*(Vhole(nn) + Vhole(nn+1)) + ...
            0.5*electricField*(Xpts(nn) + Xpts(nn+1)) + ...
            (alpha0/(delta^2))*(gamma1(nn) + gamma1(nn+1) - ...
            2*gamma2(nn+1) - 2*gamma2(nn)) + 0.5*alpha0*(gamma1(nn)+ ...
            gamma2(nn) + gamma1(nn+1) + gamma2(nn+1))*(kx^2 + ky^2) - ...
            0.5*(av(nn) + av(nn+1) + ...
            0.5*b(nn) + 0.5*b(nn+1))*(exx + eyy) - ...
            0.5*(av(nn) + av(nn+1) + b(nn) + b(nn+1))*ezz;

        M11(nn,nn+1) = -(alpha0/(delta^2))*(gamma1(nn+1)-2*gamma2(nn+1));
        M11(nn+1,nn) =  -(alpha0/(delta^2))*(gamma1(nn+1)-2*gamma2(nn+1));

        M22(nn,nn) = 0.5*(Vhole(nn) + Vhole(nn+1)) + ...
            0.5*electricField*(Xpts(nn) + Xpts(nn+1)) + ...
            (alpha0/(delta^2))*(gamma1(nn) + gamma1(nn+1) + ...
            2*gamma2(nn+1) + 2*gamma2(nn)) + 0.5*alpha0*(gamma1(nn)- ...
            gamma2(nn) + gamma1(nn+1) - gamma2(nn+1))*(kx^2 + ky^2) - ...
            0.5*(av(nn) + av(nn+1) - 0.5*b(nn) - ...
            0.5*b(nn+1))*(exx + eyy) - 0.5*(av(nn) + av(nn+1) -...
            b(nn) - b(nn+1))*ezz;

        M22(nn,nn+1) = -(alpha0/(delta^2))*(gamma1(nn+1)+2*gamma2(nn+1));
        M22(nn+1,nn) = -(alpha0/(delta^2))*(gamma1(nn+1) + 2*gamma2(nn+1));

        M13(nn,nn) = ...
            alpha0*(-0.5*sqrt(3)*(gamma2(nn)+gamma2(nn+1))*(kx^2 - ky^2)...
            + 1i*sqrt(3)*(gamma3(nn)+gamma3(nn+1))*kx*ky) + ...
            (sqrt(3)*0.5*(b(nn)+b(nn+1))/2)*(exx-eyy) - 1i*d(nn)*exy;

        M12(nn,nn) = 0.5*(d(nn) + d(nn+1))*(exz-1i*eyz);

        M12(nn,nn+1) = ...
            -1i*alpha0*2*sqrt(3)*(kx-1i*ky)*(1/(2*delta))*gamma3(nn);

        M12(nn+1,nn) = ...
            1i*alpha0*2*sqrt(3)*(kx-1i*ky)*(1/(2*delta))*gamma3(nn);
    end
end

M24 = M13;
M34 = -M12;
M33 = M22;
M44 = M11;
M21 = ctranspose(M12);
M31 = ctranspose(M13);
M42 = ctranspose(M24);
M43 = ctranspose(M34);

MatrixHole = sparse(4*Npts,4*Npts);
```

```
MatrixHole(1:Npts,1:Npts) = M11;
MatrixHole(1:Npts,Npts+1:2*Npts) = M12;
MatrixHole(1:Npts,2*Npts+1:3*Npts) = M13;
MatrixHole(Npts+1:2*Npts,1:Npts) = M21;
MatrixHole(Npts+1:2*Npts,Npts+1:2*Npts) = M22;
MatrixHole(Npts+1:2*Npts,3*Npts+1:4*Npts) = M24;
MatrixHole(2*Npts+1:3*Npts,1:Npts) = M31;
MatrixHole(2*Npts+1:3*Npts,2*Npts+1:3*Npts) = M33;
MatrixHole(2*Npts+1:3*Npts,3*Npts+1:4*Npts) = M34;
MatrixHole(3*Npts+1:4*Npts,Npts+1:2*Npts) = M42;
MatrixHole(3*Npts+1:4*Npts,2*Npts+1:3*Npts) = M43;
MatrixHole(3*Npts+1:4*Npts,3*Npts+1:4*Npts) = M44;

if(showMsgsSwitch)
    disp('Calculating the hole eigenvalues and eigenvectors...');
end

[holeEigenvectors,holeEigenvalues] = ...
    eigs(MatrixHole,4*numberEigenvalues,0);

% Sort eigenvalues and eigenvectors (from smallest to largest)
[holeEigenvalues, order] = sort(diag(holeEigenvalues),'ascend');
holeEigenvectors = holeEigenvectors(:,order);

eigenStates = struct('electronEigenvalues',electronEigenvalues,...
    'electronEigenvectors',electronEigenvectors,'holeEigenvalues',...
    holeEigenvalues,'holeEigenvectors',holeEigenvectors);

function [Xpts,V] = Potential1D(Vwell,Vbar,geometryParameters, Npts)

% Outputs the potential along the quantum well direction as a function of
% position.
% bufferWidth is space between edge of well and boundary of problem space
% If you make bufferWidth too small you can get confinement effects between
% edges. But you can adjust this if runtime is too slow.

    aWell = geometryParameters.wellWidth;
    % Space between edge of well and boundary of problem space
    % You can make this smaller for smaller grid size, if you make it too
    % small, you may get boundary effects
    bufferWidth = 100;
    V(1:Npts) = 0;

    if(~geometryParameters.isCQW)
        problemSpace = (aWell + 2*bufferWidth);
        Xpts = linspace(-0.5*problemSpace,0.5*problemSpace, Npts);
        V(abs(Xpts) >= 0.5*aWell) = Vbar;
        V(abs(Xpts) < 0.5*aWell) = Vwell;
    else
        barWidth = geometryParameters.barrierWidth;

        problemSpace = (2*aWell + barWidth + 2*bufferWidth);
        Xpts = linspace(-0.5*problemSpace,0.5*problemSpace, Npts);
```

```
        V(1:Npts) = Vwell;
        V(abs(Xpts)<0.5*barWidth) = Vbar;
        V(abs(Xpts)>0.5*barWidth + aWell) = Vbar;
    end
end
end
```

APPENDIX B

MATLAB SCRIPT FOR FINDING TRAP PROFILE

This script requires the CarrierEigenStates.m script presented in Appendix A and the output from the ANSYS calculation from Appendix C. This particular script parses the profile as a diagonal cross-section along a 2D strain map (in other words, as a cross-section along the [110] direction in the plane of the quantum wells). Run time can be reduced by only calculating the lowest few eigenvalues or by lowering the resolution and/or total size of the spatial grid discussed in Appendix A.2. The latter option should be done conservatively and one should double check the accuracy of the results after doing so.

The CarrierEigenStates function also is only intended to take the strain components as scalars. To more efficiently utilize MATLAB's ability to manipulate arrays, the CarrierEigenStates.m should be altered and the for-loops in this script should be eliminated. Alternatively, the run time can be improved on systems with multiple processors or multiple cores by replacing the inner for-loop with a parallelized parfor-loop.

```
%% Strain Trap Profile Script

% Strain values exx, eyy, ezz, exy, eyz, and exz must be imported into
% workspace as 2D arrays. Strain should be calculated at nominal 1 N force.

% Calculates the lowest three electron eigenstates and lowest six hole
% eigenstates.

F0 = [0.25 0.50 0.75 1.00 1.25 1.50];   % Nominal force values
fVals = length(F0);
Nx = length(exx);                       % Size of strain matrix
```

```
electricField = 1;      %mV/nm

ElectronEnergy1(1:Nx,1:6) = 0;          %Pre-allocating arrays
ElectronEnergy2(1:Nx,1:6) = 0;
ElectronEnergy3(1:Nx,1:6) = 0;

HoleEnergy1(1:Nx,1:6) = 0;
HoleEnergy2(1:Nx,1:6) = 0;
HoleEnergy3(1:Nx,1:6) = 0;
HoleEnergy4(1:Nx,1:6) = 0;
HoleEnergy5(1:Nx,1:6) = 0;
HoleEnergy6(1:Nx,1:6) = 0;

for nn = 1 : 1
    nn
    Fval = F0(nn);

    for ii = 1 : Nx

        kVector = [0,0];

        % 14 nm coupled quantum wells with a 4 nm barrier,
        % 0.45 alloy barrier
        geometryParameters = struct('wellWidth',14,'isCQW',true,...
            'alloyFraction',0.45,'numberDivisions',4000, 'barrierWidth',4);

        % At each point, strain is scaled according to force
        strainComponents = struct('exx',exx(ii,ii)*Fval,'eyy',...
            eyy(ii,ii)*Fval,'ezz',ezz(ii,ii)*Fval,'exy',...
            exy(ii,ii)*Fval,'exz',exz(ii,ii)*Fval,'eyz',...
            eyz(ii,ii)*Fval);

        % Eigenstates are calculated using CarrierEigenstates.m
        [eigenStates,Xpts] = CarrierEigenStates(kVector,...
            strainComponents, geometryParameters,electricField,3,false);

        ElectronEnergy1(ii,nn) = eigenStates.electronEigenvalues(1);
        ElectronEnergy2(ii,nn) = eigenStates.electronEigenvalues(2);
        ElectronEnergy3(ii,nn) = eigenStates.electronEigenvalues(3);

        HoleEnergy1(ii,nn) = eigenStates.holeEigenvalues(1);
        HoleEnergy2(ii,nn) = eigenStates.holeEigenvalues(2);
        HoleEnergy3(ii,nn) = eigenStates.holeEigenvalues(3);
        HoleEnergy4(ii,nn) = eigenStates.holeEigenvalues(4);
        HoleEnergy5(ii,nn) = eigenStates.holeEigenvalues(5);
        HoleEnergy6(ii,nn) = eigenStates.holeEigenvalues(6);

    end
end
```

APPENDIX C

CALCULATING STRAIN MAP USING FINITE-ELEMENT SOFTWARE

C.1 GENERATING STRAIN WITH ANSYS

This code is intended to be executed in the ANSYS Mechanical APDL (ANSYS Parametric Design Language) environment. After the following script is run, the equilibrium solution is saved to memory.

This script is modified from the code and finite-element geometry generated by Ryan Balili for studying the microcavity polariton system [144], which was originally designed in collaboration with R.H. Reid [80]. Parameters and geometry were modified to account for differences in coupled quantum well structure. The material parameters used herein are from Adachi [48].

```
finish
/clear

/title, CQW - Wuenschell

! Units:
! Length units in mm
! Force units in N
```

```
! Geometric parameters:
thickness       =  0.140    ! Chip thickness (mm)
width       =  2.500        ! Horizontal size of chip (mm)
pinradius       =  0.050    ! Pin radius (mm)
holeradius       =  1       ! Hole radius (mm)

!Nominal applied force in Newtons
!Do not trust this! Use trap depth to calibrate force.
load     =  1.0

!Finite-element geometry generated by defining geometry in ANSYS GUI
!and translated into code. Based on geometry used by
!R. Balili and R.H. Reid

!Keypoints

!Geometry of mesh (number of grid points):
npts1      = 8                ! Region under pin
npts2      = 30               ! Region over hole
npts3      = 7                ! Region over plate
nptsI     = 7                 ! Divisions of inner arc
nptsO     = nptsI             ! Divisions of inner arc
nptsEdge    = nptsI           ! Divisions along outer edge
nptsz     = 11                ! Divisions in growth direction

! Plotting
/triad, off

/prep7
local, 11, 1
```

```
! Generate key points

csys, 0
k, 1, 0, 0, 0
k, 2, pinradius, 0, 0
k, 3, holeradius, 0, 0
k, 4, width/2, 0, 0
k, 5, width/2,width/2,0
k, 6, 0, width/2, 0
k, 7, 0, holeradius, 0
k, 8, 0, pinradius, 0

csys, 11
k, 9, pinradius, 45, 0
k, 10, holeradius, 45, 0

csys, 0
k, 11, -pinradius, 0, 0
k, 12, -holeradius, 0, 0
k, 13, -width/2, 0, 0
k, 14, -width/2,-width/2,0
k, 15, 0, -width/2, 0
k, 16, 0, -holeradius, 0
k, 17, 0, -pinradius, 0

csys, 11
k, 18, pinradius, 225, 0
k, 19, holeradius, 225, 0
```

```
csys, 0
k, 20, -width/2,width/2,0

csys, 11
k, 21, pinradius, 135, 0
k, 22, holeradius, 135, 0

csys, 0
k, 23, width/2,-width/2,0

csys, 11
k, 24, pinradius, 315, 0
k, 25, holeradius, 315, 0

csys, 0
kgen, 2, all, , , , , thickness, 25

! Generate lines

l, 1, 2, npts1 $l, 26, 27, npts1
l, 1, 11,npts1 $l, 26, 36, npts1

l, 2, 3, npts2 $l, 27, 28, npts2
l, 11, 12,npts2 $l, 36, 37, npts2

l, 3, 4, npts3 $l, 28, 29, npts3
l, 12,13, npts3 $l, 37, 38, npts3

l, 1, 8, npts1 $l, 26, 33, npts1
l, 1, 17, npts1 $l, 26, 42, npts1
```

```
l, 8, 7, npts2 $l, 33, 32, npts2
l, 17,16, npts2 $l, 42, 41, npts2

l, 7, 6, npts3 $l, 32, 31, npts3
l, 16, 15, npts3 $l, 41, 40, npts3

l, 4, 5, nptsEdge $l, 29, 30, nptsEdge
l, 5, 6, nptsEdge $l, 31, 30, nptsEdge

l, 13, 14, nptsEdge $l, 38, 39, nptsEdge
l, 14, 15, nptsEdge $l, 39, 40, nptsEdge

l, 13, 20, nptsEdge $l, 38, 45, nptsEdge
l, 20, 6, nptsEdge  $l, 45, 31, nptsEdge

l, 4, 23, nptsEdge  $l, 29, 48, nptsEdge
l, 23, 15, nptsEdge $l, 48, 40, nptsEdge

csys, 11

l, 2, 9, nptsI $l, 27, 34, nptsI
l, 9, 8, nptsI $l, 34, 33, nptsI

l, 8, 21, nptsI $l, 33, 46, nptsI
l, 21, 11, nptsI $l, 46, 36, nptsI

l, 11, 18, nptsI $l, 36, 43, nptsI
l, 18, 17, nptsI $l, 43, 42, nptsI
```

```
l, 17, 24, nptsI $l, 42, 49, nptsI
l, 24, 2, nptsI $l, 49, 27, nptsI

l, 3, 10, npts0 $l, 28, 35, nptsI
l, 10, 7, npts0 $l, 35, 32, nptsI

l, 7, 22, npts0 $l, 32, 47, npts0
l, 22, 12, npts0 $l, 47, 37, npts0

l, 12, 19, npts0 $l, 37, 44, npts0
l, 19, 16, npts0 $l, 44, 41, npts0

l, 16, 25, npts0 $l, 41, 50, npts0
l, 25, 3, npts0 $l, 50, 28, npts0

csys, 0

l, 9, 10, npts2 $l, 34, 35, npts2
l, 10, 5, npts3 $l, 35, 29, npts3

l, 18, 19, npts2 $l, 43, 44, npts2
l, 19, 14, npts3 $l, 44, 39, npts3

l, 21, 22, npts2 $l, 46, 47, npts2
l, 22, 20, npts3 $l, 47, 45, npts3

l, 24, 25, npts2 $l, 49, 50, npts2
l, 25, 23, npts3 $l, 50, 48, npts3

csys, 0
```

```
l, 1, 26, nptsz
l, 2, 27, nptsz
l, 3, 28, nptsz
l, 4, 29, nptsz
l, 5, 30, nptsz
l, 6, 31, nptsz
l, 7, 32, nptsz
l, 8, 33, nptsz
l, 9, 34, nptsz
l, 10, 35, nptsz
l, 11, 36, nptsz
l, 12, 37, nptsz
l, 13, 38, nptsz
l, 14, 39, nptsz
l, 15, 40, nptsz
l, 16, 41, nptsz
l, 17, 42, nptsz
l, 18, 43, nptsz
l, 19, 44, nptsz
l, 20, 45, nptsz
l, 21, 46, nptsz
l, 22, 47, nptsz
l, 23, 48, nptsz
l, 24, 49, nptsz
l, 25, 50, nptsz

! Generate volumes

V, 1, 2, 9, 8, 26, 27, 34, 33
V, 2, 3, 10, 9, 27, 28, 35, 34
```

```
V, 9, 10, 7, 8, 34, 35, 32, 33
V, 10, 5, 6, 7, 35, 30, 31, 32
V, 10, 5, 4, 3, 35, 30, 29, 28

V, 1, 8, 21, 11, 26, 33, 46, 36
V, 8, 7, 22, 21, 33, 32, 47, 46
V, 21, 22, 12, 11, 46, 47, 37, 36
V, 22, 20, 6, 7, 47, 45, 31, 32
V, 22, 20, 13, 12, 47, 45, 38, 37

V, 1, 11, 18, 17, 26, 36, 43, 42
V, 11, 12, 19, 18, 36, 37, 44, 43
V, 18, 19, 16, 17, 43, 44, 41, 42
V, 19, 14, 13, 12, 44, 39, 38, 37
V, 19, 14, 15, 16, 44, 39, 40, 41

V, 1, 17, 24, 2, 26, 42, 49, 27
V, 17, 16, 25, 24, 42, 41, 50, 49
V, 24, 25, 3, 2, 49, 50, 28, 27
V, 25, 23, 15, 16, 50, 48, 40, 41
V, 25, 23, 4, 3, 50, 48, 29, 28

ET,1,SOLID185

! Material Properties:
! Define elastic tensor in N/mm^2
! Using parameters for GaAs, taken from Adachi
! At T = 0 K

TB,ANEL,1,1,21,0
```

```
TBTEMP,0
TBDATA,,12.11e4,5.48e4,5.48e4,0,0,0
TBDATA,,12.11e4,5.48e4,0,0,0,12.11e4
TBDATA,,0,0,0,6.04e4,0,0
TBDATA,,6.04e4,0,6.04e4,,,

! Create Elements:

mshape, 0
vmesh, all

! Boundary Conditions:
! Top and bottom plates allow no displacement
! ux, uy, uz = 0 in plate region

! Top plate (with circular hole in top)

csys, 11
nsel, s, loc, x, holeradius, width
nsel, r, loc, z, thickness
d, all, all, 0
csys, 0
alls

! Bottom plate (with circular hole)

csys, 11
nsel, s, loc, x, holeradius, width
nsel, r, loc, z, 0
d, all, all,0
```

```
csys, 0
alls

! Apply load:
! Assumes constant force over circular pin
! More complicated pin models give similar results

csys, 11
nsel, s, loc, x, 0, pinradius
nsel, r, loc, z, thickness
*get, ncount, node, 0, count
f, all, fz,-load/ncount
csys, 0
alls

! Transfer loads to model:

sbctran
/pbc, all, 1
eplo
fini

/sol
solve
fini
```

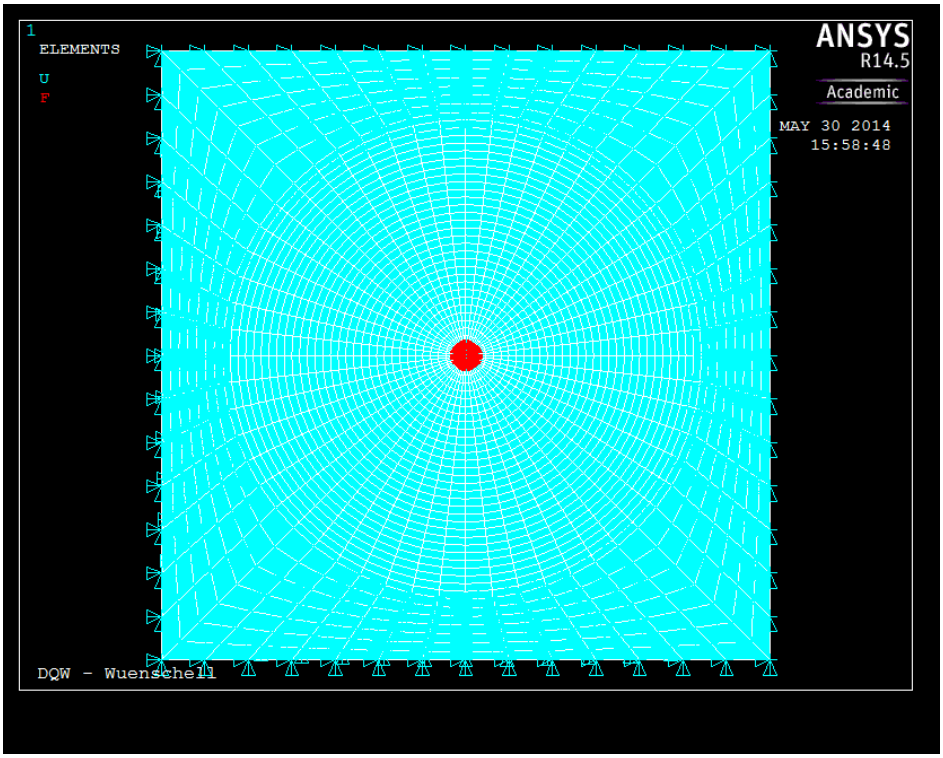

Figure 49: A top-down view of the 3D finite-element mesh generated by the script given.

C.2 READING RESULTS FROM ANSYS

The following script should be run directly after running the above script. It outputs the strain components approximately in the plane of the quantum wells (500 nm from the bottom of the sample). This particular script generates a relatively high-resolution 2D map of all six strain components (approximate resolution is 8 μm). The data is output to 300 text files.

This script can take a long time to run. Faster processing time can be achieved by lowering the resolution, cutting down the problem space, or only reading out a 1D cross-section (the last option is a vast improvement; for a 300 $\times$ 300 grid, it will run 300 times faster). Keep in mind that this script only reads out the existing results, so modifying the resolution will only reduce the amount of information extracted, it does not effect the accuracy of the simulation.

```
! Post-Process:
/post1

/NERR, 0

XInc = width/299

! Loops over rows along 2D profile
! Takes a long time to run!

*DO, II, 1, 300

Xpt = -width/2 + XInc*(II-1)

PATH,LinePath,2,300,300,!Define path for data

PPATH,1,0,Xpt,-width/2,0.0005,0,!Path at bottom of sample (500 nm from bottom)
```

```
PPATH,2,0,Xpt,width/2,0.0005,0,

AVPRIN,0, ,
PDEF, ,EPEL,X,AVG

AVPRIN,0, ,
PDEF, ,EPEL,Y,AVG

AVPRIN,0, ,
PDEF, ,EPEL,Z,AVG

AVPRIN,0, ,
PDEF, ,EPEL,XY,AVG

AVPRIN,0, ,
PDEF, ,EPEL,YZ,AVG

AVPRIN,0, ,
PDEF, ,EPEL,XZ,AVG

AVPRIN,0,,
PDEF, ,U,Z,AVG

/PAGE,1000,,1000,
/OUTPUT,CQW_091813_%II%,txt,

!List strain
PRPATH, EPELX, EPELY, EPELZ, EPELXY, EPELYZ, EPELXZ
```

```
/OUTPUT

*ENDDO
```

C.3 MATLAB SCRIPT FOR PROCESSING ANSYS RESULTS

This code is intended to process the output files generated by the code in the previous section, but can be easily modified for different ANSYS simulations. All results are saved as a MATLAB workspace containing 2D arrays of all six strain components and a vector containing the associated x- and y-values.

```
%% Program for processing files from ANSYS
%% Based on output files named "CQW_091813_1.txt", "CQW_091813_2".txt, etc.

clear all;
close all;

DataSetName = input('Enter name for data set: ','s');

warning('off','MATLAB:dispatcher:InexactCaseMatch')

Name = 'CQW_091813_';
FileType = '.txt';
NFiles = 300;           % Number of files
NLines = 301;
Width = 2.5;            % Width of problem space in mm

exx(1:NFiles,1:NLines) = 0;   %Pre-allocate strain matrices
eyy(1:NFiles,1:NLines) = 0;
ezz(1:NFiles,1:NLines) = 0;
exy(1:NFiles,1:NLines) = 0;
eyz(1:NFiles,1:NLines) = 0;
exz(1:NFiles,1:NLines) = 0;

for nn = 1 : NFiles

    FileName = strcat(Name,num2str(nn),FileType);
    fid = fopen(FileName);
    C = textscan(fid,'%s');
    DataCell = C{1};
    [M1,M2] = size(DataCell);
```

```
    NCount = 1;
    Skip = 1;

    for mm = 1 : M1

        CurrentString = DataCell{mm};

        if strcmp(CurrentString,'EPELXZ') && Skip == 1

            Skip = 0;

        elseif Skip == 0

            findDoubles = length(strfind(CurrentString,'E'));

            if findDoubles > 1

                CurrentString = strrep(CurrentString,'-0.',' -0.');
                x = sscanf(CurrentString,'%f %f');

                for qq = 1 : findDoubles

                    NumberList(NCount) = x(qq);
                    NCount = NCount + 1;

                end

            else

               NumberList(NCount) = str2num(CurrentString);
               NCount = NCount + 1;

            end
        end

    end

    NumberMatrix = vec2mat(NumberList,7);

    exx(nn,:) = NumberMatrix(:,2);
    eyy(nn,:) = NumberMatrix(:,3);
    ezz(nn,:) = NumberMatrix(:,4);
    exy(nn,:) = NumberMatrix(:,5);
    eyz(nn,:) = NumberMatrix(:,6);
    exz(nn,:) = NumberMatrix(:,7);

    fclose(fid);

end

Xpt = linspace(-0.5*Width,0.5*Width,NFiles);
Ypt = linspace(-0.5*Width,0.5*Width,NLines);
```

```
save(strcat(DataSetName,'.mat'),'exx','eyy','ezz','exy','eyz','exz','Xpt','Ypt');
```

APPENDIX D

TIME-AVERAGED TRAPPING

The idea of using a time-dependent spatially-inhomogeneous electric field to trap indirect excitons is partially inspired by the use of the time-orbiting potential (TOP) magnetic trapping geometry used in cold atom research. For atoms with a magnetic dipole moment, $\vec{\mu}$, the energy shift due to the presence of a static magnetic field, $\vec{B}$, is given simply by

$$\Delta E = -\vec{\mu} \cdot \vec{B}. \tag{D.1}$$

A quadrupolar magnetostatic trap profile is easily created using a pair of symmetric anti-Helmholtz coils; while this configuration provides tight confinement, loss from the center of the trap is high due to Majorana spin flip [145]. In the quadrupolar geometry, the minimum of the magnetic field is at the center of the trap, so atoms whose magnetic moment is opposite the direction of the field will feel a confining potential; atoms aligned with the field will be sitting on top of a potential hill and will be quickly expelled from the trap. Away from trap center, spin flip is suppressed due to the splitting between the two states. Near the center of the trap, where the two states are nearly degenerate, spin flip can be a significant source of loss [146].

The TOP trap is a variation on the static, quadrupolar trap that includes a magnetic field that rotates slowly in-plane. The time scale of the time-dependent field is designed to be long compared to the spin flip time, but short compared to the time scale associated with motion of atoms in the trap [145]. The atoms feel a time-averaged, harmonic trapping

potential with a energy gap that breaks the spin degeneracy at the center [147]. Due to the gap, spin flip near trap center is suppressed.

In the TOP configuration, the primary source of loss is associated with the sides of the trap. This can be an attractive feature, because higher kinetic energy particles are preferentially removed to from the trap, which tends to lower the average thermal energy of the trapped population [145]. It is easy to see how this is preferable to the static quadrupole trap, where particles at trap center - the coldest part of the population on average - are preferentially removed from the trap. The process of lowering the average energy of a system by preferentially removing high energy particles is known as evaporative cooling and is one of the major tools of cold atoms research.

As discussed in Chapter 2, a spatially inhomogeneous electrostatic trap is also characterized by a spatially dependent radiative lifetime. Indirect excitons are trapped by high electric field in the growth direction, which also corresponds to longer radiative lifetime (as discussed in Chapter 1). Therefore, it would be expected that some degree of evaporative cooling occurs naturally in electrostatic traps, due to the shorter lifetime along the trap periphery compared to at trap center. In practice, this benefit is likely reduced by the flattening of the trapping potential at high density. Evaporative cooling can also be introduced by altering the geometry of the trap, for example, by creating a trap with a lip, over which high energy particles can simply escape; this approach was applied to an electrostatic trap by Hammack et al. [148, 149].

Ultimately, there are two features of the TOP trap that the trapping technique discussed in this appendix attempts to mimic. First, during at least part of the cycle particles at the edges of the trap should be expelled - either by the trapping potential itself or due to radiative recombination. Second, the indirect exciton population should feel a time-averaged confinement potential that is at least 5-10 meV deep (the achievable density is largely limited by the trap flattening due to density-dependent blue shift).

One method that may achieve these goals is the introduction of a slowly varying, spatially-inhomogeneous electric field on top of an overall applied bias. An implementation of this approach is outlined in the following section.

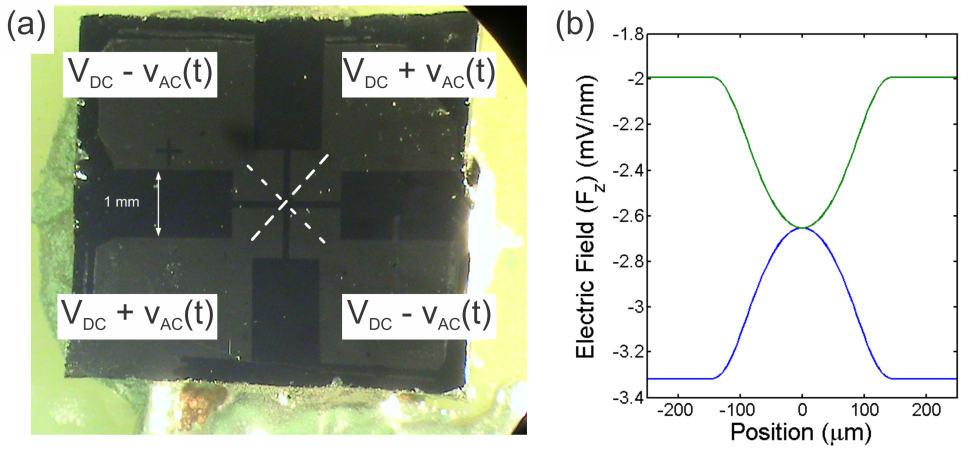

Figure 50: Image of a mounted sample with quadrupolar contacts under shown in (a). The four quadrants can be independently driven with AC signals of varying phase, shown is the case where opposing quadrants are 180° out of phase. In (b), the trapping and anti-trapping electric field profile along dotted lines is shown, calculated under assumptions that voltage is constant across metal pads and varies linearly between pads.

D.1 DEVICE

The quadrupolar trapping geometry, shown in Figure 50(a), was fabricated by lithographically patterning photoresist to cover the non-contacted region of the sample. The wafer it was taken from consisted of 14 nm CQWs separated by a 4 nm barrier, grown on an n-type substrate, and topped with a p-type capping layer. The sample was coated via e-beam evaporation with 5 nm of gold on top of 11 nm of titanium. The photoresist was then removed, leaving four independent, optically-transparent contacts. It can be seen in Figure 50(a), that the four contacts meet at a box in the center (with a side length of approximately 100 μm) which forms the trapping region.

The four quadrants can be independently driven by AC signals with a constant, DC offset. The DC offset is chosen to be larger than the amplitude of the AC signals; this insures that the AC signals alternately enhance and oppose the DC field. Depending on the relative phase of the four quadrants, a number of trapping geometries can be implemented.

The configuration discussed here is such that opposite quadrants are shorted to the same phase, while adjacent quadrants are 180° out of phase (this is the configuration shown in Figure 50(a)). This results in a geometry where the IX population is trapped along one axis and anti-trapped along the other. By flipping the trapping and anti-trapping direction back and forth on a time-scale faster than the response time of the IX diffusion rate, one might expect that the population will experience a time-averaged trapping potential. A plot of the expected electric field along the growth direction (F_z) along the two axes (shown by white, dotted lines in Figure 50(a)) is shown in Figure 50(b). The plot is calculated assuming a constant gradient of the potential in the region between the contacts, using 2D interpolation, and uses a DC bias of 2V with a modulation of 0.5 V. This would be the instance of strongest confinement for an AC signal of 1 V_{ptp} amplitude.

D.2 EXPERIMENTAL RESULTS

In the experimental results shown here, a quasi-steady state population of indirect excitons is introduced into the system by resonantly pumping the direct line. The excitation source is a chopped laser diode with a 50% duty cycle (4 μs / 8 μs). Due to the long radiative lifetime of indirect excitons, this chopping does not drastically decrease the steady state IX population, while minimizing heating. The series discussed here uses an overall 2 V DC bias with an AC signal of 1 V_{ptp} applied in the quadrupolar geometry discussed in Section D.1. The indirect exciton population was studied by observing the time-averaged luminescence (using an ungated ICCD).

The frequency-dependence of the luminescence profile was studied at low temperature (6 K). The primary goal was to look for evidence of enhanced trapping as a function of driving frequency. In the low-frequency limit, there is no reason to expect that any time averaged trapping will occur; the population will quickly diffuse out of the trapping area before the trapping direction switches and the population is pushed back towards the center. Signatures of enhanced trapping could include spatial narrowing, an increase in the intensity, or an increase in the density-dependent blue shift. For each image in the series, the IX population

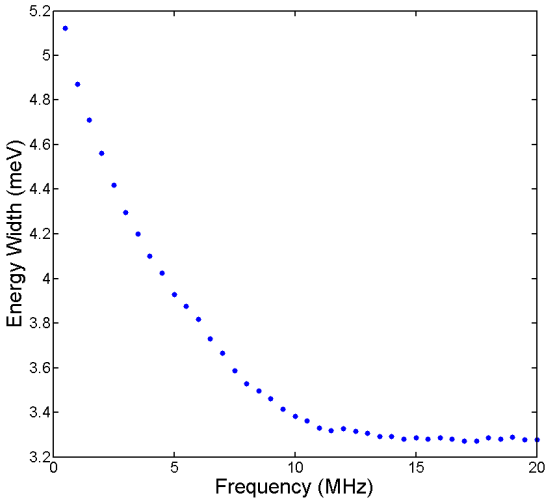

Figure 51: The measured energy broadening of the luminescence as a function of AC frequency. Based on a DC voltage of 2 V and AC signal of 1 V_{ptp} in the quadrupolar geometry.

was spectrally resolved along one of the trapping axes. The mean energy of the luminescence $\langle E \rangle$, the spectral FWHM ΔE, the peak intensity height of the cross-section, and the spatial FWHM were measured at each frequency value.

A plot of the energy width is shown in Figure 51 and a plot of the peak intensity is shown in Figure 52. A clear trend appears in the frequency dependence for both plots - the spectral width of the signal decreases with frequency as the peak intensity of the population increases. One possible interpretation of this behavior is that the voltage felt by the quantum wells is frequency dependent due to the characteristic charging time of the *p-i-n* structure. The insulating region of the structure will have some capacitance, which can be approximated using a simple planar capacitor model:

$$C = \frac{A\epsilon_{\mathrm{GaAs}}}{d} \tag{D.2}$$

where A is the area of the contact region - which is on the order of 1 mm^2 - and d is the thickness of the insulating region - which is around 700 nm. The expected capacitance according to this approximation is 0.2 nF. The relevant resistance will be be the contact

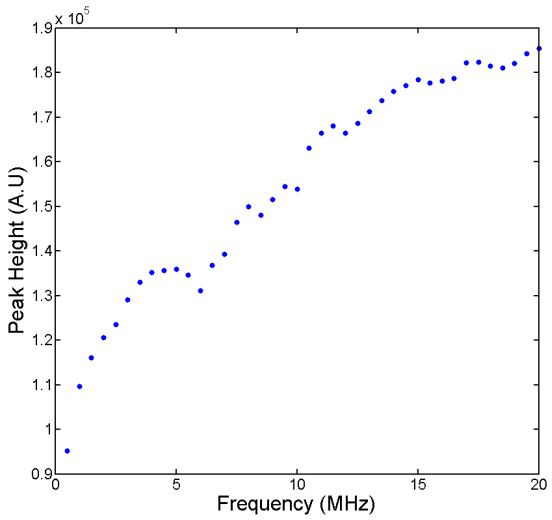

Figure 52: Measured intensity height of the spectrally-resolved luminescence as a function of AC frequency. Based on a DC voltage of 2 V and AC signal of 1 V_{ptp} in the quadrupolar geometry.

resistance to the metal pads; due to thin contact pads used this will be non-negligible, but is less than 100 Ω. The RC constant corresponds to a charging time of 50 ns and a characteristic frequency of about 50 MHz, so it is reasonable to expect that the charging time is not significant in the ≤ 20 MHz frequency range. Furthermore, attempts to fit the response to an RC voltage divider,

$$\left|\frac{v_S}{v_{in}}\right| = \frac{1}{1+\omega^2 R^2 C^2}, \tag{D.3}$$

where v_S is the voltage across the sample and v_{in} is the input voltage, resulted in a very poor fit. Instead, the most accurate fit was to a decaying exponential:

$$\Delta E = \Delta E_{HF} + (\Delta E_{LF} - \Delta E_{HF}) \exp\left[-\frac{f}{f_0}\right] \tag{D.4}$$

with the high-frequency energy shift ΔE_{HF}, the low-frequency energy shift ΔE_{LF}, and a characteristic frequency f_0 as fitting parameters. A non-linear least squares fit to this model gave (with 95% confidence intervals) $\Delta E_{HF} = 3.23$ meV ± 0.02 meV, $\Delta E_{LF} = 5.34$ meV ±

0.07 meV, and $f_0 = 231$ kHZ $\pm$ 6.4 kHz. A characteristic frequency of 230 kHz corresponds to a time scale of about 4 μs; the relevance of this time scale will be discussed in more detail in the following section.

In the quadrupolar trapping geometry, the net additional bias due to the AC voltage should be zero. At trap center, the potential should be approximately equal to the DC voltage offset at all times due to the symmetry of the AC bias. However, this smearing of the energy at low frequency does seem to indicate that the population at trap center is adiabatically shifting back and forth with time. An imbalance in the contact resistance of the quadrupolar contacts could introduce an asymmetry in the trapping potential, which could result in a shift at trap center.

One can see from Figure 52, that the maximum intensity of the population exhibits roughly the opposite behavior of the energy width. Assuming the total population is independent of frequency, it makes sense that the spectrally-resolved peak intensity would be larger when the the luminescence is less smeared out over energy. It is worth noting from Figure 52 that there is a distinct dip in the intensity around f = 6 MHz, while there is no corresponding feature in the frequency-dependence of the energy width. A plot of the mean energy, shown in Figure 53, also shows that the mean energy is the lowest between 5-10 MHz driving frequency. The mean energy shift can be indicative of the time-averaged density at trap-center (due to the density dependent blue shift). Both features could indicate that the steady-state population may be lower at trap center.

The spatial width of the population did not change dramatically with frequency; instead, it was observed to remain fixed within the measurement noise at a FWHM of around 200 μm $\pm$ 10 μm. Note that this is also roughly the size of the contact window, so it seems there does not seem to be significant confinement in this regime.

It does not appear from these results that there was any frequency-dependent enhancement of the population density, which seems to indicate that trapping did not occur. A time-dependent drift-diffusion model will be used in the following section to study the quadrupolar geometry and provide some perspective for the experimental results.

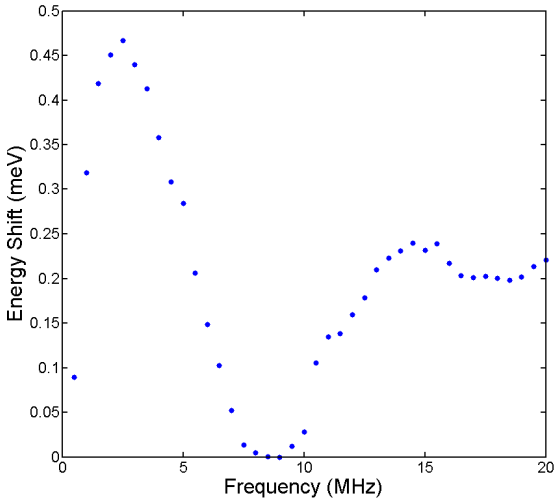

Figure 53: The measured mean energy shift of the luminescence as a function of AC frequency, defined such that the minimum value is zero. Based on a DC voltage of 2 V and AC signal of 1 V_{ptp} in the quadrupolar geometry.

D.3 NUMERICAL MODELING

Given that no drastic effects were observed in the luminescence of the IX population, it was necessary to gain a deeper understanding of the trap dynamics before spending more time experimentally exploring the parameter space. The indirect exciton population in a time-varying AC trap should be reasonably modeled using the classical drift-diffusion model with a time-dependent potential and radiative decay:

$$\frac{\partial n}{\partial t}(x,y,t) = \nabla \cdot (D \nabla n(x,y,t)) + \nabla \cdot (\mu \nabla U(x,y,t)) - \frac{n(x,y,t)}{\tau_{\mathrm{Rad}}(x,y)}. \tag{D.5}$$

The diffusion constant of indirect excitons in coupled-quantum wells was measured by Z. Vörös [113] for a variety of quantum well widths. Therein it is shown that the diffusion constant scales as well-width to the sixth-power, due to the effect of roughness scattering being more prevalent for thin-wells. In Vörös' work, the diffusion constant was found to be 9.4 cm^2/s for 14 nm quantum wells and 2.08 cm^2/s for 12 nm quantum wells.

In the classical regime, mobility μ is closely related to the diffusion constant via the Einstein relation:

$$\mu = \frac{D}{kT}. \tag{D.6}$$

In the regime where quantum degeneracy is significant, this expression must be modified (see works by Ivanov [150, 151]). For the purposes of the calculations discussed below only the classical limit will be considered. Quantum degeneracy introduces a density dependence to the mobility, which significantly complicates the model. The purpose of this calculation is to examine whether high density can be achieved at all; thus, it is reasonable to start with the classical regime. If this geometry does not provide time-averaged trapping within the classical regime, it is unlikely that it will be possible to rech a high enough density to observe quantum degeneracy.

To approximate the time-scale associated with motion in the trap discussed above, one can consider roughly how long it would take an indirect exciton to drift from trap center to the periphery under an appropriate potential gradient. For a change in potential, ΔU [1] , across a fixed distance, Δx, at temperature T the relevant time scale can be approximated as:

$$\Delta t \approx \frac{\Delta x^2 k_B T}{D \Delta U}. \tag{D.7}$$

Using $\Delta x \approx 50$ μm, $T = 10$ K, the value 9.4 cm^2/s from [113] for the diffusion constant, and a potential change of 10 meV from the center of the trap to the periphery, this expression predicts a time scale of approximately 230 ns, corresponding to a frequency of about 4 MHz. Recall from the discussion of experimental results in Section D.2 that the indirect population response to the AC bias seemed to depend on a characteristic frequency scale of 230 kHz; however, there were also features in the data shown in Figures 52 and 53 in the vicinity of 6 MHz.

The time-dynamics of the density profile, $n(x, y, t)$, were calculated using a finite-difference calculation of the drift-diffusion model in D.5, with a grid spacing of 1 μm and a variable

[1] Using a constant drift force, $\Delta U/\Delta x$, is not strictly correct, because the potential is shown to be parabolic in Figure 50- not linear. But for the sake of an order-of magnitude calculation, the average potential gradient from the center to the edge of the trap is used as an approximation.

time step. The initial population is localized within 1 μm of the origin and allowed to evolve with time. As discussed below, both density-dependent blue shift and radiative decay are ignored in the model; these assumptions, while clearly not a valid representation of the system, provide the simplest scenario to calculate the upper-bound of confinement (as both processes reduce the effectiveness of the trap). It will be shown that, even by making these assumptions, this configuration does not provide favorable conditions for confinement, making it unnecessary to develop a more rigorous model.

For the purpose of calculating the electric field, the electric potential was assumed to be constant across the contact surfaces. In the region between the contacts, the potential was calculated using a 2D linear interpolation. The spatial scale of the gap between the top contacts is large (100 μm) compared to the thickness of the insulating region (around 1 μm), so it is expected that the in-plane electric field induced by the varying potential will be small compared to the field in the growth direction. The spatial thickness of the p-type capping layer is expected to smear out the spatial profile of the trapping potential, but this layer is typically only 100 nm thick and not a perfect conductor, so the potential profile will mostly be intact directly above the insulating region.

As an additional simplifying assumption, radiative decay will also be ignored. The lifetime is strongly dependent on electric field, so it is expected that it could vary by an order of magnitude as the electric field varies. This might be a useful property in terms of evaporative cooling, but if the trapping potential is too leaky to maintain a large steady-state population, additional sources of loss will not improve the situation. In other words, a model which excludes radiative loss shows the upper limit of trapping capability.

Another simplifying assumption is to ignore the density-dependent blue shift. In principle, this can be modeled by adding a term to the potential $U(x, y, t)$ that is proportional to the density; however, at high density the non-linearity of this term introduces numerical instability issues and slows down the calculation. Density-dependent blue shift serves primarily to flatten out the trapping potential, so it is expected that confinement will be strictly worse in the high-density limit than it is at low density.

There are a few metrics one can use to gauge the effectiveness of a trap. In Figures 54 and 55 the simulated population average of the radius-squared from the center of the trap

is plotted with respect to time, as a function of AC frequency and trap depth, respectively. It can easily be shown that for free diffusion in a two-dimensional system with diffusion constant D, this quantity varies linearly with time:

$$\langle r(t)^2 \rangle = 4Dt. \tag{D.8}$$

This is also a good way to test the validity of the numerical model; for small trapping potential, the model should approach the result for free-diffusion.

One can see from the frequency series in Figure 54 that the time-dependence of $\langle r^2 \rangle$ approaches the untrapped case as frequency is increased. Likewise, in Figure 55, the value of $\langle r^2 \rangle$ varies linearly with time as the potential is decreased to zero. However, both plots also reveal that the value of $\langle r^2 \rangle$ is always greater than the free diffusion case for all calculated values of the trapping potential depth, U_0, and potential frequency. This suggests that this geometry will not work well for trapping; on average, the population spreads out more quickly in this potential than in the untrapped case.

However, one other metric worth looking at is the peak density. Shown in Figure 56 is the peak density of the population as a function of time, for a range of trap depths. While the lower bound of the max-density curves for the trapped case are universally lower than the untrapped ($U_0 = 0$ meV) case, the trapped curves do exhibit instantaneous peak densities which are significantly larger than the untrapped case. Physically, this occurs when the AC component of the potential flips and the untrapped axis becomes the trapped axis. The population that was initially spread out in this direction is quickly forced back into the center. This effect may have some merit, in the sense that it could be used to achieve high peak density in a trap.

It is clear that even with extremely liberal assumptions, this configuration will not provide time-averaged confinement without some re-design of the geometry. From inspection of the population dynamics, it appears that the primary issue is the flat potential profile outside of the trap. There is a reasonable trapping potential in the central region, but once excitons diffuse outside of this region (under the plates) they are completely untrapped.

One approach to fixing this issue would be to increase the size of the central region. Specifically, if the size of the trapping potential is larger than the typical diffusion length of

an IX during its lifetime, it is expected that the leakage out of the trap will be much smaller. The gap between the contacts can also be problematic, because they form untrapped channels which provide an additional source of loss. Minimizing the size of this gap (currently 50 μ m) would also be an improvement.

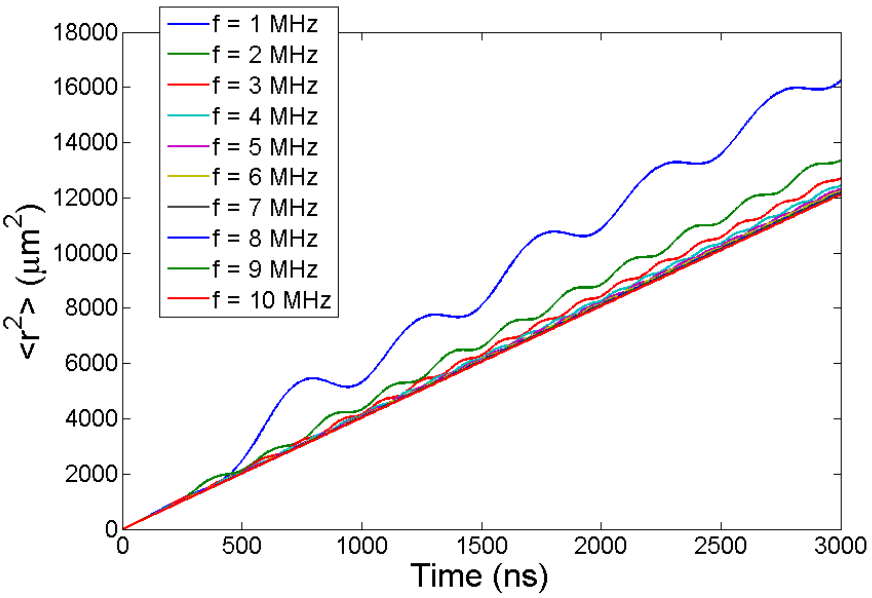

Figure 54: Population average of r^2 as a function of time, modeled using finite-difference calculation of drift-diffusion model discussed in text. Initial population is essentially delta function at the center (spot size small compared to trap dimensions). Trap depth is fixed at 7 meV, while frequency of oscillation is varied.

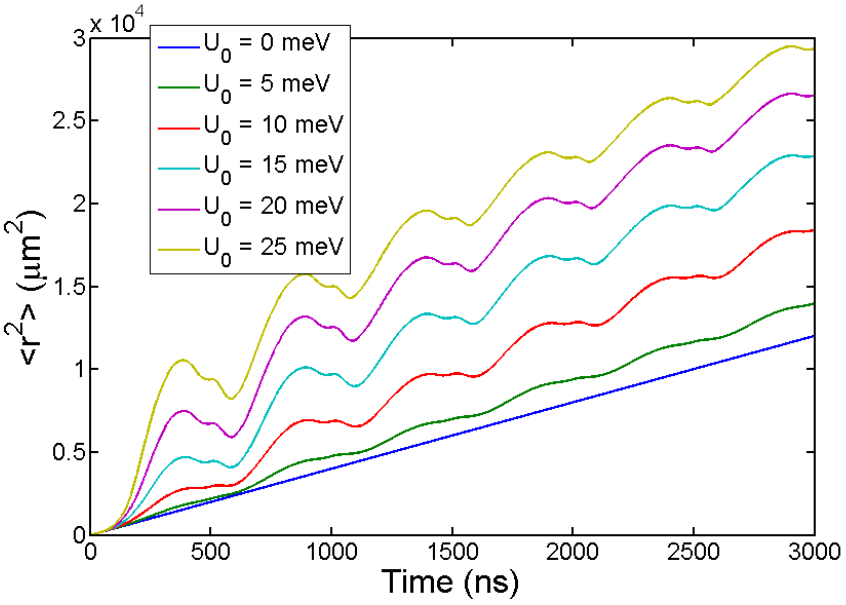

Figure 55: Population average of r^2 as a function of time, modeled using finite-difference calculation of drift-diffusion model discussed in text. Frequency is fixed at 1 MHz, while trap depth is varied.

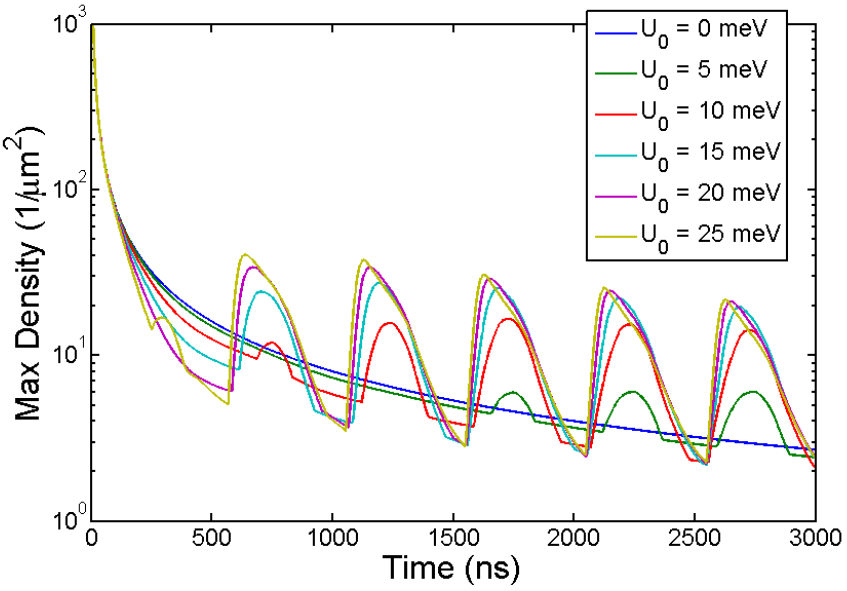

Figure 56: Peak density as a function of time, modeled using finite-difference calculation of drift-diffusion model discussed in text. Oscillation frequency is fixed at 1 MHz, while trap depth is varied.

BIBLIOGRAPHY

[1] S. Chuang, *Physics of Photonic Devices (2nd Ed.)*. John Wiley and Sons, Inc., 2009.

[2] S. Bose, "Planck's law and light quantum hypothesis," *Zeitschrift für Physik*, vol. 26, no. 178, 1924.

[3] R. Pathria, *Statistical Mechanics (2nd Ed.)*. Elsevier, 1996.

[4] A. Einstein, "Quantum theory of the monatomic ideal gas, part II," *Sitzungberichte der Preussischen Akademie der Wissenschaften (Berlin), Physikalischmathematische Klasse*, p. 3, 1925.

[5] A. Griffin, "A brief history of our understanding of BEC: From Bose to Beliaev," in *Bose-Einstein Condensation in Atomic Gases* (M. Inguscio, S. Stringari, and C. Wieman, eds.), p. 1, IOS Press, 1999.

[6] P. Kapitza, "Viscosity of helium below the λ-point," *Nature*, vol. 141, 1938.

[7] A. Misener and J. Allen, "Flow of liquid helium-II," *Nature*, vol. 142, 1938.

[8] F. London, "The λ-phenomenon of liquid helium and the Bose-Einstein degeneracy," *Nature*, vol. 141, 1938.

[9] L. Tisza, "Transport phenomena in helium II," *Nature*, vol. 141, 1938.

[10] E. Lifschitz and L. Pitaevskii, *Statistical Physics, Part 2*, vol. 9. Butterworth-Heinemann, 1980.

[11] P. Sokol, "BEC in liquid helium," in *Bose-Einstein Condensation* (A. Griffin, D. Snoke, and S. Stringari, eds.), Cambridge University Press, 1995.

[12] H. Glyde, "Condensate, momentum distribution, and final-state effects in liquid ^4He," *Physical Review B*, vol. 62, no. 21, 2000.

[13] A. Wyatt, "Evidence of Bose-Einstein codensate in liquid ^4He from quantum evaporation," *Nature*, vol. 391, 1998.

[14] W. Buckel and R. Kleiner, *Superconductivity: Fundamentals and Application (2nd Ed.)*. Wiley-VCH, 2004.

[15] J. Matricon and G.Waysand, *The Cold Wars: A History of Superconductivity*. Rutgers University Press, 2003.

[16] W. Meissner and R. Ochsenfeld, "Ein neuer effekt bei eintritt der supreleitfähigkeit," *Naturwissenschaften*, vol. 21, no. 44, 1933.

[17] F. London and H. London, "The electromagnetic equations of the supraconductor," *Proceedings of the Royal Society A*, vol. 149, no. 866, 1935.

[18] J. Bardeen, L. Cooper, and J. Schrieffer, "Theory of superconductivity," *Physical Review*, vol. 108, no. 5, 1957.

[19] A. Leggett, *Quantum Liquids*. Oxford University Press, 2008.

[20] A. Leggett and S. Zhang, "The BEC-BCS crossover: Some history and some general observations," in *The BCS-BEC Crossover and the Unitary Fermi Gas* (W. Zwerger, ed.), Springer-Verlag, 2012.

[21] J. Bednorz and K. Müller, "Possible high T_C superconductivity in the Ba-La-Cu-O system," *Zeitschrift für Physik B*, vol. 64, no. 2, 1986.

[22] C. Chu, L. Gao, F. Chen, Z. Huang, R. Meng, and Y. Xue, "Superconductivity above 150 K in $HgBa_2Ca_2Cu_3O_{8+\delta}$ at high pressures," *Nature*, vol. 365, no. 323, 1993.

[23] P. Lee, N. Nagaosa, and X. Wen, "Doping a Mott insulator: Physics of high-temperature superconductivity," *Reviews of Modern Physics*, vol. 78, no. 1, 2006.

[24] P. Anderson, "Twenty-five years of high-temperature superconductivity - a personal review," *Journal of Physics: Conference Series*, vol. 449, 2013.

[25] C. Hecht, "The possible superfluid behaviour of hydrogen atom gases and liquids," *Physica*, vol. 25, no. 7, 1959.

[26] W. Stwalley and L. Nosanow, "Possible "new" quantum systems," *Physical Review Letters*, vol. 36, no. 15, 1976.

[27] E. Cornell and C. Wieman, "Bose Einstein condensation in a dilute gas: The first 70 years and some recent experiments," in *Nobel Lectures in Physics (2001-2005)* (G. Ekspong, ed.), 2008.

[28] J. Doyle, J. Sandberg, I. Yu, C. Cesar, D. Kleppner, and T. Greytak, "Hydrogen in the submillikelvin regime: Sticking probability on superfluid ^4He," *Physical Review Letters*, vol. 67, no. 5, 1991.

[29] W. Ketterle, D. Durfee, and D. Stamper-Kurn, "Making, probing and understanding Bose-Einstein condensates," in *Bose-Einstein Condensation in Atomic Gases, Proceedings of the International School of Physics 'Enrico Fermi', Course CXL* (M. Inguscio, S. Stringari, and C. Wieman, eds.), IOS Press, 1999.

[30] M. Anderson, J. Ensher, M. Matthews, C. Wieman, and E. Cornell, "Observation of Bose-Einstein condensation in a dilute atomic vapor," *Science*, vol. 269, no. 5221, 1995.

[31] K. Davis, M. Mewes, M. Andrews, N. van Druten, D. Durfee, D. Kurn, and W. Ketterle, "Bose-Einstein condensation in a gas of sodium atoms," *Physical Review Letters*, vol. 75, no. 22, 1995.

[32] B. Laikhtman, "Are excitons really bosons?," *Journal of Physics: Condensed Matter*, vol. 19, no. 29, 2007.

[33] I. Blatt, K. Boer, and W. Brandt, "Bose-Einstein condensation of excitons," *Physical Review*, vol. 126, no. 5, 1962.

[34] S. Moskalenko, "Reversible opto-hydrodynamical phenomena in a non-ideal exciton gas," *Fiz. Tverd. Tela*, vol. 4, no. 276, 1962.

[35] D. Snoke and G. Kavoulakis, "Bose-Einstein condensation of excitons in Cu_2O: Progress over thirty years," *Reports on Progress in Physics*, vol. 77, no. 11, 2014.

[36] H. Kuroda, S. Shionoya, H. Saito, and E. Hanamura, "Bose condensation of excitonic molecules in CdSe," *Journal of the Physical Society of Japan*, vol. 35, no. 2, 1973.

[37] W. Johnston, Jr. and K. Shaklee, "Considerations relevant to Bose condensation of excitonic molecular in CdSe," *Solid State Communications*, vol. 15, no. 1, 1974.

[38] N. Peyghambarian, L. Chase, and A. Mysyrowicz, "Bose-Einstein statistical properties and condensation of excitonic molecules in CuCl," *Physical Review B*, vol. 27, 1983.

[39] M. Hasuo, N. Nagasawa, T. Itoh, and A. Mysyrowicz, "Progress in Bose-Einstein condensation of biexcitons in CuCl," *Physical Review Letters*, vol. 70, no. 9, 1993.

[40] S. Moskalenko and D. Snoke, *Bose-Einstein Condensation of Excitons and Biexcitons*. Cambridge University Press, 2000.

[41] A. Mysyrowicz, D. Hulin, and A. Antonetti, "Long exciton lifetime in Cu_2O," *Physical Review Letters*, vol. 43, no. 15, 1979.

[42] H. Stolz, R. Schwartz, F. Kieseling, S. Som, M. Kaupsch, S. Sobkowiak, D. Semkat, N. Naka, T. Koch, and H. Fehske, "Condensation of excitons in Cu_2O at ultracold temperatures: Experiment and theory," *New Journal of Physics*, vol. 14, no. 10, 2012.

[43] K. Yoshioka, E. Chae, and M. Kuwata-Gonokami, "Transition to a Bose-Einstein condensate and relaxation explosion of excitons at sub-Kelvin temperatures," *Nature Communications*, vol. 2, 2011.

[44] R. Balili, V. Hartwell, D. Snoke, L. Pfeiffer, and K. West, "Bose-Einstein condensation of microcavity polaritons in a trap," *Science*, vol. 316, no. 5827, 2007.

[45] H. Deng, G. Solomon, R. Hey, K. Ploog, and Y. Yamamoto, "Spatial coherence of a polariton condensate," *Physical Review Letters*, vol. 99, no. 12, 2007.

[46] C. Lai, N. Kim, S. Utsunomiya, G. Roumpos, H. Deng, M. Fraser, T. Byrnes, P. Recher, N. Kumada, T. Fujisawa, and Y. Yamamoto, "Coherent zero-state and π-state in an exciton-polariton condensate array," *Nature Letters*, vol. 450, no. 7169, 2007.

[47] B. Nelsen, G. Liu, M. Steger, D. Snoke, R. Balili, K. West, and L. Pfeiffer, "Dissipationless flow and sharp threhold of a polariton condensate with long lifetime," *Physical Review X*, vol. 3, no. 4, 2013.

[48] S. Adachi, *GaAs and Related Materials: Bulk Semiconducting and Superlattice Properties*. World Scientific Publishing, 1994.

[49] R. Winkler, *Spin-Orbit Coupling Effects in Two-Dimensional Electron and Hole Systems*. Springer-Verlag, 2003.

[50] K. Maezawa, T. Mizutani, and F. Yanagawa, "Barrier height in indirect bandgap AlGaAs/GaAs hetero-junction determined with n-semiconductor / insulator / semiconductor diodes," *Japanese Journal of Applied Physics*, vol. 25, no. 7A, 1986.

[51] D. Snoke, *Solid State Physics: Essential Concepts*. Addison-Wesley, 2009.

[52] S. Nam, D. Reynolds, C. Litton, R. Almassy, T. Collins, and C. Wolfe, "Free-exciton energy spectrum in GaAs," *Physical Review B*, vol. 13, 1976.

[53] S. Tarucha and H. Okamoto, "Exciton binding energy in GaAs quantum wells deduced from magneto-optical absorption measurement," *Solid State Communications*, vol. 52, no. 9, 1984.

[54] R. Miller, D. Kleinman, W. Tsang, and A. Gossard, "Observation of the excited level of excitons in GaAs quantum wells," *Physical Review B*, vol. 24, 1981.

[55] K. Köhler, H. Polland, and L. Schultheis, "Photoluminescence of two-dimensional excitons in an electric field: Lifetime enhancement and field ionization in GaAs quantum wells," *Physical Review B*, vol. 38, 1988.

[56] D. Miller, D. Chemla, T. Damen, A. Gossard, W. Wiegmann, T. Wood, and C. Burrus, "Band-edge electroabsorption in quantum well structures: The quantum-confined Stark effect," *Physical Review Letters*, vol. 53, no. 22, 1984.

[57] H. Polland, L. Schultheis, J. Kuhl, E. Göbel, and C. Tu, "Lifetime enhancement of two-dimensional excitons by the quantum-confined Stark effect," *Physical Review Letters*, vol. 55, no. 23, 1985.

[58] Y. Takahashi, Y. Kato, S. Kano, S. Fukatsu, and Y. Shiraki, "The effect of electric field on the excitonic states in coupled quantum well structures," *Journal of Applied Physics*, vol. 76, no. 4, 1994.

[59] P. Harrison, *Quantum Wells, Wires and Dots.* Wiley, 2009.

[60] M. Szymańska, P. Littlewood, and R. Needs, "Excitons in T-shaped quantum wires," *Physical Review B*, vol. 63, no. 20, 2001.

[61] M. Szymanska and P. Littlewood, "Excitonic binding in coupled quantum wells," *Physical Review B*, vol. 67, no. 19, 2003.

[62] N. Sinclair, J. Wuenschell, Z. Vörös, B. Nelsen, D. Snoke, M. Szymanska, A. Chin, J. Keeling, L. Pfeiffer, and K. West, "Strain-induced darkening of trapped excitons in coupled quantum wells at low temperature," *Physical Review B*, vol. 83, no. 25, 2011.

[63] D. Oberli, J. Shah, T. Damen, C. Tu, T. Chang, D. Miller, J. Henry, R. Kopf, N. Sauer, and A. DiGiovanni, "Direct measurement of resonant and nonresonant tunneling times in asymmetric coupled quantum wells," *Physical Review B*, vol. 40, 1989.

[64] K. Leo, J. Shah, J. Gordon, T. Damen, D. Miller, C. Tu, and J. Cunningham, "Effect of collisions and relaxation on coherent resonant tunneling: Hole tunneling in $GaAs/Al_xGa_{1-x}As$ double-quantum-well structures," *Physical Review B*, vol. 42, 1990.

[65] Z. Vörös, R. Balili, D. Snoke, L. Pfeiffer, and K. West, "Long-distance diffusion of excitons in double quantum well structures," *Physical Review Letters*, vol. 94, no. 22, 2005.

[66] G. Baym and C. Pethick, "Ground-state properties of magnetically trapped Bose-condensed rubidium gas," *Physical Review Letters*, vol. 76, no. 1, 1996.

[67] O. Berman, Y. Lozovik, and D. Snoke, "Theory of Bose-Einstein conensation and superfluidity of two-dimensional polaritons in an in-plane harmonic potential," *Physical Review B*, vol. 77, no. 15, 2008.

[68] V. Berezinskii, "Destruction of long-range order in one-dimensional and two-dimensional systems possessing a continuous symmetry group II: Quantum systems," *Soviet Physics JETP*, vol. 34, no. 3, 1972.

[69] J. Kosterlitz and D. Thouless, "Ordering, metastability, and phase transitions in two-dimensional systems," *Journal of Physics C*, vol. 6, no. 7, 1973.

[70] P. Cladeé, C. Ryu, A. Ramanathan, K. Helmerson, and W. Phillips, "Observation of a 2D Bose gas: From thermal to quasicondensate to superfluid," *Physical Review Letters*, vol. 102, no. 17, 2009.

[71] V. Schweikhard, S. Tung, and E. Cornell, "Vortex proliferation in the Berezinskii-Kosterlitz-Thouless regime on a two-dimensional lattice of Bose-Einstein condensates," *Physical Review Letters*, vol. 99, no. 3, 2007.

[72] G. Roumpos, M. Lohse, W. Nitsche, J. Keeling, M. Szymańska, P. Littlewood, A. Löffler, S. Höfling, L. Worschech, A. Forchel, and Y. Yamamoto, "Power-law decay of the spatial correlation function in exciton-polariton condensates," *Proceedings of the National Academy of Sciences*, vol. 109, no. 17, 2012.

[73] A. High, A. Thomas, G. Grosso, M. Remeika, A. Hammack, A. Meyertholen, M. Fogler, L. Butov, M. Hanson, and A. Gossard, "Trapping indirect excitons in a GaAs quantum-well structure with a diamond-shaped electrostatic trap," *Physical Review Letters*, vol. 103, no. 8, 2009.

[74] A. Gärtner, D. Schuh, A. Holleitner, and J. Kotthaus, "Loading indirect excitons into an electrostatic trap formed in coupled GaAs quantum wells," *Physica E*, vol. 40, no. 6, 2008.

[75] R. Rapaport, G. Chen, S. Simon, O. Mitrofanov, L. Pfeiffer, and P. Platzman, "Electrostatic traps for dipolar excitons," *Physical Review B*, vol. 72, no. 7, 2005.

[76] R. Markiewicz, J. Wolfe, and C. Jeffries, "Strain-confined electron-hole liquid in germanium," *Physical Review B*, vol. 15, no. 4, 1977.

[77] P. Gourley and J. Wolfe, "Thermodynamics of excitonic molecules in silicon," *Physical Review B*, vol. 20, no. 8, 1979.

[78] V. Negoita, D. Snoke, and K. Eberl, "Stretching quantum wells: A method for trapping free carriers in GaAs heterostructures," *Applied Physics Letters*, vol. 75, no. 14, 1999.

[79] L. Landau and E. Lifschitz, *Theory of Elasticity (3rd Ed.)*. Elsevier, 1986.

[80] R. Balili, B. Nelsen, D. Snoke, R. Reid, L. Pfeiffer, and K. West, "Huge splitting of polariton states in microcavities under stress," *Physical Review B*, vol. 81, no. 12, 2010.

[81] V. Popov, *Contact Mechanics and Friction: Physical Principles and Applications*. Springer-Verlag, 2010.

[82] S. Sze, *Semiconductor Sensors*. Wiley-Interscience, 1994.

[83] J. Davis, *Tensile Testing (2nd Ed.)*. ASM International, 2004.

[84] B. Nelsen, *Polariton Condensates in a Trap and Photon Lasing in Two-Dimensional Semiconductor Microcavities*. PhD thesis, University of Pittsburgh, 2012.

[85] E. Ivchenko, *Optical Spectroscopy of Semiconductor Nanostructures*. Alpha Science International, 2005.

[86] N. Sinclair, *Luminescence Darkening of Strain-Trapped Excitons in Coupled Quantum Wells*. PhD thesis, University of Pittsburgh, 2014.

[87] D. Snoke, "Dipole excitons in coupled quantum wells: Towards an equilibruim exciton condensate," in *Quantum Gases: Finite Temperature and Non-equilibrium Dynamics* (N. Proukakis, S. Gardiner, M. Davis, and M. Szymańska, eds.), vol. 1 of *Cold Atoms*, ch. 28, Imperial College Press, 2013.

[88] J. Kash, M. Zachau, E. Mendez, and J. Hong, "Fermi-Dirac distribution of excitons in coupled quantum wells," *Physical Review Letters*, vol. 66, no. 17, 1991.

[89] I. Lerner and Y. Lozovik, "Two-dimensional electron-hole system in a strong magnetic field as an almost ideal exciton gas," *JETP*, vol. 53, no. 4, 1981.

[90] Y. Kuramoto and C. Horie, "Two-dimensional excitonic phase in strong magnetic fields," *Solid State Communications*, vol. 25, no. 9, 1978.

[91] L. Butov, A. Ivanov, A. Imamoglu, P. Littlewood, A. Shashkin, V. Dolgopolov, K. Campman, and A. Gossard, "Stimulated scattering of indirect excitons in coupled quantum wells: Signature of a degenerate Bose-gas of excitons," *Physical Review Letters*, vol. 86, no. 24, 2001.

[92] L. Butov and A. Filin, "Anomalous transport and luminescence of indirect excitons in AlAs/GaAs coupled quantum wells as evidence for exciton condensation," *Physical Review B*, vol. 58, 1998.

[93] R. Rapaport, G. Chen, and S. Simon, "Nonlinear dynamics of a dense two-dimensional dipolar exciton gas," *Physical Review B*, vol. 73, no. 3, 2006.

[94] D. Snoke, S. Denev, Y. Liu, L. Pfeiffer, and K. West, "Long-range transport in excitonic dark states in coupled quantum wells," *Nature*, vol. 418, 2002.

[95] L. Butov, A. Gossard, and D. Chemla, "Macroscopically ordered state in an exciton system," *Nature*, vol. 418, 2002.

[96] D. Snoke, Y. Liu, S. Denev, L. Pfeiffer, and K. West, "Luminescence rings in quantum well structures," *Solid State Communications*, vol. 127, no. 2, 2003.

[97] R. Rapaport, G. Chen, D. Snoke, S. Simon, L. Pfeiffer, K. West, Y. Liu, and S. Denev, "Charge separation of dense two-dimensional electron-hole gases: Mechanism for exciton ring pattern formation," *Physical Review Letters*, vol. 92, no. 11, 2004.

[98] L. Butov, A. Gossard, and D. Chemla, "Macroscopically ordered state in an exciton system," *Nature*, vol. 418, 2002.

[99] J. Wilkes, E. Muljarov, and A. Ivanov, "Drift-diffusion model of the fragmentation of the external ring structure in the photoluminescence pattern emitted by indirect excitons in coupled quantum wells," *Physical Review Letters*, vol. 109, no. 18, 2012.

[100] A. High, J. Leonard, A. Hammack, M. Fogler, L. Butov, A. Kavokin, K. Campman, and A. Gossard, "Spontaneous coherence in a cold exciton gas," *Nature*, vol. 483, 2012.

[101] A. High, J. Leonard, M. Remeika, L. Butov, M. Hanson, and A. Gossard, "Condensation of excitons in a trap," *Nano Letters*, vol. 12, no. 5, 2012.

[102] D. Semkat, S. Sobkowiak, G. Manzke, and H. Stolz, "Comment on 'condensation of excitons in a trap'," *Nano Letters*, vol. 12, no. 9, 2012.

[103] A. High, J. Leonard, M. Remeika, L. Butov, M. Hanson, and A. Gossard, "Reply to "comment on 'condensation of excitons in a trap"'," *Nano Letters*, vol. 12, no. 10, 2012.

[104] J. Repp, G. Schinner, E. Schubert, A. Rai, D. Reuter, A. Wieck, U. Wurstbauer, J. Kotthaus, and A. Holleitner, "Confocal shift interferometry of coherent emission from trapped dipolar excitons," *arXiv preprint arXiv:1411.5358*, 2014.

[105] M. Alloing, M. Beian, M. Lewenstein, D. Fuster, Y. González, L. Gonzaález, R. Combescot, M. Combescot, and F. Dubin, "Evidence for a Bose-Einstein condensate of excitons," *Europhysics Letters*, vol. 107, no. 1, 2014.

[106] Y. Shilo, K. Cohen, B. Laikhtman, K. West, L. Pfeiffer, and R. Rapaport, "Particle correlations and evidence for dark state condensation in a cold dipolar exciton fluid," *Nature Communications*, vol. 4, 2013.

[107] M. Combescot, O. Betbeder-Matibet, and R. Combescot, "Bose-Einstein condensation in semiconductors: The key role of dark excitons," *Physical Review Letters*, vol. 99, no. 17, 2007.

[108] R. Combescot and M. Combescot, ""Gray" BCS condensate of excitons and internal Josephson effect," *Physical Review Letters*, vol. 109, no. 2, 2012.

[109] A. Larionov and V. Timofeev, "Coherence and spin relaxation of interwell excitons in GaAs/AlGaAs coupled quantum wells," *International Journal of Nanoscience*, vol. 6, no. 03n04, 2007.

[110] V. Timofeev and A. Gorbunov, "Collective state of the Bose gas of interacting dipolar excitons," *Journal of Applied Physics*, vol. 101, no. 8, 2007.

[111] A. Gorbunov, V. Timofeev, D. Demin, and A. Dremin, "Two-photon correlations of luminescence at the Bose-Einstein condensation of dipolar excitons," *JETP Letters*, vol. 90, no. 2, 2009.

[112] Z. Vörös, D. Snoke, L. Pfeiffer, and K. West, "Trapping excitons in a two-dimensional in-plane harmonic potential: Experimental evidence for equilibration of indirect excitons," *Physical Review Letters*, vol. 97, no. 1, 2006.

[113] Z. Vörös, *Interaction of Excitons in Two-Dimensional Potentials*. PhD thesis, University of Pittsburgh, 2008.

[114] Y. Lozovik and O. Berman, "Phase transitions in a system of two coupled quantum wells," *JETP Letters*, vol. 64, no. 8, 1996.

[115] B. Laikhtman and R. Rapaport, "Exciton correlations in coupled quantum wells and their luminescence blue shift," *Physical Review B*, vol. 80, no. 19, 2009.

[116] R. Zimmermann and C. Schindler, "Exciton-exciton interaction in coupled quantum wells," *Solid State Communications*, vol. 144, no. 9, 2007.

[117] Z. Vörös, D. Snoke, L. Pfeiffer, and K. West, "Direct measurement of exciton-exciton interaction energy," *Physical Review Letters*, vol. 103, no. 1, 2009.

[118] L. Andreani, A. Pasquarello, and F. Bassani, "Hole subbands in strained GaAs-$Ga_{1-x}Al_xAs$ quantum wells: Exact solution of the effective-mass equation," *Physical Review B*, vol. 36, 1987.

[119] D. Snoke, N. Sinclair, L. Pfeiffer, K. West, and Z. Vörös, "Dark region of quantum well excitons in stress-induced potentials," in *Lasers and Electro-Optics 2009 and the European Quantum Electronics Conference. CLEO Europe-EQEC 2009. European Conference on*, pp. 1–1, IEEE, 2009.

[120] J. Eisenstein, L. Pfeiffer, and K. West, "Independently contacted two-dimensional electron systems in double quantum wells," *Applied Physics Letters*, vol. 57, no. 22, 1990.

[121] C. Morath, J. Seamons, J. Reno, and M. Lilly, "Layer interdependence of transport in an undoped electron-hole bilayer," *Physical Review B*, vol. 78, no. 11, 2008.

[122] D. Yoshioka and A. Macdonald, "Double quantum well electron-hole systems in strong magnetic fields," *Journal of the Physical Society of Japan*, vol. 59, no. 12, 1990.

[123] I. Spielman, J. Eisenstein, L. Pfeifer, and K. West, "Observation of a linearly dispersing collective mode in a quantum hall ferromagnet," *Physical Review Letters*, vol. 87, no. 3, 2001.

[124] J. Eisenstein and A. Macdonald, "Bose-Einstein condensation of excitons in bilayer electron systems," *Nature*, vol. 432, 2004.

[125] J. Eisenstein, "Exciton condensation in bilayer quantum hall systems," *Annual Review of Condensed Matter Physics*, vol. 5, 2014.

[126] I. Spielman, J. Eisenstein, L. Pfeiffer, and K. West, "Resonantly enhanced tunneling in a double layer quantum hall ferromagnet," *Physical Review Letters*, vol. 84, no. 25, 2000.

[127] M. Kellogg, J. Eisenstein, L. Pfeiffer, and K. West, "Vanishing hall resistance at high magnetic field in a double-layer two-dimensional electron system," *Physical Review Letters*, vol. 93, no. 3, 2004.

[128] E. Tutuc, M. Shayegan, and D. Huse, "Counterflow measurements in strongly correlated GaAs hole bilayers: Evidence for electron-hole pairing," *Physical Review Letters*, vol. 93, no. 3, 2004.

[129] D. Nandi, A. Finck, J. Eisenstein, L. Pfeiffer, and K. West, "Exciton condensation and perfect Coulomb drag," *Nature*, vol. 488, 2012.

[130] C. Morath, J. Seamons, J. Reno, and M. Lilly, "Density imbalance effect on the Coulomb drag upturn in an undoped electron-hole bilayer," *Physical Review B*, vol. 79, no. 4, 2009.

[131] B. Hu, "Prospecting for the superfluid transition in electron-hole coupled quantum wells using Coulomb drag," *Physical Review Letters*, vol. 85, no. 4, 2000.

[132] J. Eisenstein and A. MacDonald, "Bose-Einstein condensation of excitons in bilayer electron systems," *Nature*, vol. 432, 2004.

[133] D. Snoke, "Coherence and optical emission from bilayer exciton condensates," *Advances in Condensed Matter Physics*, vol. 2011, 2010.

[134] A. Baca and C. Ashby, *Fabrication of GaAs Devices*. Institute of Engineering and Technology, 2005.

[135] S. Sze, *Physics of Semiconductor Devices (2nd Ed.)*. John Wiley and Sons, 1981.

[136] A. McLean and R. Williams, "Schottky contacts to cleaved GaAs (110) surfaces. I - eletrical properties and microscopic theories," *Journal of Physics C*, vol. 21, no. 4, 1988.

[137] R. Tung, "Recent advances in Schottky barrier concepts," *Materials Science and Engineering: Reports*, vol. 35, no. 1, 2001.

[138] T. Sebestyen, "Models for ohmic contacts on graded crystalline or amorphous heterojunctions," *Solid-State Electronics*, vol. 25, no. 7, 1982.

[139] A. Lakhani, "The role of compound formation and heteroepitaxy in indium-based ohmic contacts to GaAs," *Journal of Applied Physics*, vol. 56, no. 6, 1984.

[140] R. Cox and H. Strack, "Ohmic contacts for GaAs devices," *Solid-State Electronics*, vol. 10, no. 12, 1967.

[141] J. Shealy and S. Chinn, "Simultaneous diffusion of zinc and indium into GaAs: A new approach for the formation of low resistance ohmic contacts to compound semiconductors," *Applied Physics Letters*, vol. 47, no. 4, 1985.

[142] E. Palik, ed., *Handbook of Optical Constants of Solids*, vol. 1. Academic Press, 1998.

[143] E. Palik, ed., *Handbook of Optical Constants of Solids*, vol. 3. Academic Press, 1998.

[144] R. Balili, *Bose-Einstein Condensation of Microcavity Polaritons*. PhD thesis, University of Pittsburgh, 2009.

[145] W. Petrich, M. Anderson, J. Ensher, and E. Cornell, "Stable, tightly confining magnetic trap for evaporative cooling of neutral atoms," *Physical Review Letters*, vol. 74, no. 17, 1995.

[146] D. Brink and C. Sukumar, "Majorana spin-flip transitions in a magnetic trap," *Physical Review A*, vol. 74, no. 3, 2006.

[147] V. Minogin, J. Richmond, and G. Opat, "Time-orbiting-potential quadrupole magnetic trap for cold atoms," *Physical Review A*, vol. 58, no. 4, 1998.

[148] A. Hammack, N. Gippius, S. Yang, G. Andreev, L. Butov, M. Hanson, and A. Gossard, "Excitons in electrostatic traps," *Journal of Applied Physics*, vol. 99, no. 6, 2006.

[149] Y. Kuznetsova, A. High, and L. Butov, "Control of excitons by laterally modulated electrode density," *Applied Physics Letters*, vol. 97, no. 20, 2010.

[150] A. Ivanov, "Quantum diffusion of dipole-oriented indirect excitons in coupled quantum wells," *Europhysics Letters*, vol. 59, no. 4, 2002.

[151] A. Ivanov, "Thermalization and photoluminescence dynamics of indirect excitons at low bath temperatures," *Journal of Physics: Condensed Matter*, vol. 16, no. 35, 2004.